

**Investigation of Radar Subsurface Sounding through Seasonal Cycles
Collected by Mars Shallow Radar (SHARAD) in the South Polar Area**

Submitted to the Department of Geology
In partial fulfillment of the requirement for the
Degree of Master of Science

Kwan Yee Cheng
B.S., University of Kansas, 2007

Advisory Committee:

Carl Leuschen, Co-Chairman

George Tsoflias, Co-Chairman

J. Douglas Walker

Date of Thesis Defended: _____

[Acceptance Page for Thesis]

**The Thesis Committee for Kwan Yee Cheng certifies that this is the
approved version of the following thesis:**

**Investigation of Radar Subsurface Sounding through Seasonal Cycles
Collected by Mars Shallow Radar (SHARAD) in the South Polar Area**

Advisory Committee:

Carl Leuschen, Co-Chairman

George Tsoflias, Co-Chairman

J. Douglas Walker

Date Approved: _____

Abstract

Using an orbital-based ground-penetrating radar – SHARAD proves to be an effective method for imaging the Martian surface and subsurface layering at the south polar layered deposit. This investigation focuses on examining whether seasonal variation of CO₂ thickness on the surface caused by accumulation during winter and sublimation during summer could be observed for the first time by analyzing SHARAD data. Travel time and amplitude analysis between the Martian surface reflection and a reference reflection in the subsurface were conducted on multiple orbital tracks corresponding to varying seasons. Results from the travel time analysis along all four cross-lines show that the average change in CO₂ frost thickness ranged from 6.80 m to 9.58 m assuming a medium dielectric constant between 2.12 and 2.77. The CO₂ thickness reaches its maximum during winter and minimum during summer likely because of the CO₂ frost accumulation and retreat, respectively. This observation agrees with other studies. However, the magnitude of change in CO₂ thickness estimated in this study is greater than values reported previously. This difference is attributed to the different locations of the Martian polar region examined in the various studies. Amplitude analysis does not show any relationship to seasonal variations on the Martian surface.

Dedication

I would like to dedicate my work on this project to my family and friends and to thank them for their supports. I would like first to give thank to God for His guidance throughout all these years studying aboard at KU. His strength, wisdoms, and grace given to me cannot be measured. I would like to thank all of my friends at KU for their wonderful times together, especially A.J. Herrs, Ben Rickard, Mike Christie, Alicia Rosales, Dave Riese and many more. Thank you for bringing me such unforgettable times together, including drinking, camping, going on fieldtrips, and more importantly, sharing the interest in geology and geophysics. I would like to thank Thao Linh, my significant other, for your care, patient, and prayers. You always bring me positive energy and remind me to be a more confident, unselfish and considerate person. Finally, I would like to thank my family. I especially thank my parents for their financial support, unconditional love and valuable teachings that I will never forget. You taught me to work hard and be a responsible person for whatever I do. I also thank my sisters, Lai On, Lai Yee, and Lai Wah, for their financial supports, time, and being my role models in life. Without every one of you, I would not have finished my undergraduate degree and completed this study. Thank you for being there for me and I love you all.

Acknowledgements

I would like to first thank my graduate advisors, George Tsoflias and Carl Leuschen, for their direct guidance and insights on this study. I would like to thank George Tsoflias, who was also my undergraduate advisor, for his guidance and opportunity to work with him throughout all these years. Thank you for leading me into this fascinating geophysics field and providing an excellent environment to learn about it. I would like to thank Carl Leuschen for his financial support for the past three years and sharing his valuable experience on radar subsurface imaging on Mars. I also would like to thank Doug Walker for being on my committee and sharing his insights. I would like to thank the whole SHARAD team for providing the processed data, maintaining the instrument, and also organizing the data. For all the technical discussions on radar hardware and theory, programming in MATLAB, and loading data into Kingdom Suite, I would like to thank Anthony Hoch, Ross Black, and Chris Gifford for sharing their time, experience, and assistance. I would like to thank Blair Benson, Amanda Falk, Brian Miller, Dave Riese, Alicia Rosales, and Richard Styron for reviewing my drafts and giving me suggestions. Finally, I would like to thank NASA for funding this work and having made this investigation possible.

Table of Contents

Abstract.....	iii
Dedication	iv
Acknowledgements	v
Table of Contents	vi
List of Figures.....	viii
List of Tables	xi
Chapter 1: Introduction	1
1.1 Introduction to ground-penetrating radar for Mars exploration	1
1.2 Martian subsurface sounding instrumentation	3
1.3 Presence of water ice layer at the south pole of Mars	12
1.4 Presence of CO ₂ frost layer on the surface at the south pole of Mars....	19
1.5 Research objectives	23
Chapter 2: Field Site Selection, Data Acquisition and Processing	25
2.1 Field site selection and data acquisition.....	25
2.2 SHARAD data processing.....	31
2.3 Data editing	37

Chapter 3: Data Analysis and Interpretation	40
3.1 Horizon identification and picking.....	40
3.2 Track alignment.....	47
3.3 Data management.....	50
3.4 Travel time analysis	52
3.5 Amplitude analysis.....	63
Chapter 4: Results and Discussion	66
4.1 Travel time analysis	66
4.2 Amplitude analysis.....	84
Chapter 5: Conclusions and Recommendations	87
References.....	90
Appendices.....	96
Appendix A: List of datasets selected.....	97
Appendix B: Data loading and editing scripts in IDL	98
Appendix C: Loading and writing data to SEG-Y in MATLAB.....	101
Appendix D: Loading data into Kingdom Suite	103
Appendix E: Twelve selected orbital tracks.....	111
Appendix F: Matlab scripts for data analysis.....	118

List of Figures

Figure 1.1	SHARAD on Mars Reconnaissance Orbiter	8
Figure 1.2	Imaging capability between MARSIS and SHARAD	10
Figure 1.3	Cross-section collected by SHARAD in the NPLD	11
Figure 1.4	Amount of thermal neutrons captured by γ spectrometer	16
Figure 1.5	Normalized flux of hydrogen gamma rays at different latitude ...	16
Figure 1.6	Simultaneous THEMIS infrared (IR) data	17
Figure 1.7	Images of adsorption features of CO ₂ and H ₂ O ice at the SPLD .	18
Figure 1.8	Elevation changes versus time collected by MOLA	22
Figure 2.1	Study area for the investigation at the south PLD on Mars	29
Figure 2.2	An example of a radar cross-section (track #5570)	30
Figure 2.3	MRO/SHARAD orientations in space	35
Figure 3.1	Twelve selected orbital tracks on the base map	44
Figure 3.2	Surface and subsurface horizon picks on orbital track 8787	45
Figure 3.3	Surface and subsurface horizon picks on orbital track 11920	46
Figure 3.4	Misalignment of surface horizons on cross-line 11920	48
Figure 3.5	Misalignment of surface horizons on in-line 8787	49

Figure 3.6	Closest traces between a cross-line and an in-line	57
Figure 3.7	Surface and subsurface horizons before alignment	59
Figure 3.8	Surface and subsurface horizons after alignment	59
Figure 3.9	Δ surface elevation in time vs. Ls (Cross-line 11920)	60
Figure 3.10	Solar longitude (Ls)	61
Figure 3.11	Δ surface elevation in meters vs. Ls (Cross-line 11920)	62
Figure 3.12	Amplitude ratio vs. Ls (Cross-line 5789)	65
Figure 4.1	Δ travel time at each intersection vs. Ls (Cross-line 4444)	73
Figure 4.2	Δ travel time at each intersection vs. Ls (Cross-line 5723)	73
Figure 4.3	Δ travel time at each intersection vs. Ls (Cross-line 5789)	74
Figure 4.4	Δ travel time at each intersection vs. Ls (Cross-line 11920)	74
Figure 4.5	Thickness at each intersection vs. Ls (Cross-line 4444)	75
Figure 4.6	Thickness at each intersection vs. Ls (Cross-line 5723)	75
Figure 4.7	Thickness at each intersection vs. Ls (Cross-line 5789)	76
Figure 4.8	Thickness at each intersection vs. Ls (Cross-line 11920)	76
Figure 4.9	One-way travel time and thickness along cross-line 4444	77
Figure 4.10	One-way travel time and thickness along cross-line 5723	77
Figure 4.11	One-way travel time and thickness along cross-line 5789	78
Figure 4.12	One-way travel time and thickness along cross-line 11920	78

Figure 4.13	Radar wave propagation velocity vs. different ϵ_r	79
Figure 4.14	Thickness vs. dielectric constant along cross-line 4444	80
Figure 4.15	Thickness vs. dielectric constant along cross-line 5723.....	80
Figure 4.16	Thickness vs. dielectric constant along cross-line 5789.....	81
Figure 4.17	Thickness vs. dielectric constant along cross-line 11920	81
Figure 4.18	Difference in amplitude ratio vs. Ls (Cross-line 4444)	85
Figure 4.19	Difference in amplitude ratio vs. Ls (Cross-line 5723)	85
Figure 4.20	Difference in amplitude ratio vs. Ls (Cross-line 5789)	86
Figure 4.21	Difference in amplitude ratio vs. Ls (Cross-line 11920)	86

List of Tables

Table 1.1	History of successful Mars exploration missions	7
Table 1.2	SHARAD and MARSIS instrument parameters	9
Table 3.1	Data types stored for each orbital track in MATLAB	51
Table 3.2	Data types stored for each intersection in MATLAB	58
Table 4.1	Thicknesses with $\epsilon_r = 2.12$ and 2.77 (4444)	82
Table 4.2	Thicknesses with $\epsilon_r = 2.12$ and 2.77 (5723)	82
Table 4.3	Thicknesses with $\epsilon_r = 2.12$ and 2.77 (5789)	82
Table 4.4	Thicknesses with $\epsilon_r = 2.12$ and 2.77 (11920)	83
Table 4.5	Average thicknesses with $\epsilon_r = 2.12$ and 2.77	83

Chapter 1: Introduction

1.1 Introduction to ground-penetrating radar for Mars exploration

Ground-penetrating radar (GPR) or Radar subsurface sounding has been successfully applied to many different geological investigations on Earth. This includes imaging sedimentary structures and faults (Christie et al., 2009), detecting fractures (Tsoflias et al., 2004), and quantifying thickness of the Greenland ice sheets (Gogineni et al., 2001). Different types of radar instruments, such as airborne, borehole, surface, and orbital based systems, have been developed to meet the needs of the radar remote sensing investigations. These advancements in radar subsurface sounding technology over the past few decades have made exploration of other planets' subsurface, such as Mars, possible. One of the most important goals of using GPR on Mars is to determine if water exists beneath the surface. Orbital-based GPR instruments have been deployed to try to answer this question (Nunes et al., 2006; Picardi et al., 2005; Seu et al., 2007b).

Rover-based GPR is still under development for high resolution near-surface imaging on the Martian surface (Grant et al., 2003); however, orbital subsurface sounding radars have been deployed successfully and been operational since their deployment, providing the first glimpse of the Martian subsurface. The

Mars Advanced Radar for Subsurface and Ionosphere Sounder (MARSIS) onboard the Mars Express (MEX) satellite was the first orbital subsurface sounding radar deployed by the European Space Agency (ESA) on June 2, 2003 for the purpose of searching for water in the Martian subsurface (Farrell et al., 2008). The second orbital subsurface imaging instrument was the Shallow (Subsurface) Radar (SHARAD) onboard the Mars Reconnaissance Orbiter (MRO), which was launched by the National Aeronautics and Space Administration (NASA) on August 12, 2005. SHARAD is the first Italian facility instrument aboard a completely American mission (Seu et al., 2007b; Zurek et al., 2007). Details of these two instruments' mission objectives, specifications, and differences are discussed in Chapter 1.2.

The main objective of this thesis is to investigate if SHARAD data can be used to evaluate seasonal variations in the CO₂ thickness on the Martian south polar ice cap. This thesis consists of 5 chapters. Chapter 1 discusses the hypothesis and approach of this work, as well as the basic background of GPR for Martian subsurface exploration, the instruments' specifications and comparisons, a brief hydrological history of the Martian south polar ice cap, and a discussion of previous work on the existence of water ice and CO₂ frost. Chapter 2 discusses the location of interest, data acquisition, and processing. Chapter 3 discusses the data analysis and interpretation. Chapter 4 presents results and discussion from interpretation in the third chapter. Chapter 5 draws conclusions from the findings

of this work, their implications to radar subsurface sounding on Mars using SHARAD, and future work recommendations.

1.2 Martian subsurface sounding instrumentation

Multiple missions have been launched by NASA to explore Mars since the 1960s. The first successful mission was Mariner 4, launched in 1964, which flew by Mars and returned 21 images to Earth. With the success of the Mariner and Viking missions in the 1960s and 1970s, more probes were sent to Mars for further studies, including both exploration rovers Spirit and Opportunity, which have been exploring the surface of Mars since 2003, and Mars Phoenix Lander in 2007. NASA's Mars Science Laboratory rover, Curiosity, is expected to launch in 2011. A list of successful missions is shown in Table 1.1.

The MEX satellite was launched by the European Space Agency (ESA) in 2003. Onboard MEX was the first radar subsurface sounder called MARSIS. MARSIS is a synthetic-aperture radar (SAR). Detailed SAR theory will be discussed in Chapter 2.2. MARSIS can operate at 4 different frequency bands centered at 1.8, 3.0, 4.0, and 5.0 MHz each with 1 MHz bandwidth in a 40-m-monopole antenna configuration. A synthetic aperture algorithm is used to achieve finer along-track image resolution and higher signal-to-noise (SNR) with

limited power supply and antenna length. MARSIS has a cross-track resolution of 10–30 km and an along-track resolution of 5 km after Doppler focusing. The vertical resolution in free space is approximately 150 m and processing is required onboard MEX to reduce the data volume (Farrell et al., 2008; Safaeinili et al., 2003).

On August 12, 2005, SHARAD was launched onboard MRO by NASA. SHARAD was the second radar subsurface sounder sent to Mars (Figure 1.1). SHARAD was provided by the Italian Space Agency as a facility instrument on MRO to compliment MARSIS. MRO entered Mars' orbit successfully on March 10, 2006 and completed aero-braking into a circular orbit with a low altitude of 250–320 km above the Martian surface (Seu et al., 2007b; Zurek et al., 2007). SHARAD complements MARSIS with a finer spatial and vertical resolution. SHARAD is also a SAR operating at a single 20 MHz center frequency band with 10 MHz bandwidth in a 10-meter-dipole antenna configuration. This altitude and frequency range provides both along-track and cross-track resolution of 3–6 km, which represent the first and the second Fresnel zones. The along-track resolution can be increased with synthetic-aperture focusing (Doppler focusing) to 0.3–1 km. The maximum vertical resolution in free-space is 15 m and 8.4 m in water ice assuming real relative permittivity of 3.15. Surface penetration depth is approximately 0.5–1 km (Putzig et al., 2009).

SHARAD has been designed for higher resolution imaging than MARSIS; however, SHARAD does not penetrate as deep. SHARAD's signal (Figure 1.2) was rarely able to detect a basal reflection between bedrock and the south polar ice cap. Table 1.2 shows a comparison of the two radar systems (Seu et al., 2007b). MARSIS was able to detect the basal reflector at a depth of 3.7 km beneath the surface with lower frequency bands from 1.3 to 5.5 MHz as shown in Figure 1.2. SHARAD's primary objective is mapping dielectric interfaces of Polar Layered Deposits (PLD) at the north and south poles, searching for water, and detecting internal layers in sedimentary series up to a few hundred meters in depth (Plaut et al., 2007; Seu et al., 2007b). MARSIS's objective is to image to greater depth. With both subsurface imaging radars working alongside each other, a large amount of data and more complete coverage of the surface and subsurface can be obtained for analysis to understanding better the Martian subsurface.

SHARAD's ability to detect layering in the shallow subsurface has been tested through modeling. Calculation of the relative radar reflection strength from layer interfaces indicates that dielectric properties of silicate inclusions in ice significantly affect the depth of SHARAD signal's penetration. Signals can reach at least 250 m deep in highly conductive altered basaltic dust in ice-rich areas, and up to 2 km in ice-rich areas with widespread weakly conductive silicate inclusions. Vertical resolution in the models can reach approximately 20 m under ideal conditions for stratigraphic mapping in the PLD (Nunes et al., 2006).

SHARAD has recently returned promising data from the North PLD. Dust trapped in between finely layered water ice has been revealed in the North PLD region (Figure 1.3) (Putzig et al., 2009). Radar subsurface imaging results are generally displayed in cross-section view. The horizontal axis of the cross-section represents the cross-section position on the surface. The vertical axis represents amplitude information at each two-way signal travel time or depth, if time-depth conversion has been performed (Figure 1.3). There are sequences of subsurface reflections in the North PLD area on Mars (Figure 1.3). Package G, which is the first sequence below the surface, returns the strongest signal and the signal strength progressively decreases as the arrival time increases. This decreasing trend in amplitude does not indicate that the layers are thicker or the dielectric contrast is decreased. This phenomenon occurs because of the attenuation of higher frequency radar signal and loss due to reflections as it travels through the subsurface (Putzig et al., 2009). Dielectric constants of 1 for the Martian atmosphere and 3.15 for the subsurface were used to calculate SHARAD's radar wave velocity for the time to depth conversion for the middle panel in Figure 1.3. The bottom panel in Figure 1.3 is the Mars Orbital Laser Altimeter (MOLA) topographic profile for the radar cross-section location (Putzig et al., 2009). These data show that SHARAD is able to provide meaningful subsurface information of the PLDs as expected from careful radar system designs for subsurface imaging of geologic structures and materials.

Launch Date	Name	Results
1964	Mariner 4	Returned 21 images
1969	Mariner 6	Returned 75 images
1969	Mariner 7	Returned 126 images
1971	Mariner 9	Returned 7,329 images
1975	Viking 1 (Orbiter/Lander)	Located landing site for Lander and first successful landing on Mars
1975	Viking 2 (Orbiter/Lander)	Returned 16,000 images and extensive atmospheric data and soil experiments
1996	Mars Global Surveyor	More images than all previous Mars missions
1996	Mars Pathfinder	Technology experiment lasting 5 times longer than the expected length of mission
2001	Mars Odyssey	High resolution images of Mars
2003	Mars Express Orbiter/ Beagle 2 Lander	Orbiter imaging Mars in detail and Lander lost on arrival
2003	Mars Exploration Rover – Spirit	15 times longer than the expected length of mission and still operating
2003	Mars Exploration Rover – Opportunity	15 times longer than the expected length of mission and still operating
2005	Mars Reconnaissance Orbiter	Returned more than 26 terabits of data (more than all other Mars missions combined)
2007	Phoenix Mars Lander	Returned more than 25 gigabits of data

Table 1.1 History of successful Mars exploration missions by NASA and ESA (National Aeronautics and Space Administration).

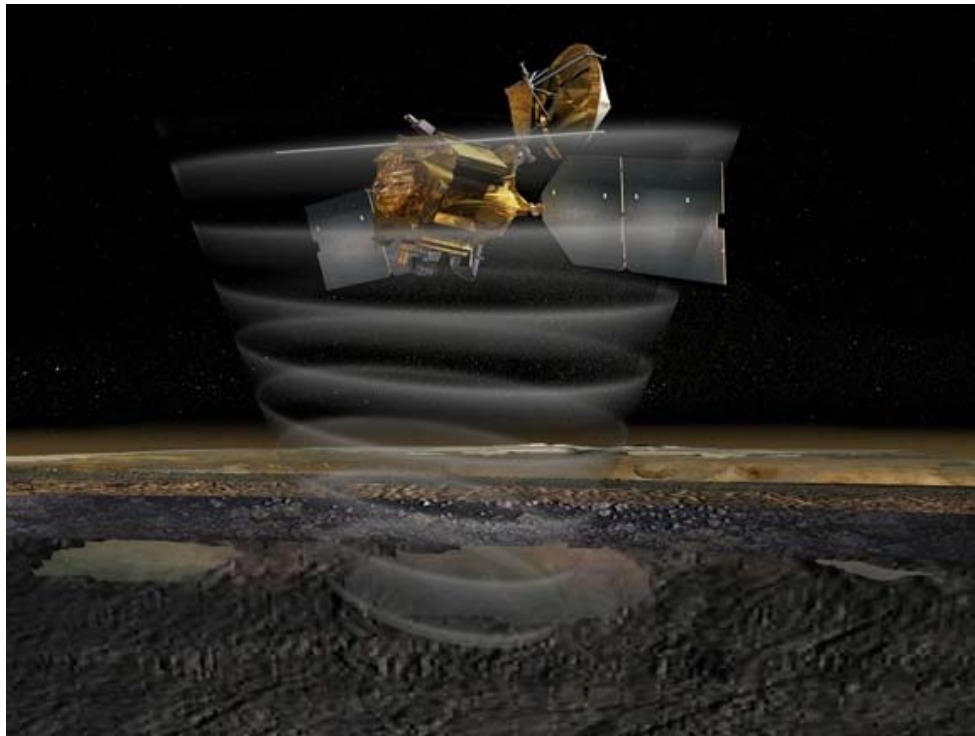


Figure 1.1 The long pole on MRO is Shallow Radar's (SHARAD) dipole antenna transmitting and receiving signals to and from the subsurface (National Aeronautics and Space Administration et al., 2005).

	SHARAD	MARSIS
Frequency Band	15 — 25 MHz	1.3 — 2.3, 2.5 — 3.5, 3.5 — 4.5, 4.5 — 5.5 MHz
Vertical Resolution, theoretical, Reciprocal Bandwidth, $\epsilon_r = 4$	7.5 m	75 m
Transmitter Power	10 W	10 W
Pulse Length	85 μ s	250 or 30 μ s
PRF	700 or 350 Hz	127 Hz
Antenna Configuration	10 m tip-to-tip dipole	40 m tip-to-tip monopole
Postprocessor SNR (Worst to Best)	50 — 58 ^a dB	30 — 50 ^b dB
Horizontal Resolution (Along Track X Cross Track)	0.3 — 1 km by 3 — 6 km	5 — 10 km by 10 — 30 km

(a) Estimate (b) Actual

Table 1.2 SHARAD and MARSIS instrumentation parameters (Seu et al., 2007b)

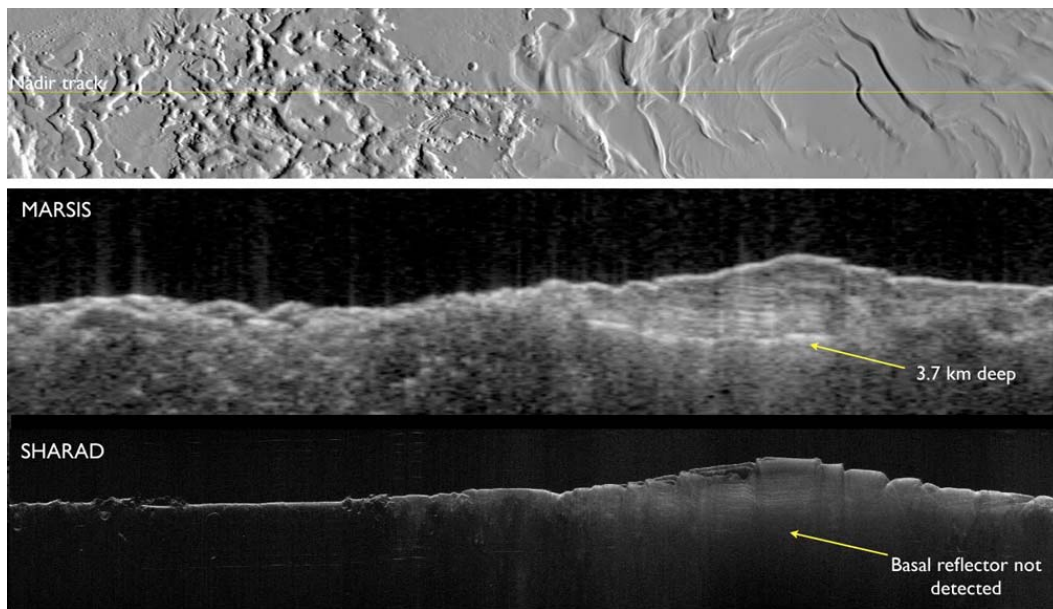


Figure 1.2 A comparison of two radar subsurface sounders - MARSIS and SHARAD tracks over the South PLD on Mars. MARSIS was designed to penetrate deeper than SHARAD, detecting the basal reflector at a depth of 3.7 km below the surface. The top panel is the MOLA data where both cross-sections are located on the surface (National Aeronautics and Space Administration et al., 2008).

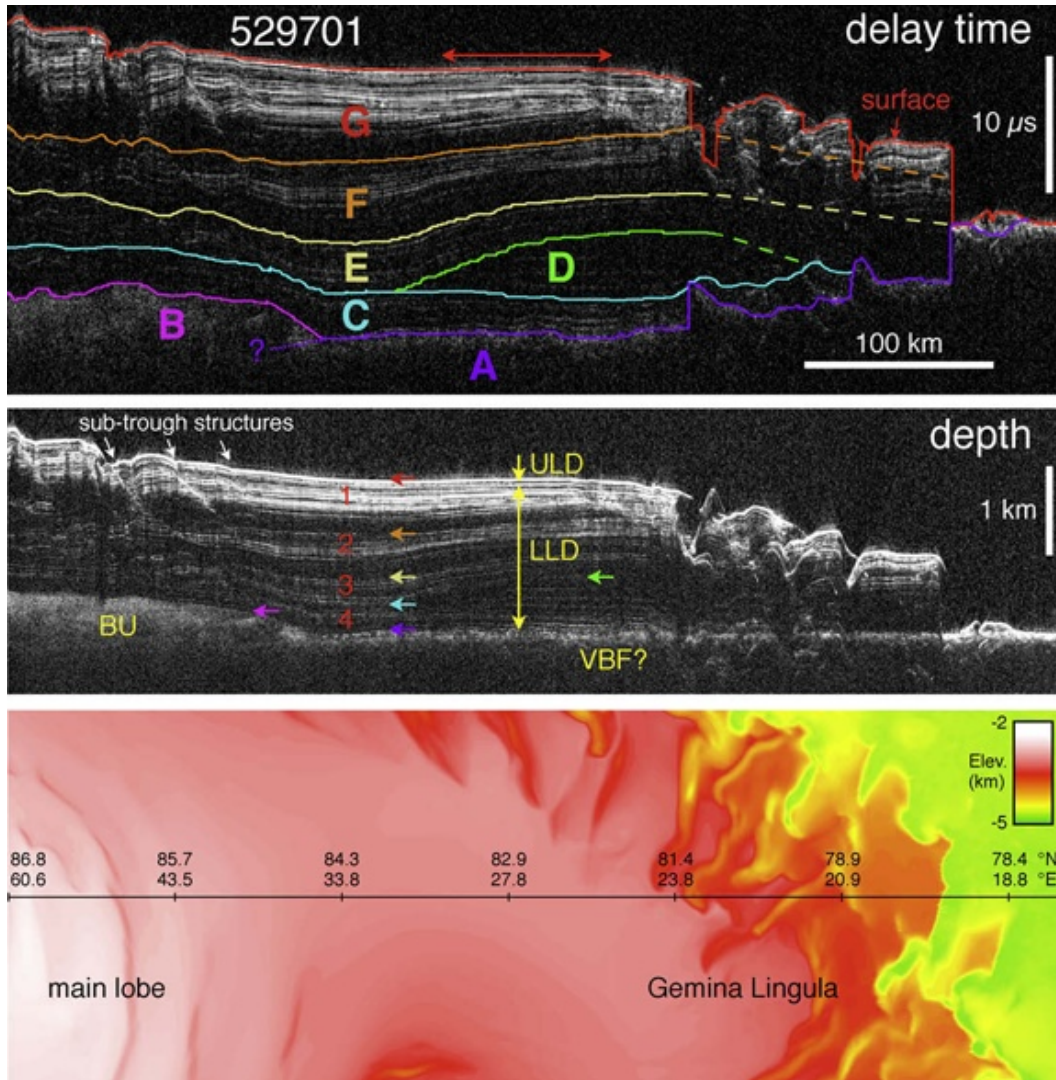


Figure 1.3 Data collected by SHARAD from the North PLD. The top panel is the radar cross-section in the time domain. Layers can be delineated into different packages (A, B, C, D, E, F, and G). The middle panel is the same data set but in the depth domain. The yellow arrows and labels approximately correspond to the interpretation made by Tanaka et al. (2005) (VBF: Vastitas Borealis Formation; BU: basal unit; LLD: lower layered deposits; ULD: upper layered deposits). The numbers in red correspond to interpretation made by Phillips et al. (2008) as packages. The bottom panel is the MOLA profile that shows the location of this radar cross-section (black line) (Putzig et al., 2009).

1.3 Presence of water ice layer at the south pole of Mars

Searching for water on Mars has always been the center of investigations for Mars exploration. The existence of water may be a critical factor necessary for past life; hence, understanding the geological and hydrological processes on the planet is important. Many studies have been done to understand the south polar region in particular (Bibring et al., 2004; Boynton et al., 2002; Kelly et al., 2006; Nye et al., 2000; Titus et al., 2003). The findings from these studies suggest that the south polar ice cap consists of an upper layer of CO₂ frost and a lower layer of water ice, containing some unknown amount of iron rich dust (Pettinelli et al., 2005). A study using the gamma-ray spectrometer onboard Mars Odyssey has shown significant amounts of hydrogen over the south polar region during the southern summer (Boynton et al., 2002). A large amount of hydrogen suggests the presence of water ice. The gamma-ray spectra (Figure 1.4) show the amount of thermal neutrons captured from hydrogen at three different regions on Mars. It is evident that the south polar ice cap has an abundance of hydrogen during the southern summer when the water ice is exposed on the surface. On the other hand, the north polar ice cap lacks strong evidence of hydrogen because a thick layer of CO₂ frost accumulation on top of the water ice cap during the northern winter blocks gamma-rays. The spectra from the north polar ice cap, therefore, are used as a background to correct the spectra for the other two regions (Boynton et al., 2002). The normalized flux of hydrogen gamma rays (Figure 1.5) shows the same

result; this flux reaches its maximum near latitude -90° (the south polar ice cap) during southern summer and decreases as latitude increases. Epithermal neutron flux also decreases, which is another independent indication of increasing hydrogen content. The hydrogen gamma-ray flux begins to climb toward the North Pole and then decreases again around latitude 60° (in the northern hemisphere) as the north polar ice cap is covered by a thick layer of CO_2 frost during the northern winter season. Only a small amount of hydrogen is at the edge of and in the mix of the CO_2 frost. This study suggests the presence of saturated water ice present in the near surface up to 1 m deep, which gamma and neutron methods can detect (Boynton et al., 2002).

A study by Titus et al. (2003) indicates that surface water ice exists underneath the CO_2 frost in the south polar ice cap, which was once thought to consist only of CO_2 frost. Thermal measurements from the Viking's missions were not able to provide a positive result of water ice detection a few centimeters below the surface. The newer and more sophisticated Thermal Emission Imaging System (THEMIS) onboard Mars Odyssey reveals that water ice is exposed when the CO_2 frost retreats to its annual minimum during late summer in the southern hemisphere and extends over a large area beneath the CO_2 frost (Titus et al., 2003). Figure 1.6 shows thermal observations near 85.5° S and 10° E on $L_s = 334^\circ$ (late southern summer). This false-color image shows that the water ice (Unit I) is exposed and extends toward the lower latitude area. Unit S, which is

further away from the south polar ice cap, has a higher temperature, representing the Martian soil surface. The CO₂ frost retreats back to the higher latitude during late southern summer season. Unit C, which shows lower temperatures than water ice and the Martian soil, is the perennial CO₂ frost on top of the water ice.

Similar conclusions were made from data collected by the Observatoire pour la Minéralogie, l'Eau, les Glaces et l'Activité (OMEGA) instrument. OMEGA is one of the seven instruments onboard the Mars Express. It is a spectrometer analyzing reflected sun light and thermal emission from the Martian surface between the visible and near-infrared spectrums (0.35 – 5.2 μm). Different materials, such as water ice and CO₂ frost, can be delineated because each material absorbs certain wavelengths in the spectrum. It can also determine the concentration of each material on the surface by measuring the intensity of electromagnetic radiation each material absorbs (Bibring et al., 2004). Figure 1.7 illustrates adsorption features of CO₂ and water ice, showing that the area of water ice is larger than that of CO₂. Water ice coverage extends further out than the CO₂ frost when the CO₂ frost sublimates into the atmosphere during the southern summer. This exposes the water ice layer beneath the CO₂ frost. This study also finds that water ice is trapped when the CO₂ frost is stable on the surface. OMEGA data suggest that water ice is left behind with dust when CO₂ frost sublimates away. Also, the CO₂ frost might be rather thin, on the order of several

meters suggested by lack of dramatic changes in topography in MOLA topographic profiles at the boundary between the CO₂ cap and water ice.

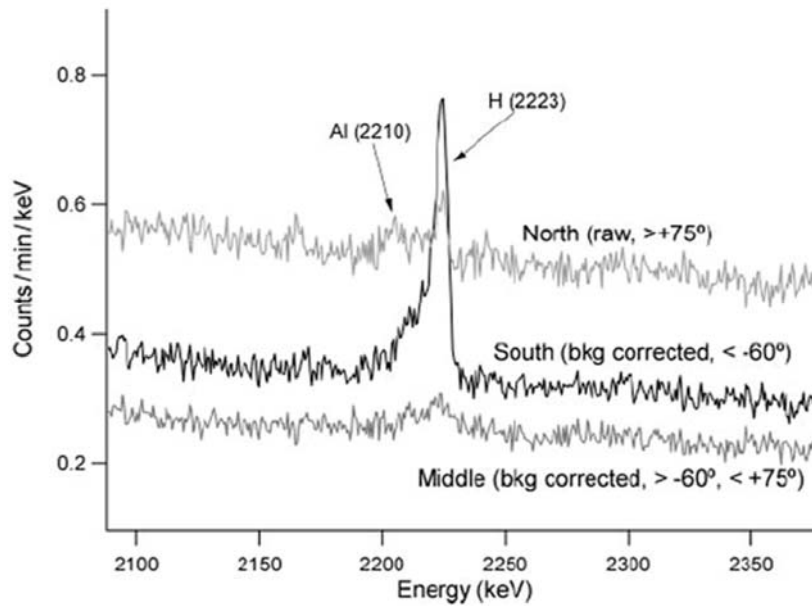


Figure 1.4 Amount of thermal neutrons captured from hydrogen (H) during the southern summer season at the north pole, the south pole, and middle to low latitude area (Al: aluminum) (Boynton et al., 2002).

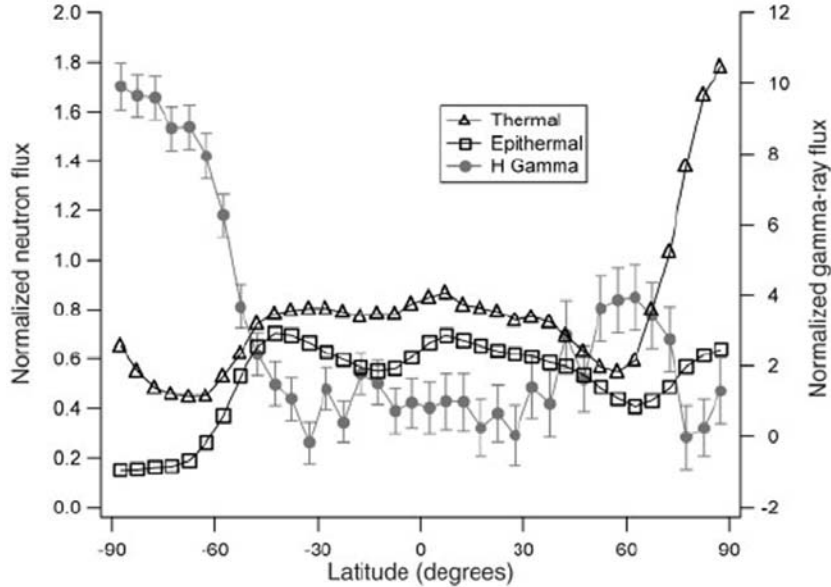


Figure 1.5 Normalized flux of hydrogen gamma rays collected during the southern summer season. The epithermal neutron flux, which shows the opposite trend, independently indicates the increasing hydrogen content (Boynton et al., 2002).

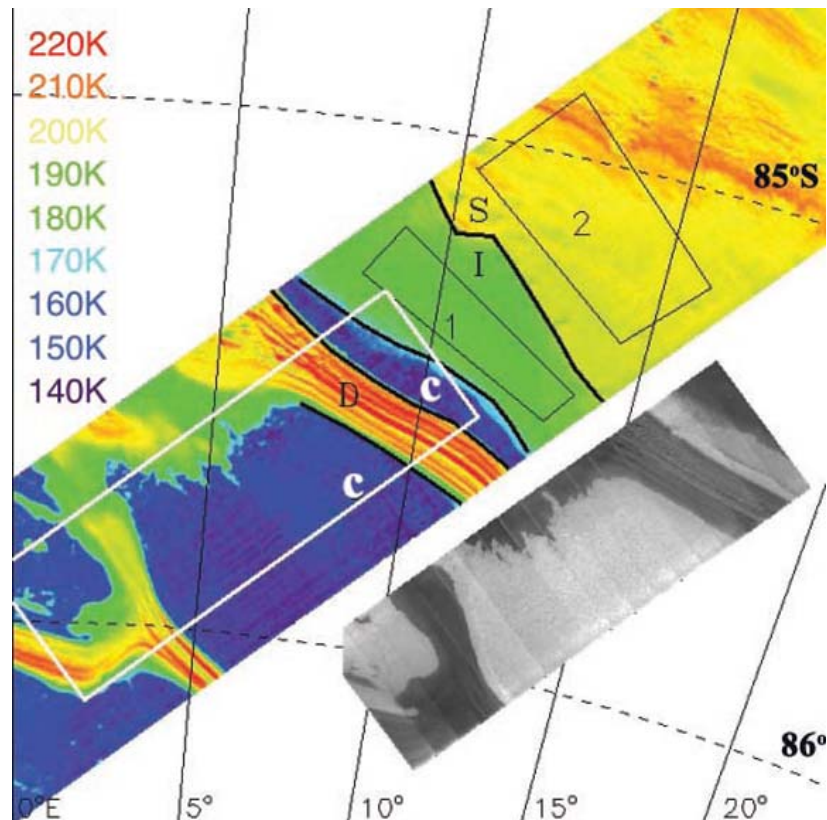


Figure 1.6 The false-color image is the simultaneous THEMIS infrared (IR) data collected at $L_s = 334^\circ$ (late southern summer). The colors in this image represent different thermal units. Unit I, which has an intermediate temperature, is water ice. Unit C is solid CO₂ on the surface (lowest temperature). Unit S represents soil on the surface (warmer temperature) (Titus et al., 2003).

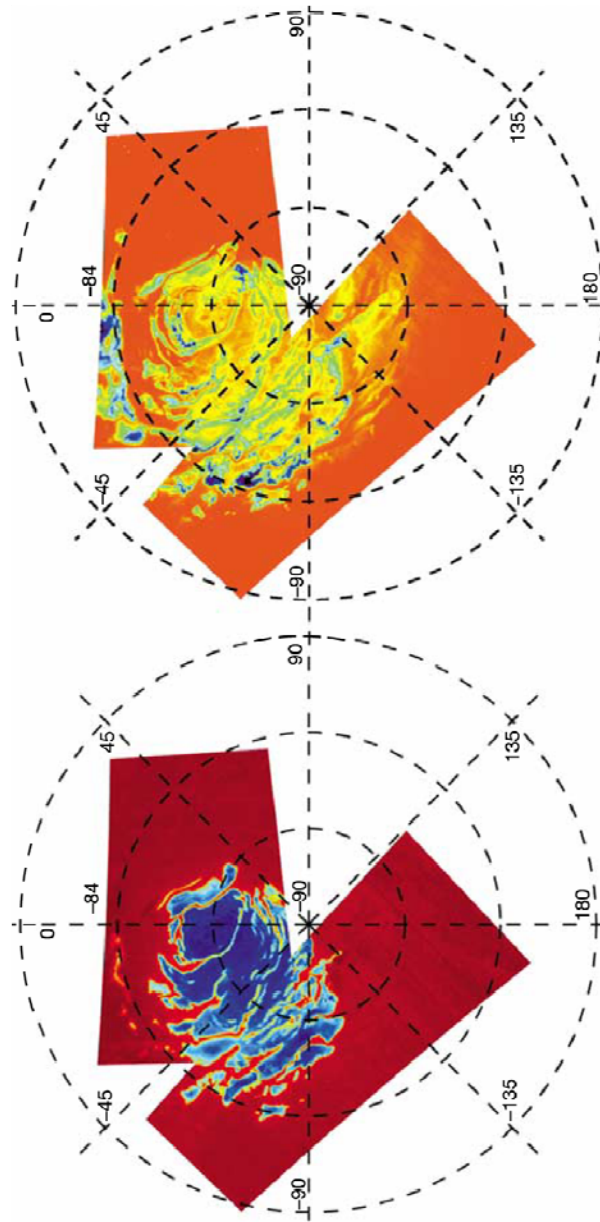


Figure 1.7 Images of adsorption features of CO₂ frost and water ice over the south polar area. The bottom image shows the coverage of the CO₂ frost, scaled from blue (presence of CO₂ frost) to red (CO₂ frost free). The top image shows the coverage of the water ice, scaled from blue (presence of water ice) to orange (water ice free). These images show that water ice extends further than the CO₂ frost (Bibring et al., 2004).

1.4 Presence of CO₂ frost layer on the surface at the south pole of Mars

The presence of a layer of CO₂ frost at the south polar ice cap of Mars has been suggested in an earlier study by Kieffer (1979) based on measurements from the Viking Infrared Thermal Mapper (IRTM). Temperature readings over the south pole were less than 10 K above the CO₂ sublimation point while the north pole was more than 50 K above the CO₂ sublimation point. At the south pole, the CO₂ frost does not sublimate completely during the year. This study also suggests that water ice is trapped both within and beneath the CO₂ frost (Kieffer, 1979). Investigations mentioned in the previous section agree that water ice exists underneath the CO₂ frost and is exposed during the southern summer season when the CO₂ frost retreats to its minimum higher latitude and elevation (Bibring et al., 2004; Boynton et al., 2002; Titus et al., 2003). Studies by Aharonson et al. (2004), Kelly et al. (2006), Smith et al. (2001), and Tokar et al. (2003) using different instruments have since been done to further investigate the dynamic behaviors of the CO₂ frost on the surface.

These studies have shown that CO₂ frost on the surface at both poles varies with time (Feldman et al., 2003; Kelly et al., 2006). However, the dynamic behavior of the CO₂ frost at each pole is different. CO₂ begins to condense during autumn at high latitude when the amount of sunlight decreases. A layer of CO₂ frost is formed first at high latitude and extends toward the equator as winter

arrives. The thickness of CO₂ frost at both poles is greatest during mid and late winter. During early spring when both poles start receiving more sunlight, the temperature is higher than the CO₂ condensation point and the frost sublimates back into the atmosphere. The CO₂ frost is then limited to areas higher in latitude and elevation. The CO₂ frost at the north polar ice cap sublimates completely because the elevation is 6 km lower than at the south polar ice cap. The temperature during summer reaches far above the CO₂ condensation point, which leads to the exposure of the residual water ice cap underneath. Conversely, the thin layer of CO₂ frost at the south polar ice cap remains in its solid form during summer as a result of higher elevation and lower atmospheric pressure (Smith et al., 2001). Also, the thin layer of the CO₂ frost remains on the surface because the summer is shorter in the southern hemisphere. Mars is running in an elliptical orbit and the Sun is not positioned at the center of the orbit, which result a shorter summer and a longer winter in the southern hemisphere than the northern hemisphere. Measurements from the MOLA onboard MGS also indicate the same CO₂ exchange phenomena from recording the seasonal change in surface elevation at both poles. Figure 1.8 shows the elevation changes for more than a full Martian year at the north polar, north mid-latitude, south polar, and south mid-latitude regions. A full Martian year is divided into 360 solar longitudes (L_s). The observation starts during northern summer and southern winter ($L_s = 90$). At the northern hemisphere (Figure 1.8A and 1.8B), elevation does not vary

considerably during the summer. After the autumnal equinox at the northern hemisphere ($L_s = 180^\circ$), CO₂ frost starts accumulating as the amount of sunlight decreases. The CO₂ frost reaches its maximum thickness during late winter ($L_s = 345^\circ$) and the ice surface elevation change is 1.5 ± 0.25 m. The change in elevation generally decreases toward the equator. The elevation change also decreases as the temperature rises and CO₂ sublimate back into the atmosphere during northern summer. Observation in the southern hemisphere starts during winter and the change in elevation behaves similar to that shown for the northern hemisphere winter (Figure 1.5C and 1.5D). The maximum change in elevation is 0.9 ± 0.3 m at $L_s = 155^\circ$ (Smith et al., 2001).

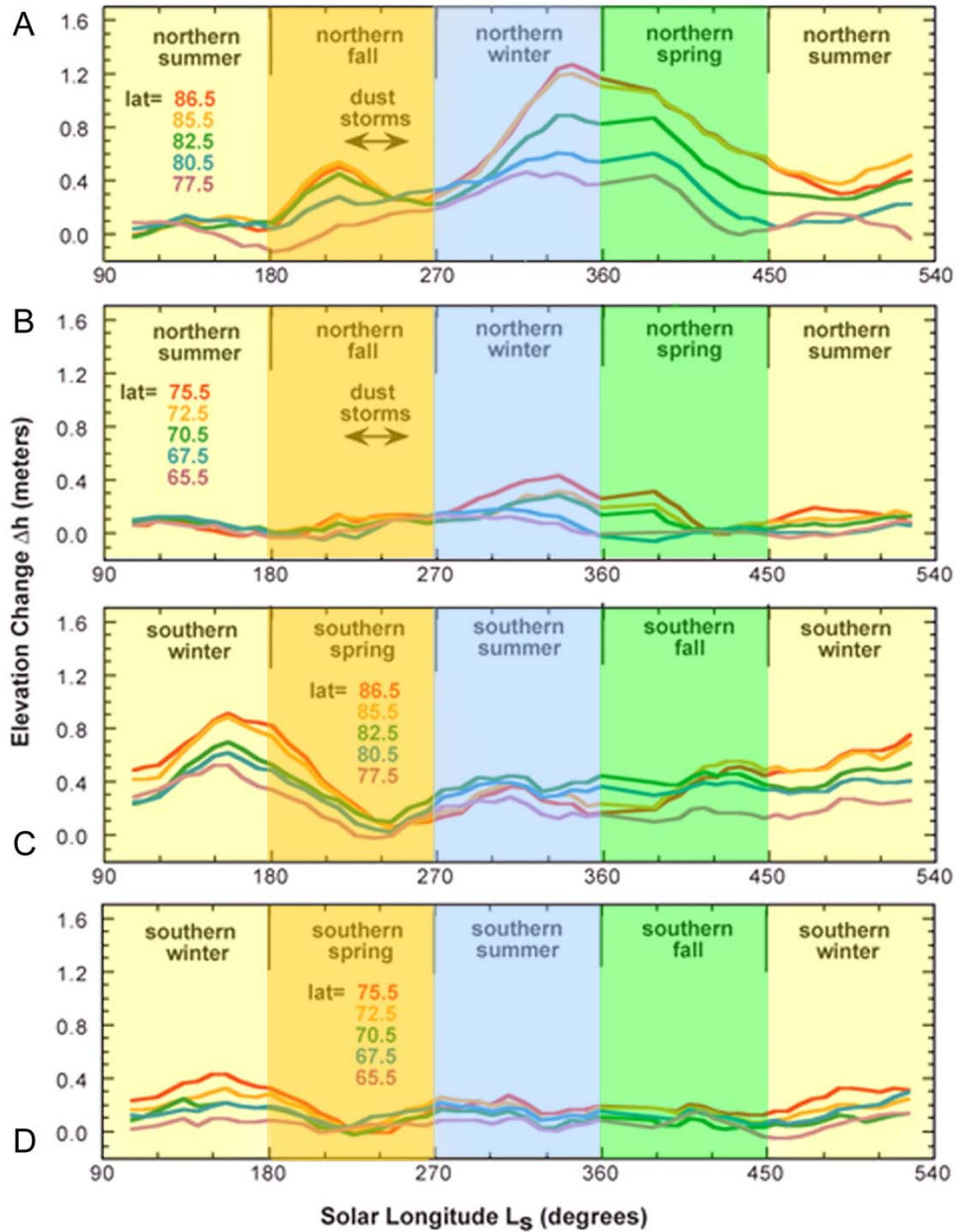


Figure 1.8 Elevation changes (Δh) versus time (Solar longitude L_s) collected by the MGS mapping mission for 1.25 Martian seasons at the (A) north polar, (B) north mid-latitude, (C) south polar, and (D) south mid-latitude regions. Elevation at latitude 60°N is a reference for calculating elevation changes in the northern hemisphere and 60°S for the southern hemisphere because elevations stay very constant over the course of different seasons (Smith et al., 2001).

1.5 Research objectives

Historically, studies have been performed on CO₂ frost behavior in the north and south polar regions. For example, the study by Nunes and Phillips (2006) stated that SHARAD can be used to monitor advances and retreats of the polar deposits. Seu et al. (2007a) explained that unlike the CO₂ frost in the north polar region, which disappears completely during summer in response to solar radiation, the south polar region retains a thin layer of solid CO₂ frost mixed with dust and water ice. Kelly et al. (2006) observed that the CO₂ frost becomes thicker during winter from condensation and precipitation, and thinner from sublimation during summer. Studies by Bibring et al. (2004) and Smith et al. (2001) suggested that CO₂ frost should not be thicker than a few meters on the surface based on the data collected by Mars Orbiter Laser Altimeter.

Ground penetrating radar has never been used to measure directly changes in CO₂ frost thickness on the surface of Mars until this investigation. This study first focuses on developing a visual and interpretation method for the SHARAD data in Kingdom Suite, which is a seismic visualization and interpretation software by Seismic Micro-Technology (SMT). This study then extracts all the necessary information from interpretation done in Kingdom Suite to analyze the changes in SHARAD signal characteristics owing to seasonal cycles in the south Polar Layered Deposits (PLD). The basis of this investigation is the hypothesis

whether the signal travel time and amplitude can monitor CO₂ thickness changes in different seasons due to accumulation and withdrawal of the water ice and CO₂ frost.

The analysis provides understanding on how the variation of the CO₂ frost thickness through different seasons affects the SHARAD signal travel time and amplitude characteristics. The signal travel time and amplitude variations are used to quantify the change in CO₂ frost thickness on the surface.

Chapter 2: Field Site Selection, Data Acquisition and Processing

2.1 Field site selection and data acquisition

Fifty seven datasets were selected to analyze possible SHARAD signal changes that occurred during seasonal cycles for this investigation. These datasets were collected over a two-and-a-half-year period from January 31, 2007 to July 25, 2009, which is equivalent to 1.5 Martian years. The datasets selected for this project are shown in Appendix A. Each dataset represents one continuous orbital track. These datasets are approximately distributed evenly throughout the one-and-a-half-Martian-year time span to ensure that there are not any large time gaps in between datasets. The target area for this investigation consists of the region covered by all the orbital tracks, which are shown as blue lines in the digital elevation model provided by MOLA in Figure 2.1.

This investigation requires high quality and reliable data. Because of this, choosing a field site at the south Polar Layered Deposit (PLD) was difficult. Subsurface reflections at the south PLD are not continuous and widespread like reflections present at the north PLD, which are present everywhere. Reflections at the south PLD are extremely localized at specific areas (Phillips et al., 2010). Figure 2.2, as an example, shows no reflections on the right side of the radar

cross-section, which is typical in all the datasets from the south PLD. The target area chosen for this investigation at the south PLD (Figure 2.1) has a relatively flat surface topography and exhibits minimal sources of surface clutter, such as craters or rough topography, which would scatter radar energy and potentially decrease the data quality. The datasets that were acquired over this area provide relatively strong, coherent, and traceable reflections (Figure 2.2). These reflections occur due to sufficient dielectric contrasts between each layer, which may indicate the variation of dust and sand content within the layers (Kelly et al., 2006).

SHARAD's hardware configuration for data acquisition is similar to any other GPR systems with a slight alteration for the MRO mission. Seu et al. (2007b) provides more detail about the instrument's hardware. SHARAD consists of a transmitter, a receiver, and a SHARAD electronic box. The other components outside the SHARAD electronic box are the antenna, data storage and power supply. The antenna is a 10-m dipole connected to the SHARAD electronic box and is used to radiate high-energy pulses generated by the transmitter and also receives energy reflected from the Martian surface and subsurface. The transmitter is designed to amplify chirped pulses with a center frequency of 20 MHz with a 10 MHz bandwidth, to switch the antenna between the transmitting and receiving modes, and to maintain communication with the antenna during data acquisition. The receiver amplifies the return signals for A/D (analog to

digital) conversion, applies a band-pass filter and digitizes the received signals. The SHARAD electronic box stores and executes information, such as survey parameters, timing and instrument control, low-power linearly-frequency-modulated chirped pulse generation for the transmitter, and onboard data processing routines. This unit ensures that SHARAD's components are working properly. The power supply is also controlled by the SHARAD electronic box to provide a steady high energy output during data acquisition. Data are formatted and stored in a solid state recorder on MRO after onboard digital signal processing.

According to the MRO operation strategy, data acquisition for SHARAD is usually not interactive and has to be scheduled in advance. SHARAD is highly programmable for different survey parameters and on-board data processing (Alberti et al., 2007). Target locations and time of data acquisition for SHARAD is planned and determined by the SHARAD team. SHARAD occasionally collects data during the daytime as part of the main MRO mission's objectives to image the north and south PLDs. SHARAD acquires data primarily at night because the ionosphere effect is minimal to the radar and requires almost no correction due to the ionosphere effect. It also does not interfere with operations from other instruments onboard (Seu et al., 2007b). During the MRO mission, SHARAD occasionally does not collect data when the radar's antenna points more than 10

degrees off nadir because SHARAD has been designed to collect useable data only within 10 degrees of the nadir looking direction.

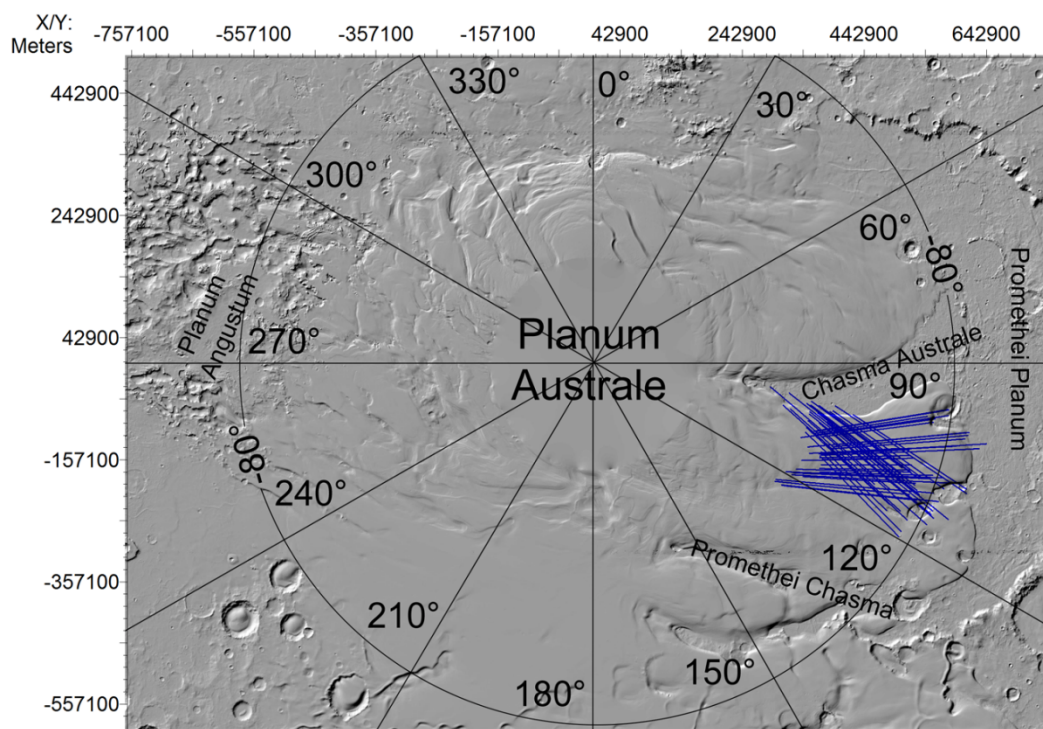


Figure 2.1 The target area for this investigation at the south PLD on Mars. Blue lines show the orbital tracks used in this study.

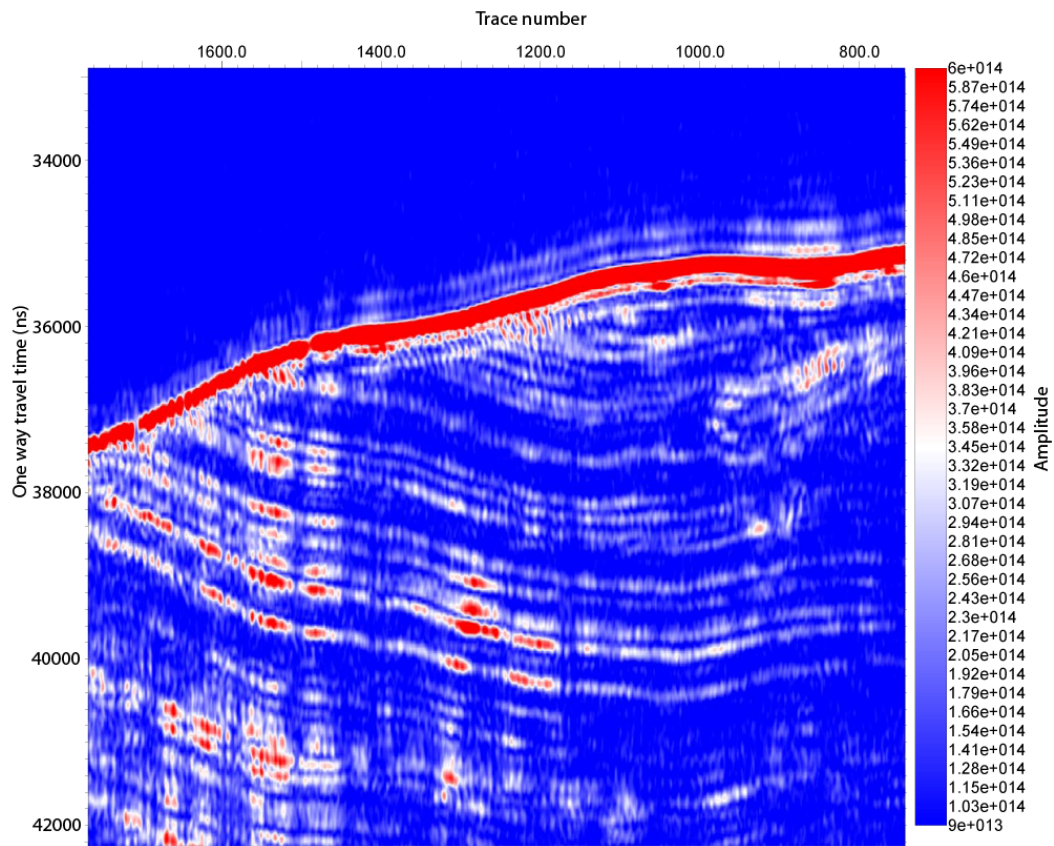


Figure 2.2 An example of a radar cross-section (track #5570) in time domain. Red color represents higher amplitudes; blue color represents lower amplitudes.

2.2 SHARAD data processing

Data processing has been completed by the SHARAD team and the data products are available for download from the SHARAD team server. This section describes what processing has been applied to the SHARAD data by the SHARAD team.

Both antenna theory and digital signal processing concepts play an important role for SHARAD imaging from a long range as a synthetic aperture radar (SAR). In order to differentiate Martian subsurface layers with sufficient resolution from long range, wavelengths of the transmitted pulses have to be extremely short, an antenna has to be impractically long, or both (Stimson, 1998). However, the energy of short wavelengths attenuates rapidly during transmission. A large amount of power thus is needed for pulse transmission from a long range. The power requirement for direct pulse transmission exceeded the power capacity of the MRO. The antenna length is often limited by the orbiter's dimensions and imaging from a long range requires an impractically long antenna (hundreds of meters) to produce a sufficiently narrow beam. These limitations can be resolved by building a 10-meter physical antenna, synthesizing a long antenna aperture or array for data acquisition, and applying signal processing routines, as the antenna takes advantage of the moving MRO around the Mars orbit. Digital signal

processing onboard and on the ground is performed after data acquisition to increase spatial resolution and signal-to-noise ratio.

As the MRO moves along its orbital track during data acquisition, pulses are being transmitted at the pulse repetition frequency (PRF) of 700 Hz, which is over-sampled spatially (Seu et al., 2007b). For every kilometer, the number of pulses collected is

$$\# \text{ pulses} = \approx \frac{d}{v_{s/c}} * PRF = \frac{1000 \text{ m}}{3400 \frac{\text{m}}{\text{s}}} * 700 \text{ Hz} \approx 206 \text{ pulses}$$

where d is the horizontal distance, $v_{s/c}$ is the spacecraft horizontal velocity, and PRF is pulse repetition frequency. Using this PRF and an 85 microsecond recording length for each pulse result in a massive amount of data being produced for every orbital track. On-board processing is therefore carried out to reduce the data size before data is downloaded to the ground for additional processing. SHARAD's on-board digital electronic unit is able to perform coherent integration or stacking to reduce the amount of data. The radar system can integrate from 1 to 32 pulses coherently into a single composite trace for each location along the orbital track (Alberti et al., 2007; Slavney et al., 2007). This process reduces the data volume and also helps to increase the signal-to-noise ratio (SNR) by summing coherent pulses together. The amplitude and phase of these composite traces do not suffer from destructive interference, as long as all

the pulses' spatial locations are within the azimuth resolution (Seu et al., 2007b). After data has been downloaded, further digital signal processing must be performed to maximize along-track and range resolution and SNR (Figure 2.3). Studies by Seu et al. (2007b) and Alberti et al. (2007) explain in greater detail the SHARAD spatial resolutions and data processing.

F-k focusing (also referred to as synthetic aperture focusing or Doppler focusing) is used to improve along-track resolution (Alberti et al., 2007). Without any focusing, the along-track resolution should be approximately between the diameter and twice the diameter of the Fresnel zone (Seu et al., 2007b). The diameter of the Fresnel zone is

$$D_{FZ} = 2 * \sqrt{\frac{\lambda R_0}{2}} = 2 * \sqrt{\frac{0.015(km) * 300(km)}{2}} = 3.00 \text{ km}$$

where R_0 is the distance between the MRO and the Martian surface and λ is the wavelength of the 20 MHz center frequency. Therefore, the along-track resolution without any focusing is approximately 3 – 6 km, which is very poor and is the same as the cross-track resolution. With synthetic aperture focusing, the along-track resolution (ρ_a) is improved dramatically without deteriorating the SNR

$$\rho_a \approx \frac{\lambda R_0}{2D_{FZ}} = \frac{0.015(km) * 300(km)}{2 * 3} = 0.750 \text{ km}$$

where R_0 is the distance between the MRO and the Martian surface, λ is the wavelength of the 20 MHz center frequency, and D_{FZ} is the diameter of the Fresnel zone. The along-track resolution receives an approximate 4 times finer improvement from 3.00 km to 0.750 km with synthetic aperture focusing (Seu et al., 2007b). With this along-track resolution, more pulses can be summed coherently to maximize SNR, beyond what was first done on-board. The number of pulses, which can be summed together, are calculated using

$$\# \text{ pulse summed} \approx \frac{\rho_a}{v_{s/c}} * PRF = \frac{750 \text{ m}}{3400 \frac{\text{m}}{\text{s}}} * 700 \text{ Hz} \approx 150 \text{ pulses}$$

where $V_{s/c}$ is the spacecraft horizontal velocity and ρ_a is the diameter of the Fresnel zone after focusing. The on-board pre-summing can only sum up to 32 pulses within this azimuth resolution (750 m) and is not focused. The calculation shows that 150 pulses can be coherently summed to further increase SNR on the ground processing without any destructive interference (Seu et al., 2007b). However, phase errors should arise during pre-summing or focusing if more than 150 pulses are summed, which exceed the azimuth resolution. Phase correction should be performed before summing by shifting the phase of each pulse in the frequency domain accordingly, which is equivalent to adding delay in the time domain. All the pulses should be in phase in the frequency domain after phase shift and are coherently summed in the frequency domain (Alberti et al., 2007).

The SHARAD data presented in this investigation have applied a f-k focusing routine with an aperture length of 4096 pulses, which also represents the length of the synthesized antenna of 160 km long. Phase corrections have been taken into account before focusing (Egan, A.F., personal communication, December 5, 2010).

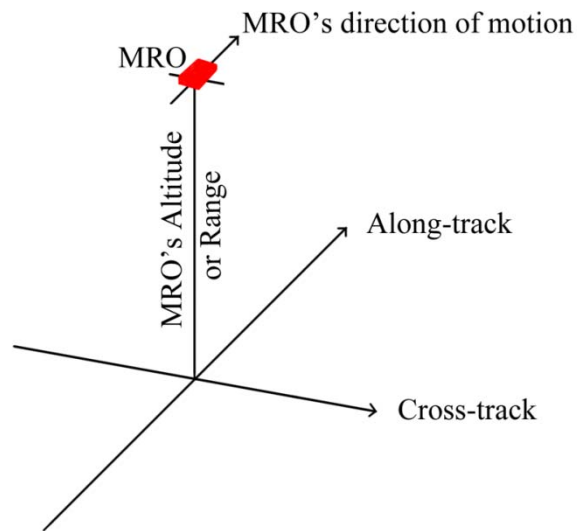


Figure 2.3 MRO/SHARAD orientations in space. Along-track is parallel to the MRO's direction of motion and cross-track is perpendicular to the MRO's direction of motion.

Another spatial resolution besides azimuth resolution that needs to be improved is range. Finer range or vertical resolution can be achieved by performing pulse compression, range compression, or cross-correlation.

Transmitting short pulses to achieve the desired vertical resolution from a long range requires a large amount of power in a short instant, which the MRO cannot provide. Therefore, signals would not have enough power to reach the targets and reflect back to the antenna. Transmitting linear frequency modulated (chirp) signals would compensate for this problem. SHARAD is able to generate a wide bandwidth chirp from 15 to 25 MHz, which allows more time for additional energy to be sent out and lowers the peak power requirement. For each returned pulse, pulse compression (a matched filter) is applied to the transmitted pulse, which is simply a multiplication in the frequency domain after Fourier transform is applied for both pulses. The transmitted pulse consists of the chirp signals multiplied by a Hanning filter in the frequency domain after the Fourier transform. The Hanning filter is applied to the chirp signal so that the effects from sidelobes can be reduced. However, bandwidth and returned pulses' strength are decreased because both sides of the chirp signals are forced to become zero by the Hanning filter applied. The results of an inverse Fourier transform is the compressed returned pulses. Reflections from the Martian surface and subsurface can be resolved, especially those that are closely spaced in time. This processing is equivalent to applying a cross-correlation in the time domain to compress pulses.

Another correction for the returned pulses is for the ionosphere effect, which would distort the radar signal. If the solar zenith angle is above 90° , which the Sun is above the horizon, an additional Chapman ionosphere correction must

be applied for the sunlit portion of the orbit track (Egan, A.F., personal communication, December 5, 2010).

2.3 Data editing

Interpretation of the SHARAD data was completed in Kingdom Suite, which is a 2-D and 3-D geologic interpretation software specifically designed for seismic data. This software did not support the SHARAD data format as it was originally provided. Modifications necessary to alter the original format in to a form compatible with Kingdom Suite are explained below. After all of the selected SHARAD datasets were downloaded from the SHARAD team server, SHARAD subsurface imaging data were extracted from the datasets by running a script written in Interactive Data Language (IDL). The script, which is presented in Appendix B, was executed to extract individual traces and their corresponding geographic coordinates. A 2-D array was created to store the amplitude information for all the traces extracted from each data product. Each column in the array represented a trace and each row represented a sample point in each trace. There were 4096 sample points in each trace and the number of traces varied between each datasets. There were between eighteen to thirty six thousand traces in each dataset. Traces which did not contain subsurface returns were removed from the analysis, resulting in three to four thousands traces per dataset. Phillip et al. (2010) followed a similar approach in his subsurface study at the

south PLD, noting that reflections from the subsurface are localized and some areas showed from incoherent and discontinuous to no reflections from the subsurface. Similarly, subsurface reflections were not always present throughout the entire orbital track in this investigation in the south polar area. All the remaining traces in the 2-D array, those which exhibited strong traceable reflections from the subsurface, were written to a file in the ASCII format with a tab separation for each sample value. The geographic coordinates corresponding to those traces were written to a separate ASCII file in the CSV format.

The data files in ASCII format were then loaded into MATLAB and were converted to SEG-Y (Society of Exploration Geophysicist, 2002) format using SegyMAT (Hansen, 2010). SegyMAT, which is an open source application, had a set of MATLAB scripts for reading and writing SEG-Y format from MATLAB. In order to load the SHARAD data properly into Kingdom Suite, a slight change was made in the default parameters. The data sample format code was changed from 5 (4-byte IEEE floating point) to 1 (4-byte IBM floating point). In addition, the sampling rate (Δt) of the SHARAD data was adjusted from 0.004 s (the default) to 0.00375 s. The actual sampling rate (37.5 ns or 26.6667 MHz) could not be used because SEG-Y files do not support such a small time sample interval. Therefore, the actual rate was multiplied by 10^5 when the data were being converted into SEG-Y format and were converted back to the actual value after

the data were loaded into Kingdom Suite. The MATLAB script for loading the data files and converting the data into SEG-Y is presented in Appendix C.

Before all the SEG-Y files can be loaded into Kingdom Suite for analysis, coordinates for each trace had to be converted from an angular unit (degrees) to meters using ArcGIS (ArcMap). Coordinate systems available in ArcMap were able to complete this transformation. The spherical coordinates were loaded by using the geographical coordinate system (Mars 2000) and was transformed by using the projected coordinate system (Mars Spolar Sphere Polar). The unit after transformation became meter, which made importing SHARAD data into Kingdom Suite relatively straight-forward. With all of the coordinates in the correct unit and the SHARAD data in the SEG-Y format, the data could be imported into Kingdom Suite. These steps are illustrated in Appendix D.

Chapter 3: Data Analysis and Interpretation

3.1 Horizon identification and picking

The main objective of this investigation is to look for possible changes in SHARAD signals when the surface elevation of the south polar cap varies during different seasons. The south polar ice cap advances toward the equator during the southern winter and retreats toward the pole during the southern summer. During winter, CO₂ frost accumulation increases surface elevation and therefore, signals travel shorter distances in the Martian atmosphere. During summer, CO₂ frost withdrawal decreases surface elevation and signals travel longer distances in the Martian atmosphere. Therefore, signal travel time is first analyzed and the approach for this analysis using Kingdom Suite and MATLAB is presented in this chapter.

Kingdom Suite by Seismic Micro-Technology (SMT) is a seismic interpretation software that allows the display of subsurface cross-sections and the picking (interpretation) of horizons. In Kingdom Suite, all orbital tracks are loaded and positioned according to their appropriate locations. The base map created in Kingdom Suite is shown in Figure 2.1. The blue lines represent all the orbital tracks that are chosen for this study. Figure 2.2 shows an orbital track as an

example that is composed by 1020 vertical traces. Each vertical trace contains 4096 time samples with the amplitude information attached. Each trace also has an individual trace number and geographic coordinates for locating its position. The vertical axis in Figure 2.2 represents the one way travel time in nanoseconds and the horizontal axis marks the trace numbers. The amplitude information in each trace is shown in color from red (high in amplitude) to blue (low in amplitude). Figure 2.2 also shows multiple subsurface reflections.

In order to compare seasonal travel time variations attributed to CO₂ frost and water ice thickness variability, I examine orbital tracks that are in close spatial proximity but acquired in different seasons.

To eliminate travel time uncertainty associated with variations in atmospheric conditions, such as the ionosphere effect due to the Sun, between seasons, SHARAD cannot be used as an altimeter measuring the travel time directly between the instrument and the Martian surface. A subsurface reflection is picked as a common reference datum on all the orbital tracks to assess relative travel time changes between surface reflections over varying seasons.

For the travel time analysis first I identify the surface and one subsurface reflection for each orbital track. The subsurface reflections from the twelve orbital tracks shown in Figure 3.1 are used as the reference horizon for assessing changes in the travel time of the surface reflections. These twelve orbital tracks were

chosen because of their consistently strong and traceable surface and subsurface reflections across the area outlined by the red box in Figure 3.1. The red box, where all twelve orbital tracks intersected each other and was this investigation's focused area, was approximately 22 km long and 15 km wide.

Recognizing and mapping a surface reflection was essential for analyzing the change of surface elevation. The yellow horizons interpreted in Figures 3.2 and 3.3 represent the Martian surface reflection. The reflection at the Martian surface is always the strongest in amplitude because approximately one-third of the SHARAD signal energy was reflected there, where the dielectric property of the materials changes sharply from the Martian atmosphere to the ground ice. The green horizons represent the subsurface reflection. The subsurface reflection appears relatively consistent throughout the same area compared to other subsurface reflections on the same orbital track. It is also found on ten other orbital tracks. The surface horizons are relatively easy to pick because of the strong amplitude responses and their continuity throughout the entire length of the orbital track. Subsurface reflections, in contrast, are difficult to pick because their amplitude responses are sufficiently weaker due to the signal's energy attenuation and relatively discontinuous reflections.

The Kingdom Suite's Auto-pick – 2D Hunt was used to pick the majority of the horizons to enhance the level of accuracy while picking horizons manually

was still necessary sometimes to connect gaps along the reflection. 2D Hunt was set to pick maximum amplitude values along each reflection on all orbital tracks within the guided window. The amplitude threshold and the guided window length were set to 0.9 (default was 0.5) and 150 ns respectively. 2D Hunt picks automatically when the current amplitude value was less than $\pm 10\%$ of the average amplitude from the past five values and was located inside the 150 ns guided window length. The small amplitude threshold and guided window length ensured that the automatic horizon picks tracked along the same reflections; therefore enhanced the level of accuracy for the results. Horizon picking was done to all twelve orbital tracks and are presented in Appendix E with a fixed amplitude scale for direct comparison in amplitude.

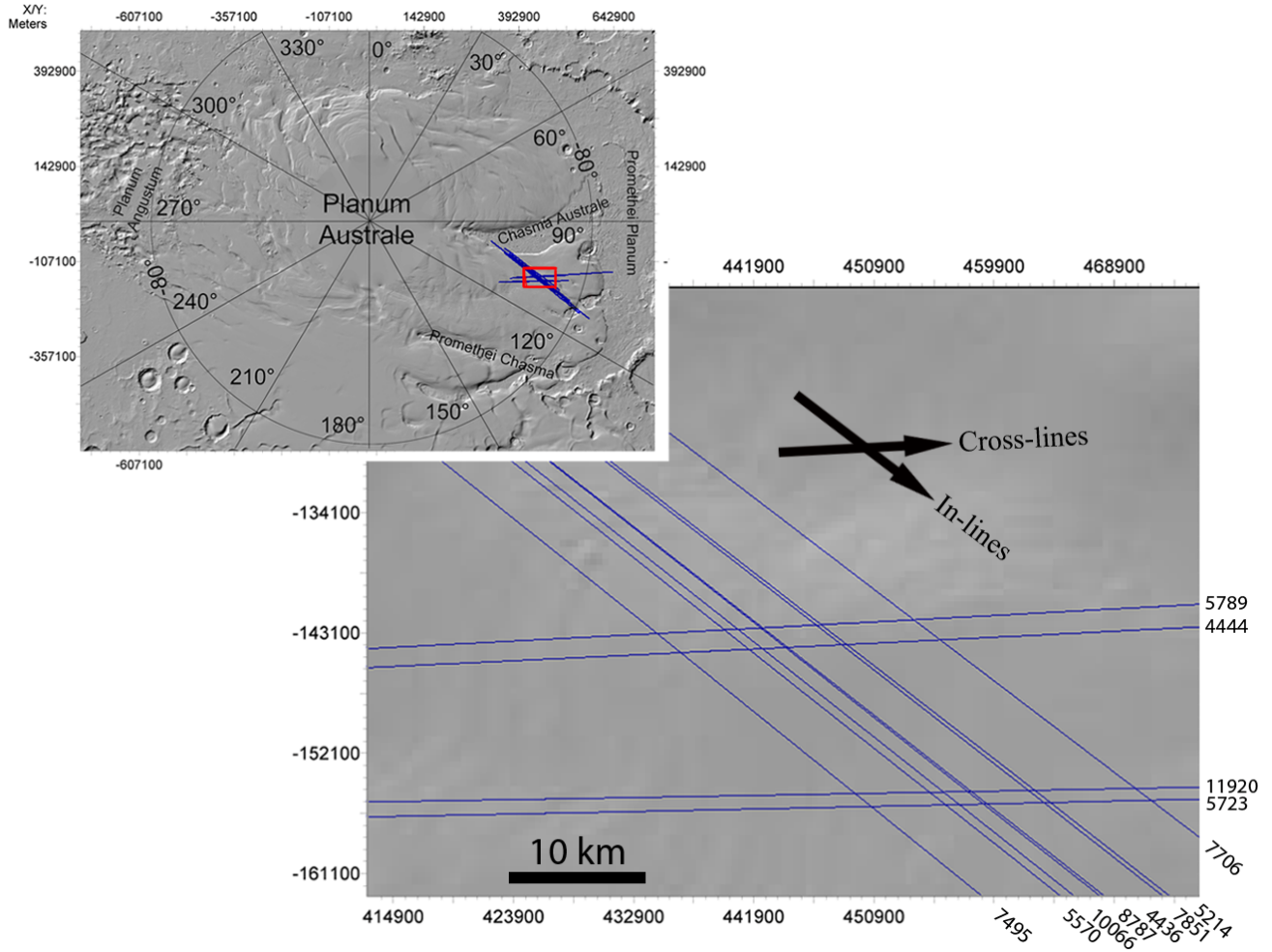


Figure 3.1 Twelve orbital tracks were chosen for the analysis. The red box shows where the tracks intersect one another. There are eight in-lines (7495, 5570, 10066, 8787, 4436, 7851, 5214, and 7706) and four cross-lines (5789, 4444, 11920, and 5723). The orbital tracks are labeled in the expanded image in the lower right corner.

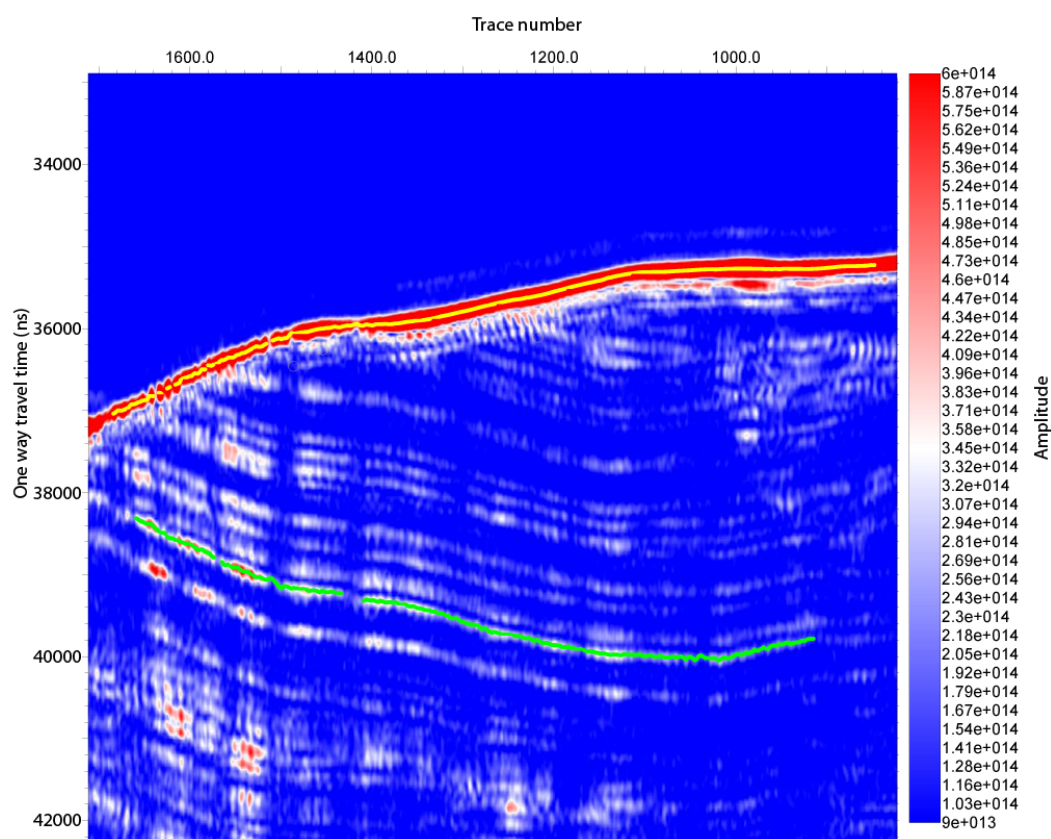


Figure 3.2 Surface and subsurface horizon picks along orbital track 8787

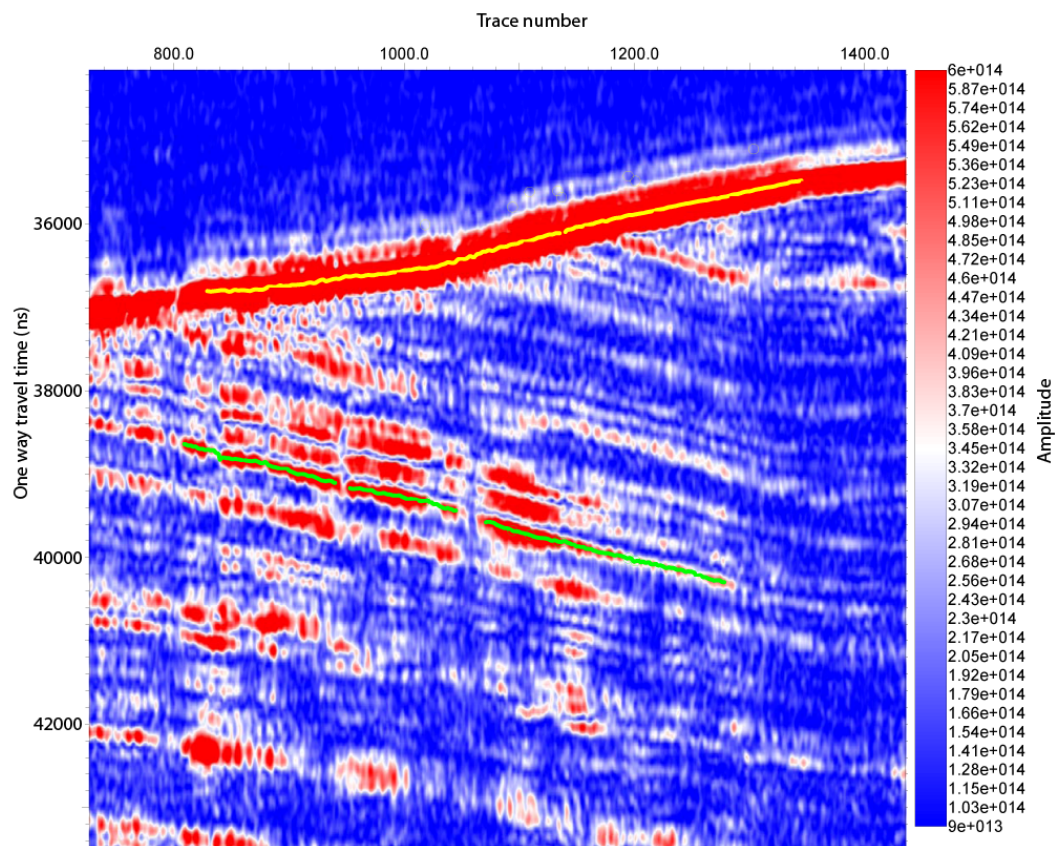


Figure 3.3 Surface and subsurface horizon picks along orbital track 11920

3.2 Track alignment

Seasonally varying atmospheric conditions could introduce travel time differences between orbital tracks. Those time differences result in orbital track misalignment which needs to be corrected. To correct for SHARAD signal propagation changes due to atmospheric conditions, the intersecting orbital tracks are shifted in time so that the subsurface horizons are completely aligned with the subsurface horizon of cross-line 11920, which is a reference horizon for the travel time analysis of the surface reflections of the intersecting lines. The surface horizons of each in-line are now placed in a correct position in time relative to other in-lines along the same cross-line. In Figure 3.4, yellow and green horizons represent the interpreted surface and subsurface horizons along cross-line 11920. The yellow and black dots are interpretations of the same horizons along intersecting lines acquired in different seasons. The alignment results show that the yellow dots do not line up with the surface horizon along cross-line 11920. Furthermore, the surface horizons have varying time differences among all the in-lines. Such misalignment and time differences between each in-line are also observed for in-line 8787 (Figure 3.5) and suggest seasonal surface layer elevation variability. Since the data for each of the orbital tracks were collected at different times throughout a Martian year, the above observations indicate the travel time differences after datum adjustment (orbital track leveling) are caused by seasonal variations.

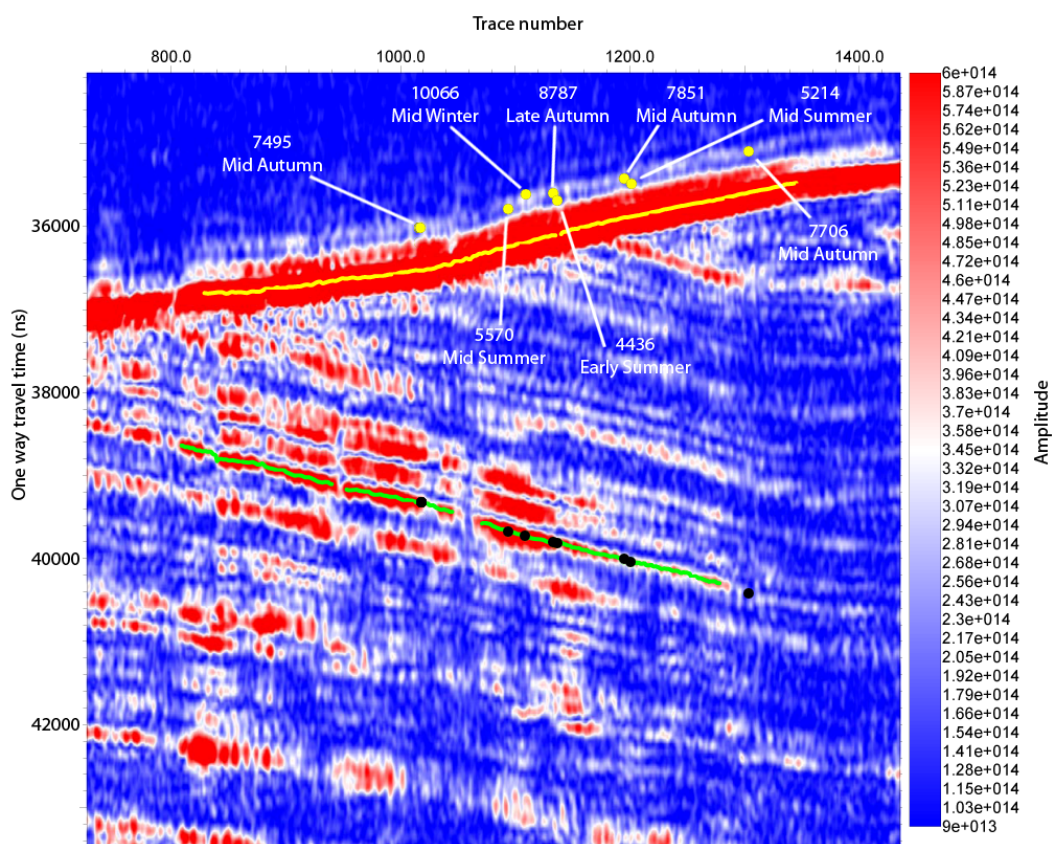


Figure 3.4 Cross-line 11920 with the subsurface horizon (green) aligned with all the intersecting in-lines' subsurface horizons (from left to right): 7495, 5570, 10066, 8787, 4436, 7851, and 5214. The cross-line is used to level the in-lines and to assess relative change in elevation due to seasonal variation between the intersecting in-lines.

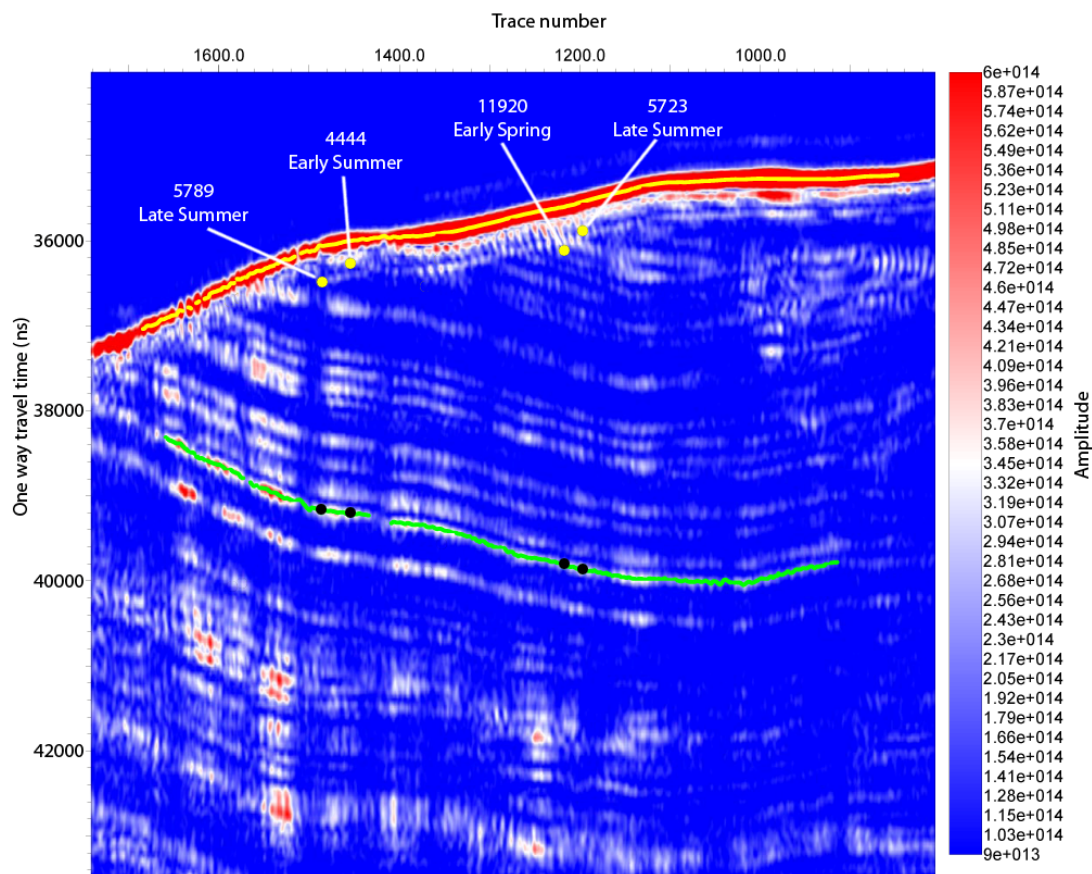


Figure 3.5 In-line 8787 with the subsurface horizon (green) aligned with all the intersecting cross-lines' subsurface horizons (from left to right): 5789, 4444, 11920, and 5723. Elevation varies seasonally among the intersecting cross-lines.

3.3 Data management

From Kingdom Suite, a surface horizon and a subsurface horizon picked for each of the twelve orbital tracks are extracted into comma-separated value formatted files (CSV). Each CSV file contains properties for each trace along one horizon. A CSV file for the surface horizon and a CSV file for the subsurface horizon from the same orbital track are then loaded into MATLAB and merged together by matching traces from each CSV file. Traces' properties are extracted after traces are matched between the surface horizon and the subsurface horizon for all twelve orbital tracks. A matrix in MATLAB is created to store the traces' properties for each of the twelve orbital tracks. The matrix for each orbital track consists of (1) columns of data for surface and subsurface horizons of each trace and (2) rows of data for each trace along a horizon.

Data in columns 1-4 are the same for both the surface and subsurface horizons. The data in columns 5 and 6 are extracted from the CSV file for the surface horizon while the data in columns 7 and 8 are extracted from the CSV file for the subsurface horizon. The data types are listed in Table 3.1. The MATLAB script is written to generate the data matrix for each orbital track in MATLAB and is attached in Appendix F (Script 1).

Column #	Data type stored in each column
1	X coordinate in meters
2	Y coordinate in meters
3	Orbital track number
4	Trace number
5	Time (surface horizon) in nanoseconds
6	Amplitude (surface horizon)
7	Time (subsurface horizon) in nanoseconds
8	Amplitude (subsurface horizon)

Table 3.1 Data types stored for each trace along each orbital track in data matrix in MATLAB

3.4 Travel time analysis

Based on the surface horizon travel time misalignments identified between each in-line in Chapter 3.2, the time differences between both surface horizons at each interaction are computed to estimate the changes in surface elevation at each intersection. The travel time difference at each intersection was then plotted against the solar longitude (Ls) of the in-lines.

As Figure 3.1 shows, each cross-line intersects with eight in-lines. For each intersection point, the distance between the nearest in-line and cross-line traces is determined following steps 1 and 2 below:

1. Starting from one end of the in-line to another, measured the distances between the first cross-line trace and all in-line traces.
2. Repeated step 1 for the next trace on the cross-line and continued to the last trace on the cross-line.

The following equation is used to calculate the distances of the in-line and cross-line trace pairs

$$d = \sqrt{(x_2 - x_1)^2 + (y_2 - y_1)^2}$$

where d is the distance of a trace pair, x_1 and y_1 are the coordinates of a cross-line trace, and x_2 and y_2 are the coordinates of an in-line trace.

The in-line and cross-line trace pairs that have the shortest distances to each intersection are then identified (see Figure 3.6 for illustration). At most orbital track intersections traces considered for the analysis are about 30 m apart. There are only a few intersections in which traces are ~50 m away from each other. Data in the MATLAB matrix for the identified in-line and cross-line trace pairs are reorganized into the data types listed in Table 3.2 to form a trace pair data matrix.

Column 1 in Table 3.2 shows the distance for the identified in-line and cross-line trace pairs. Columns 2 to 9 are the data for the cross-line trace while columns 10 to 17 are the data for the in-line trace. Each row in this trace pair data matrix represents each intersection.

In order to calculate the travel time differences between the surface horizons of the cross-line and of the in-line at each intersection, the travel times from the subsurface horizons of the cross-line and in-line are adjusted to a datum as a reference horizon (Figure 3.7). The adjustments are made as the following:

1. The black lines represent the surface and subsurface horizons of the cross-line and in-line.
2. The subsurface horizons of the cross-line and in-line are adjusted to the datum. The surface horizons of the cross-line and in-line are then adjusted with the same travel time adjustments for the

subsurface horizons (travel time x for the cross-line and travel time y for the in-line).

3. The blue lines represent the adjusted surface and subsurface horizons of the cross-line and in-line.

After the travel time adjustments are made, one-way travel time difference (Δt) at each intersection is calculated by subtracting the one-way travel times between the adjusted cross-line and in-line surface horizons (Figure 3.8). The Δt value for each intersection is stored in column 18 in the trace pair data matrix (Table 3.2).

The Δt values, which is a one-way travel time, for each intersection are plotted against the solar longitude (Ls) in Figure 3.9 to show the changes in surface elevation through Δt over different seasons. Figure 3.10 illustrates the solar longitude with respect to different seasons.

Each Δt value is converted from time to depth using the equation below

$$\Delta d = \frac{c\Delta t}{2\sqrt{\epsilon}}$$

where Δd is the thickness in meter between cross-line and in-line surface horizons at the intersection, c is the speed of light in free space, Δt is the one-way travel

time difference in nanoseconds, and ϵ is 2.12, which is the dielectric constant of CO₂ frost measured by the Time Domain Reflectometry (Pettinelli et al., 2003).

The results of the changes in CO₂ frost thickness in meters at all eight interactions are stored in column 19 in the trace pair data matrix in MATLAB (also see Table 3.2) and plotted against solar longitude (Ls) in Figure 3.11. The MATLAB script for the travel time analysis is attached in Appendix F (Script 2).

One observation made in Figure 3.11 based on the base map in Figure 3.1 and orbital track 11920 (Figure 3.4) is that there are three pairs of in-lines along cross-line 11920 that are close to each other in space and both in-lines in each pair were acquired in different seasons –5214 (*) and 7851(*), 4436 (+) and 8787(+), and 5570 (Δ) and 10066(Δ). Direct comparison of seasonal changes in CO₂ thickness within each pair becomes possible in this case because both in-lines in each pair are close to each other in space and they have been shifted to a common datum. Intersecting in-lines from each pair along cross-line 11920 that were acquired during fall and winter (7851, 8787, and 10066) shows greater thickness than those that were acquired during summer (4436, 5214, and 5570). The differences of CO₂ thickness between seasons on cross-line 11920 is as followed:

- Mid summer (5214) to mid fall (7851) = 6.90m
- Early summer (4436) to late fall (8787) = 7.93m
- Mid summer (5570) to mid winter (10066) = 14.1m

In-lines 7706 ($L_s = 46.87$) and 7495 ($L_s = 39.51$) are positioned at a distance from the other in-line orbital tracks (Figures 3.1 and 3.4) and therefore, significant topographic changes prevent direct comparison of CO_2 thickness change. Hence, both in-lines 7706 and 7495 are discarded from the analysis.

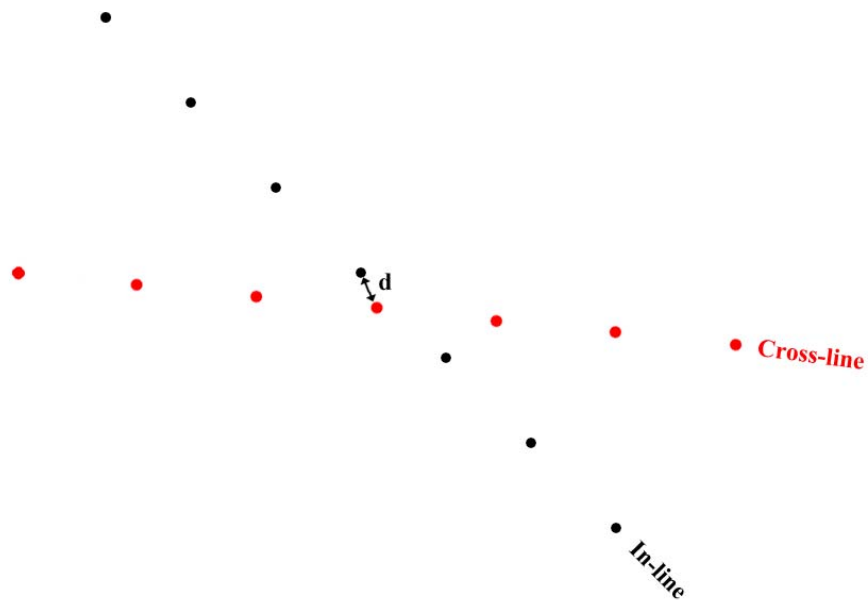


Figure 3.6 The closest traces at an intersection between a cross-line and an in-line. 'd' is the distance between the two traces. Each dot represents a trace.

Column #	Data types stored in each column
1	Min. distance between a trace from a cross-line and a trace from a in-line in meters
2	X coordinate in meters (cross-line)
3	Y coordinate in meters (cross-line)
4	Orbital track number (cross-line)
5	Trace number (cross-line)
6	Time (surface horizon) in nanoseconds (cross-line)
7	Amplitude (surface horizon) (cross-line)
8	Time (subsurface horizon) in nanoseconds (cross-line)
9	Amplitude (subsurface horizon) (cross-line)
10	X coordinate in meters (in-line)
11	Y coordinate in meters (in-line)
12	Orbital track number (in-line)
13	Trace number (in-line)
14	Time (surface horizon) in nanoseconds (in-line)
15	Amplitude (surface horizon) (in-line)
16	Time (subsurface horizon) in nanoseconds (in-line)
17	Amplitude (subsurface horizon) (in-line)
18	Time difference in nanoseconds at an intersection between the surface horizons of the cross-line and the in-line
19	Elevation change in meters

Table 3.2 Data types stored for each trace in the trace pair matrix in MATLAB. Each row in this data matrix represents each of the intersection.

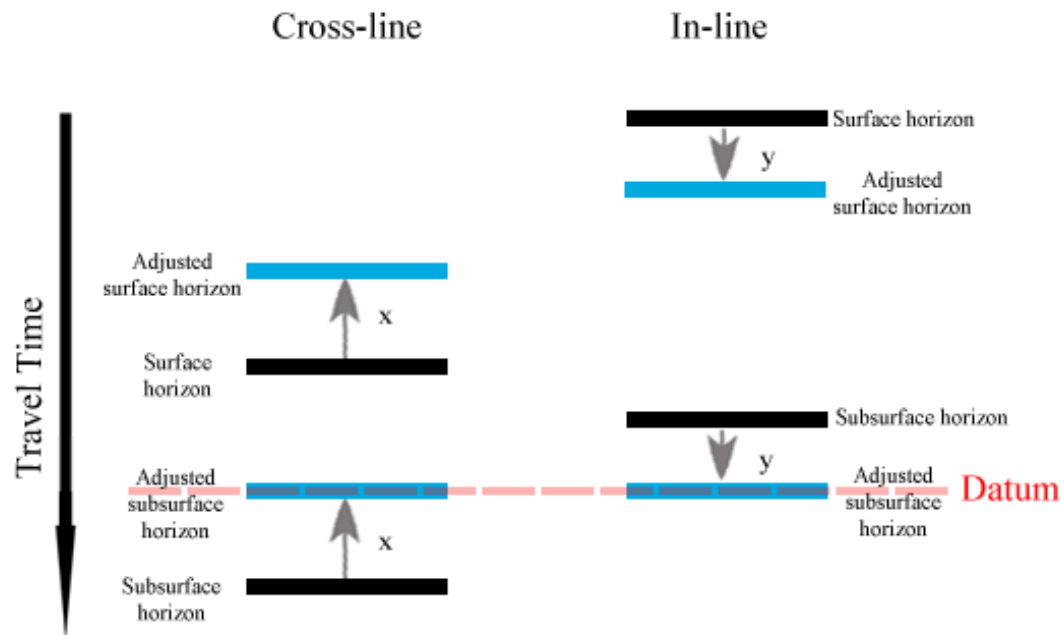


Figure 3.7 Surface and subsurface horizons' travel times are shifted to the datum defined by the subsurface horizon

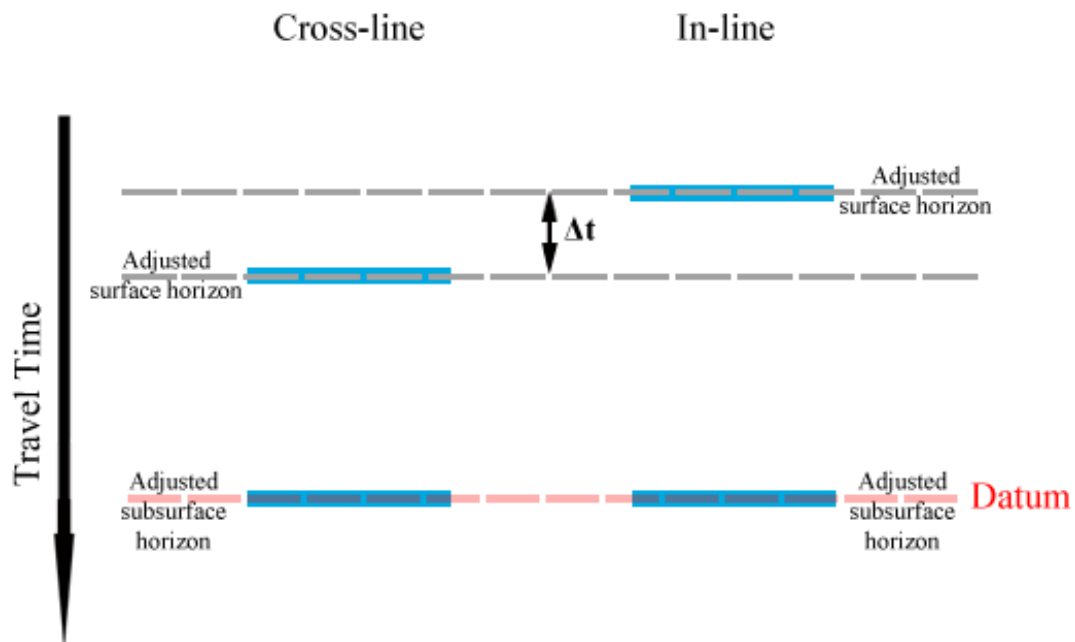


Figure 3.8 Difference in travel time (Δt) was calculated by subtracting between the adjusted cross-line and in-line surface horizons.

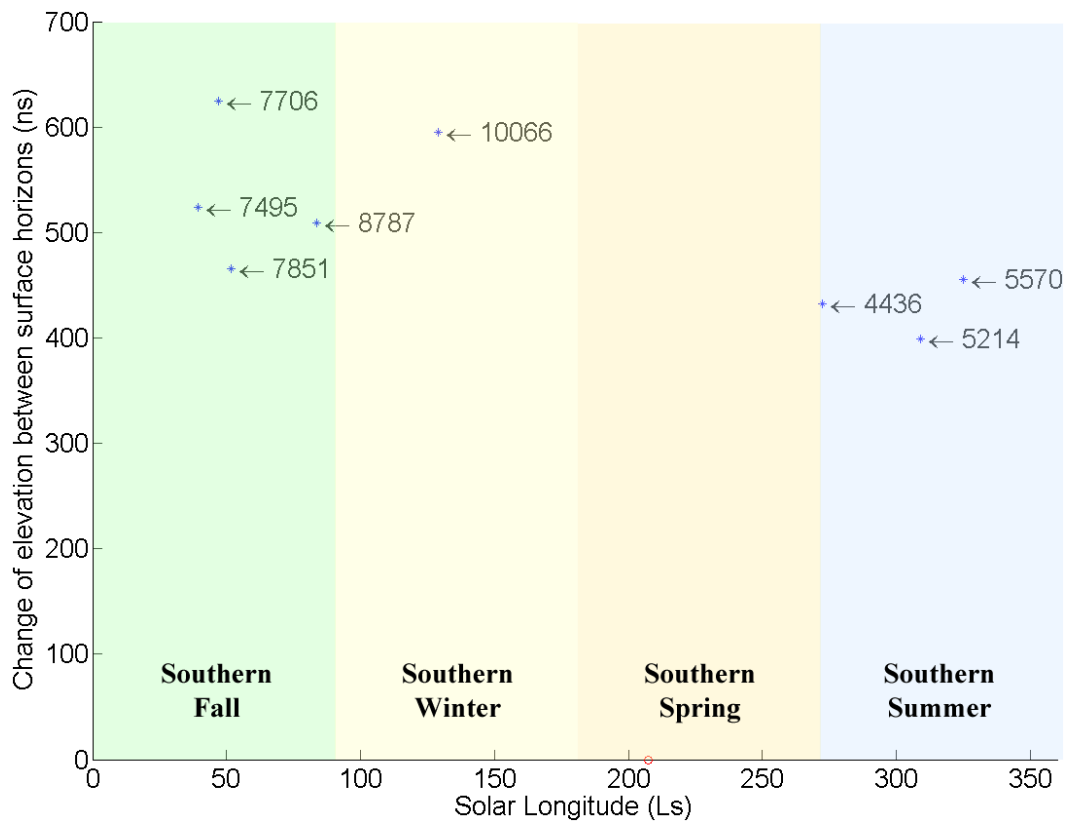


Figure 3.9 Change in surface elevation of each intersecting in-line in time (nanoseconds) relative to the surface horizon of cross-line 11920 is plotted against solar longitude (Ls). The four and five digit numbers next to the arrows correspond to intersecting in-lines. The red circle on the x-axis corresponds to the season when cross-line 11920 was acquired.

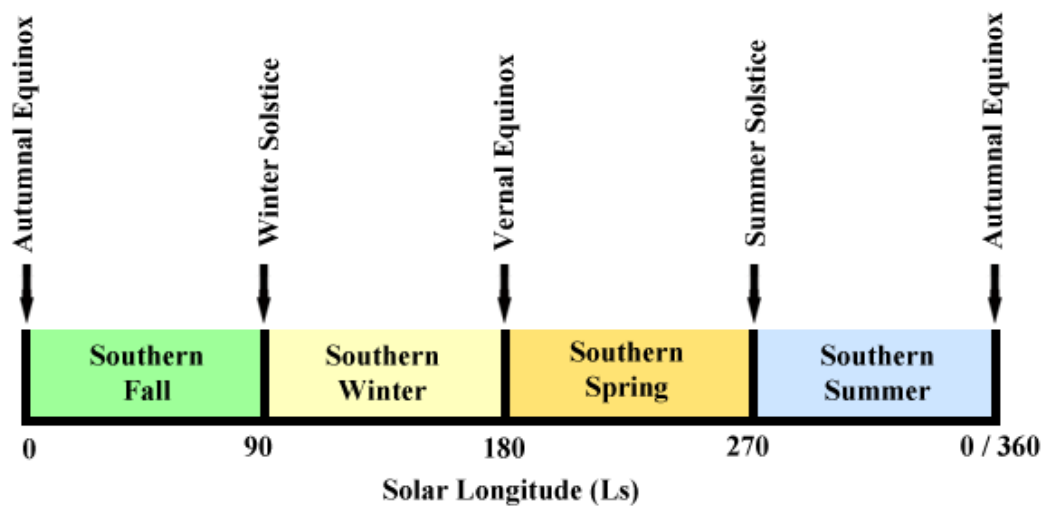


Figure 3.10 Solar longitude is commonly used to delineate different seasons with respect to the position of the Sun on Mars. $L_s = 0^\circ$, 90° , 180° , and 270° represent southern autumnal equinox, winter solstice, vernal equinox, and summer solstice, respectively. Winter solstice ($L_s = 90$) in the southern hemisphere occur when the Sun is farthest north and is the shortest day of the Martian year. In contrast, summer solstice ($L_s = 270$) occur when the Sun is farthest south and is the longest day of the Martian year in the southern hemisphere. Vernal equinox ($L_s = 180$) and autumnal equinox ($L_s = 0$) takes place when the lengths of the day and night are about the same and the Sun is at the celestial equator moving southward and northward, respectively.

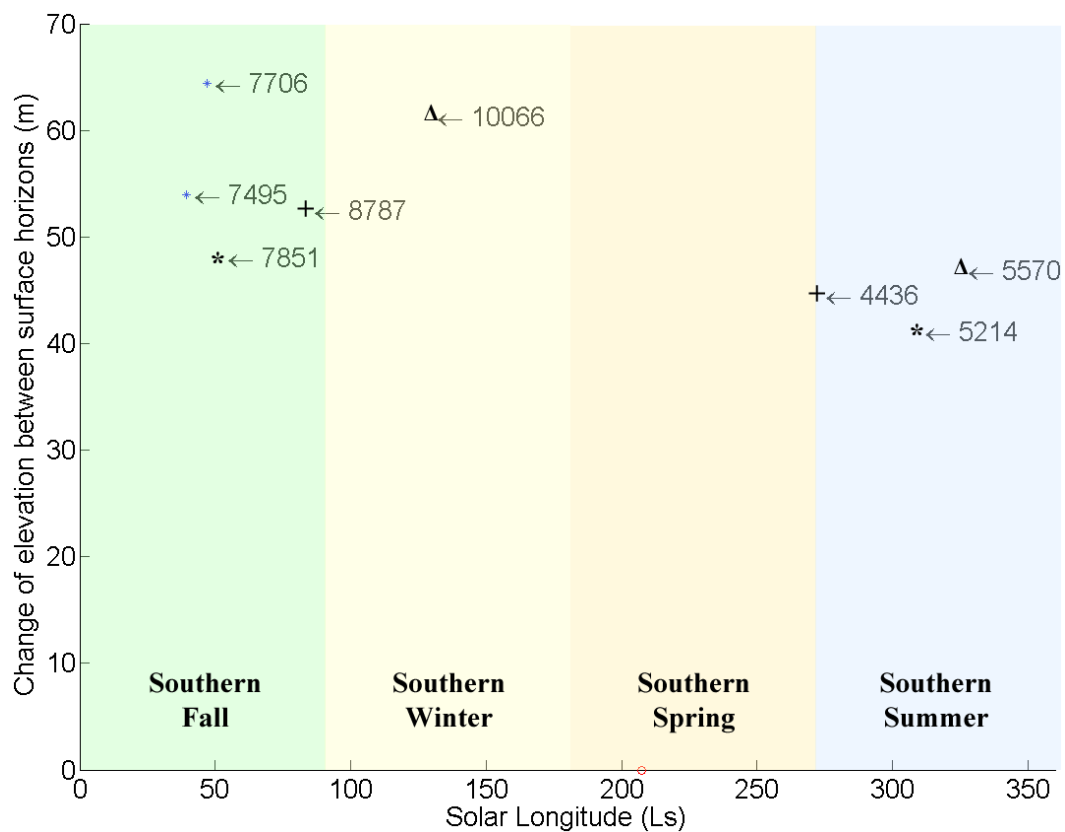


Figure 3.11 Change in surface elevation of each intersecting in-line in meters relative to the surface horizon of cross-line 11920 is plotted against solar longitude (Ls). The four and five digit numbers next to the arrows correspond to intersecting in-lines. Each pair of symbols (*, +, and Δ) indicates that both in-lines are close to each other in space, but they were acquired in different seasons. The red circle on the x-axis corresponds to the season when cross-line 11920 was acquired.

3.5 Amplitude analysis

Amplitude analysis of reflected signals is performed to determine whether seasonal variation affects SHARAD's recorded amplitudes.

Direct comparison of the absolute reflection amplitudes is not possible between surface horizons from each orbital track because recorded signal strength could be influenced greatly by the intensity of the ionosphere effect caused by the Sun (Alberti et al., 2007; Flamini et al., 2007). Since this effect varies based on the time data was acquired and the exposure to the Sun, the SHARAD signal's phase and amplitude values could be distorted. Additionally, surface roughness and MRO direction of motion could be another factor that influences reflected amplitude values. Hence, a relative amplitude comparison method was adopted.

The relative amplitude comparison approach is based on the fact that each surface horizon and subsurface horizon on the same trace should have experienced the same magnitude of ionosphere and surface roughness effects. To cancel these effects, the reflected amplitude value of the surface horizon is divided by the reflected amplitude value of the subsurface horizon on the same trace. This calculation provides a amplitude ratio for each trace.

The amplitude ratios of the (1) cross-line and (2) in-line at each intersection are then calculated. For each intersection, the same traces used in the travel time analysis in Chapter 3.4 are used in the amplitude analysis.

The differences between cross-line and in-lines amplitude ratios are plotted against the solar longitude for each intersection (Figure 3.10) to illustrate the changes in amplitude ratios over different seasons. The MATLAB script for the amplitude analysis is presented in Appendix F (Script 3).

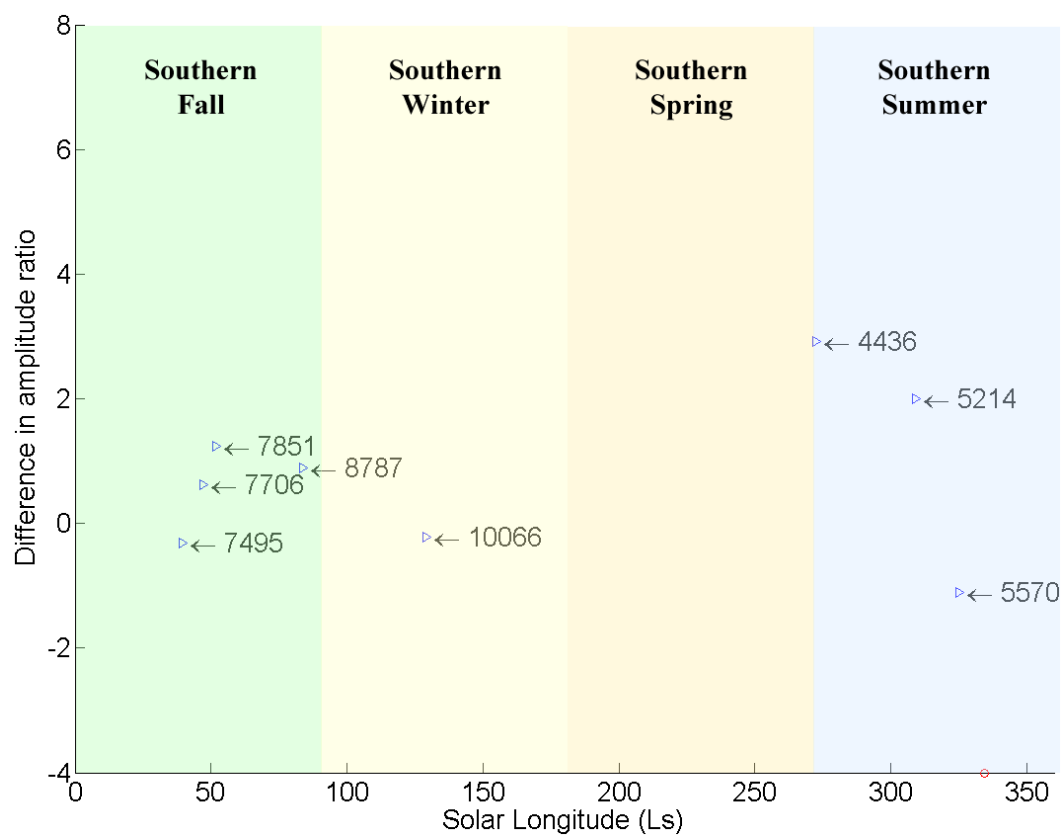


Figure 3.12 Difference in amplitude ratios between each in-line and cross-line 5789. The red circle on the x-axis corresponds to the season when cross-line 5789 was acquired.

Chapter 4: Results and Discussion

4.1 Travel time analysis

In Chapter 3.2 after orbital track leveling to a common datum is performed, surface horizon misalignment in one-way travel time is observed between each intersecting inline. It is hypothesized that the misalignment between the surface horizons of intersecting in-lines was caused by the seasonal variation of CO₂ frost accumulation at the field area. To further investigate the surface horizon misalignment, travel time analysis is used to estimate the one-way travel time difference (Δt) between in-line pairs in close proximity. All Δt values are plotted against solar longitude for each cross-line to illustrate the changes in one-way travel time in different seasons.

The results of the travel time analysis show that the change in thickness between each intersecting in-line is different over the course of a seasonal cycle. In Figures 4.1, 4.2, 4.3, and 4.4, a third order polynomial curve is fitted in each figure to show the expected cyclical nature of seasonal variation. Travel time (ns) differences between the surface horizons at each intersection is relatively large during the late southern fall and winter compared to the travel time differences during the southern summer on each cross-line. All cross-lines (Figures 4.1 – 4)

display good fit to all the data points. The trend of the travel time difference increases during fall and reaches its maximum around winter, except cross-line 5723 where the maximum is between late fall and early winter. The trend then starts to decrease during spring and reaches its minimum during summer. Although the fitted curve treats all data points equally, topographic variability between points will introduce additional changes.

After travel time at each intersection was converted to thickness (m) between both surface horizons with a dielectric constant of CO₂ frost ($\epsilon_r = 2.12$) (Pettinelli et al., 2003), the same seasonal variation trend is observed in figures 4.5, 4.6, 4.7, and 4.8. A third order polynomial is again applied to each figure to show that thickness at each intersection is larger during the southern fall and winter than those during the southern summer. The trend of thickness difference increases during fall and reaches its maximum around winter, except cross-line 5723 where the maximum is between late fall and early winter. The trend then starts to decrease during spring and reaches its minimum during summer. As presented in Chapter 3.4, figures 4.9, 4.10, 4.11, and 4.12 summarize the changes in CO₂ frost thickness through different seasons within each in-line pair along each cross-line, where both in-lines in each pair are close to each other in space for direct comparison. For example, in Figure 4.9, the changes in CO₂ frost thickness are 7.62 m from mid summer (in-line 5570) to mid winter (in-line

10066), 7.93 m from early summer (in-line 4436) to late fall (in-line 8787), and 12.1 m from mid summer (in-line 5214) to mid fall (in-line 7851).

Horizon picking error analysis is performed on two out of three in-line pairs along cross-line 4444 by conducting the same travel time analysis on two different subsurface reflections. The small number of continuous and high signal-to-noise reflections on few cross-lines and in-lines limits the data available for error analysis on all profiles used in this study. The same two subsurface reflections on cross-lines 5723, 5789, and 11920 are not picked due to the data quality. The subsurface reflection that is selected as a reference datum for the travel time analysis presented in Chapter 3.4 is the most coherent reflection in the data. Picking reflections of lower quality would introduce greater uncertainty.

The results of the change in CO₂ frost thickness from a less continuous and lower signal-to-noise reflection along cross-line 4444 are 6.80 m from mid summer (in-line 5570) to mid winter (in-line 10066) and 6.79 m from early summer (in-line 4436) to late fall (in-line 8787). As shown in Figure 4.9, the corresponding thicknesses are 7.62 and 7.93 m from the best subsurface reflection. The results from the continuous and higher signal-to-noise reflection should be more reliable than less continuous and lower signal-to-noise reflections.

The trend in each cross-line is in agreement and the seasonality of the changes is consistent with other studies mentioned in Chapters 1.3 and 1.4.

Studies by Smith et al. (2001), Feldman et al. (2003), and Kelly et al. (2006) stated that CO₂ frost starts accumulating as the amount of sunlight decreases after the autumnal equinox at the southern hemisphere ($L_s = 0$). The accumulation is formed first at high latitude and extends toward the equator as winter arrives. The thickness of the CO₂ frost layer is the greatest during late fall and winter. During early spring when the South Pole starts to receive more sunlight, the thickness of the accumulation decreases as the temperature rises above the CO₂ condensation point and CO₂ sublimates back into the atmosphere. The CO₂ frost is then limited to areas of high latitude and elevation during southern summer.

The seasonal change in one-way travel time and CO₂ frost thickness between winter and summer is observed in this analysis (Figures 4.1–8) and agrees with other studies; however, the magnitude of change on each cross-line is larger than what other studies have shown, up to 14.4m in cross-line 11920 between in-lines 5570 and 11920) (Figure 4.12). One study by Smith et al. (2001) stated that the greatest elevation change was only 0.9 ± 0.3 m at a latitude above 80° in the south hemisphere by using Mars Orbiter Laser Altimeter (MOLA). Another study by Aharonson et al. (2004) suggested that the elevation change was no more than 2.5 m in the south pole, using MOLA as well.

Variability in estimating CO₂ thickness can be introduced by uncertainty in the dielectric constant of the medium used to estimate the thickness within each

in-line pair. Travel time and radar signal propagation velocity within each in-line pair are used to calculate the vertical change (m). While the difference in travel time within each in-line pair is measured directly from the data misalignments, the radar signal propagation velocity varies as a function of medium dielectric constant as shown in the following relationship

$$v = \frac{c}{\sqrt{\epsilon_r}}$$

where v is the radar signal propagation velocity, c is the speed of light ($0.3 \frac{m}{ns}$), and ϵ_r is the dielectric constant. Dielectric constant varies depending on the materials the radar signal travels through. The radar signal propagation velocity has an inverse relationship to the dielectric constant (Figure 4.13) and it changes dramatically between the dielectric constants of 1 and 5, which could significantly affect the conversion to thickness. Therefore, different dielectric constants from 1 – 10 are used to determine thicknesses within each in-line pair on every cross-line to examine the effect of different dielectric constants to thickness.

Each of the Figures 4.14, 4.15, 4.16, and 4.17 represent the change in thickness between both in-lines in each pair with different dielectric constants on each cross-line 5789, 5723, 4444, and 11920, respectively. The blue curve represents the change in thicknesses between in-lines 5570 and 10066 with different dielectric constants. The red curve represents the change in thickness

between in-lines 4436 and 8787. The green curve represents the change in thickness between in-lines 5214 and 7851. The horizontal axis represents the dielectric constant from 1 to 5 and the vertical axis represents the thickness. These figures illustrate an exponential decrease of the thickness as dielectric constant increases.

The results in Figures 4.1 – 8 demonstrate that using a dielectric constant of pure CO₂ frost ($\epsilon_r = 2.12$) does not provide comparable estimates to other studies about the change in surface elevation at each intersection. Figures 4.14 – 17 prove that it is not likely to achieve the measurements made by other studies (below or around 2.5m).

This suggests that the south polar cap does not only consist of pure CO₂. It has to be mixed with the iron-rich Martian soil (Pettinelli et al., 2005), which is carried by wind and is deposited on top of the ice. Having iron-rich material on the Martian surface increases the bulk medium dielectric constant, but it is still not sufficient to obtain the thickness as small as reported in other studies.

According to the Lichtenecker's formula, which is a mixing formula for calculating the dielectric constant of materials (Olhoeft, 1989), the dielectric constant increases to 2.77 when 85% of pure CO₂ frost is mixed with 10% of pure hematite and 5% of pure water ice in volume

$$\varepsilon_m = \varepsilon_1^{v_1} \varepsilon_2^{v_2} \dots \varepsilon_n^{v_n}$$

$$\varepsilon_m = \varepsilon_1^{v_1} \varepsilon_2^{v_2} \varepsilon_3^{v_3}$$

where ε_m is the dielectric constant after mixing, V_1 is the volume fraction of the CO₂ frost, ε_1 is the dielectric constant for CO₂, V_2 is the volume fraction of pure hematite, ε_2 is the dielectric constant of pure hematite, and V_3 is the volume fraction of pure water ice, ε_3 is the dielectric constant of pure water ice.

$$\varepsilon_m = 2.12^{0.85} * 25^{0.1} * 3.29^{0.05} = 2.77$$

The thickness between both in-lines in each pair decreases in general along each cross-line with the increased dielectric constant from 2.12 (CO₂) to 2.77 (mixed material) (Tables 4.1, 4.2, 4.3, and 4.4). The average thicknesses (Table 4.5) with the dielectric constant of 2.77 ranged from 6.80m to 8.38m are still larger than what other studies reported; however, these results are reasonable because each study have a different area of interest. The results of this study reflect the thickness change between different seasons at the area of this study and the results with both dielectric constants of 2.12 and 2.77 are still somewhat close to other studies.

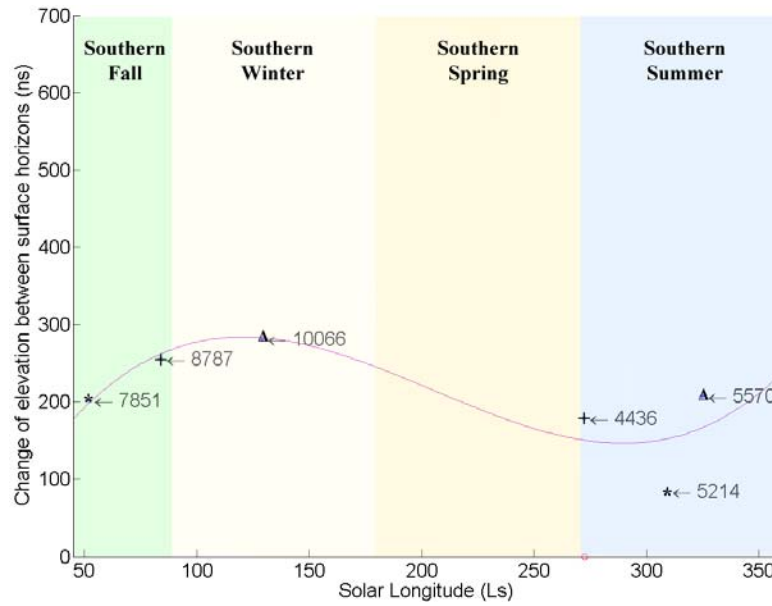


Figure 4.1 Difference in one-way travel time (ns) between the surface horizon of each of the six in-lines and the surface horizon of the cross-line 4444 at every intersection. The red circle on the x-axis corresponds to the season when cross-line 4444 was acquired.

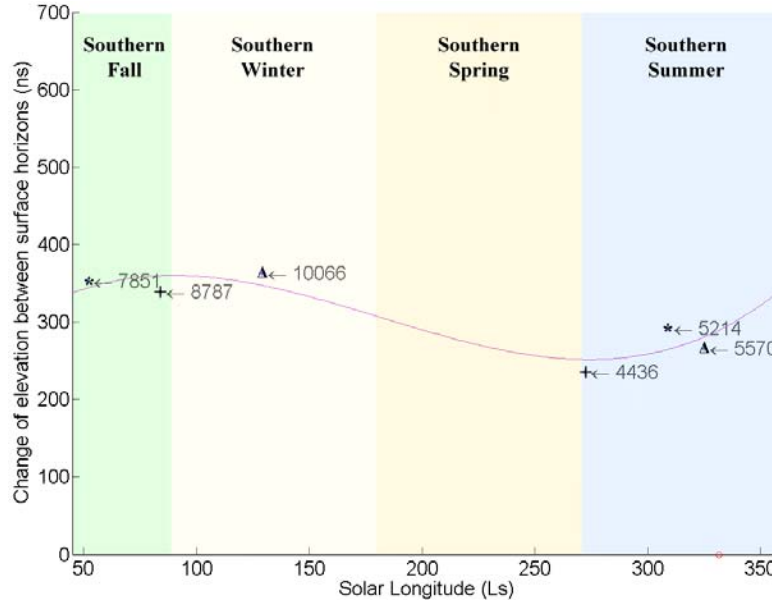


Figure 4.2 Difference in one-way travel time (ns) between the surface horizon of each of the six in-lines and the surface horizon of the cross-line 5723 at every intersection. The red circle on the x-axis corresponds to the season when cross-line 5723 was acquired.

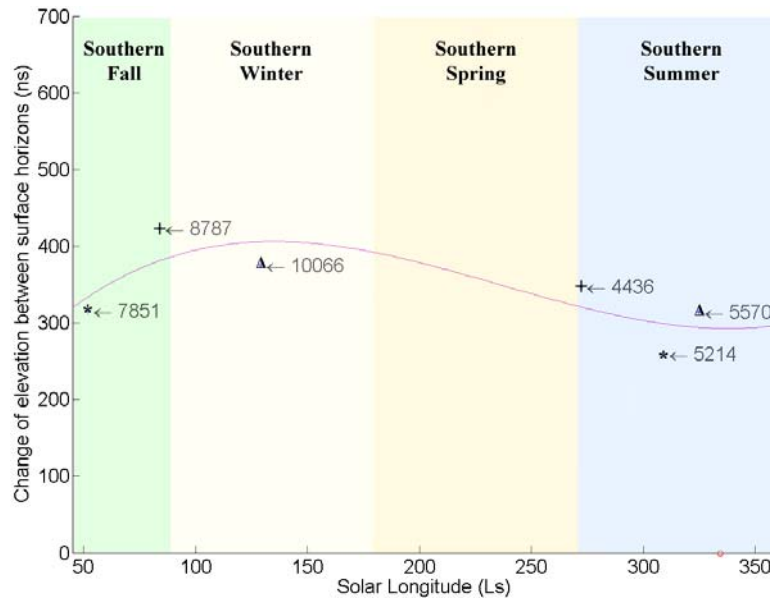


Figure 4.3 Difference in one-way travel time (ns) between the surface horizon of each of the six in-lines and the surface horizon of the cross-line 5789 at every intersection. The red circle on the x-axis corresponds to the season when cross-line 5789 was acquired.

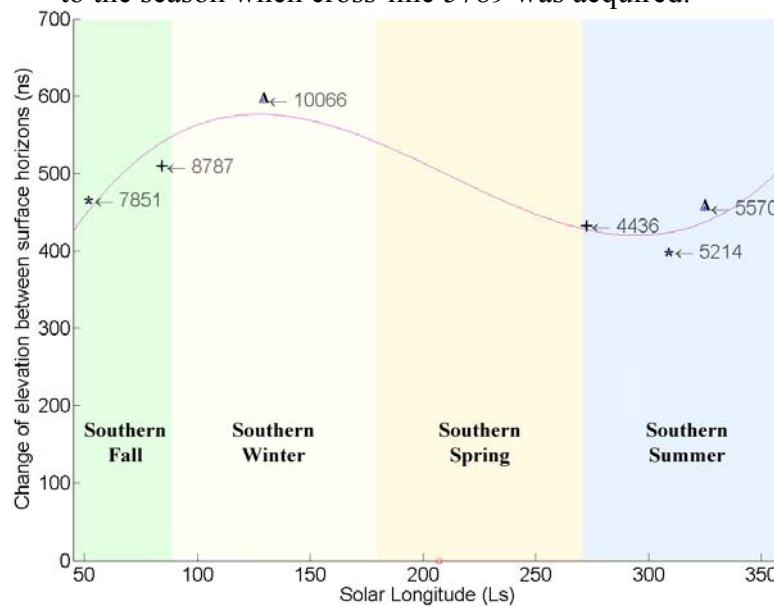


Figure 4.4 Difference in one-way travel time (ns) between the surface horizon of each of the six in-lines and the surface horizon of the cross-line 11920 at every intersection. The red circle on the x-axis corresponds to the season when cross-line 11920 was acquired.

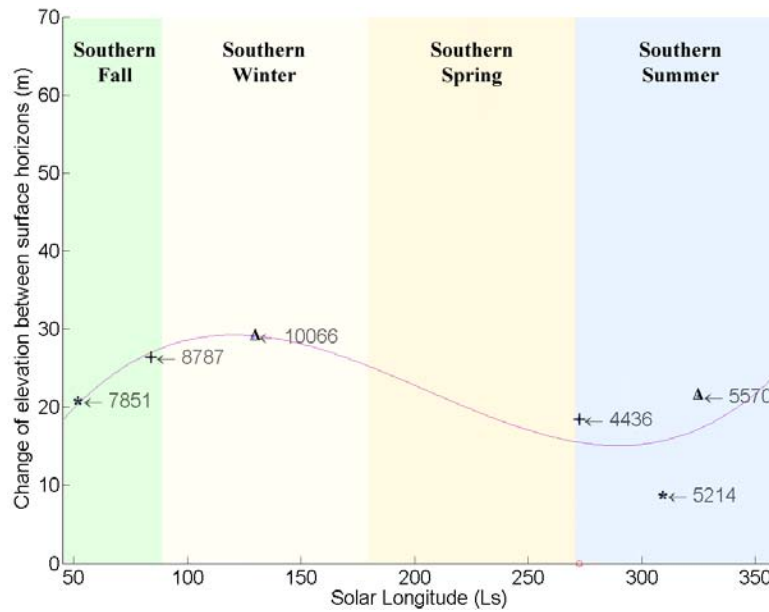


Figure 4.5 Thickness (m) between the surface horizon of each of the six in-lines and the surface horizon of the cross-line 4444 at every intersection. The red circle on the x-axis corresponds to the season when cross-line 4444 was acquired.

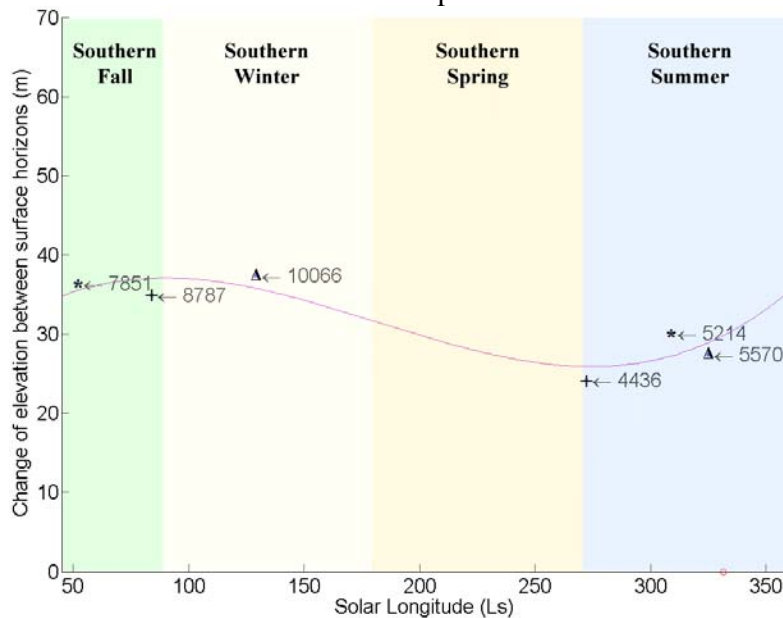


Figure 4.6 Thickness (m) between the surface horizon of each of the six in-lines and the surface horizon of the cross-line (Orbital track 5723) at every intersection. The red circle on the x-axis corresponds to the season when cross-line 5723 was acquired.

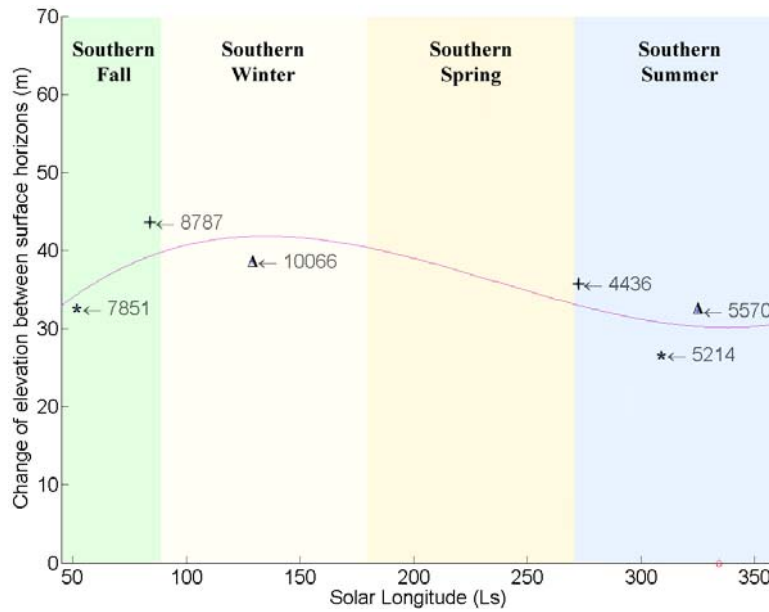


Figure 4.7 Thickness (m) between the surface horizon of each of the six in-lines and the surface horizon of the cross-line (Orbital track 5789) at every intersection. The red circle on the x-axis corresponds to the season when cross-line 5789 was acquired.

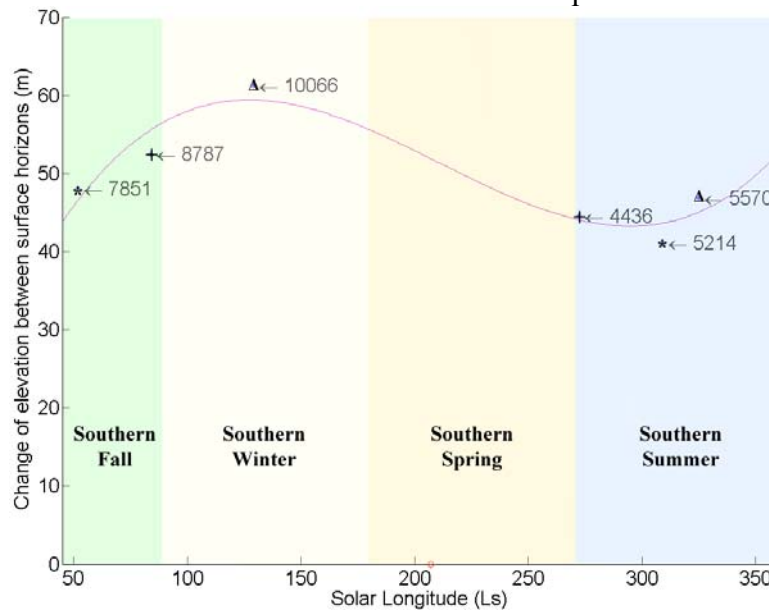


Figure 4.8 Thickness (m) between the surface horizon of each of the six in-lines and the surface horizon of the cross-line (Orbital track 11920) at every intersection. The red circle on the x-axis corresponds to the season when cross-line 11920 was acquired.

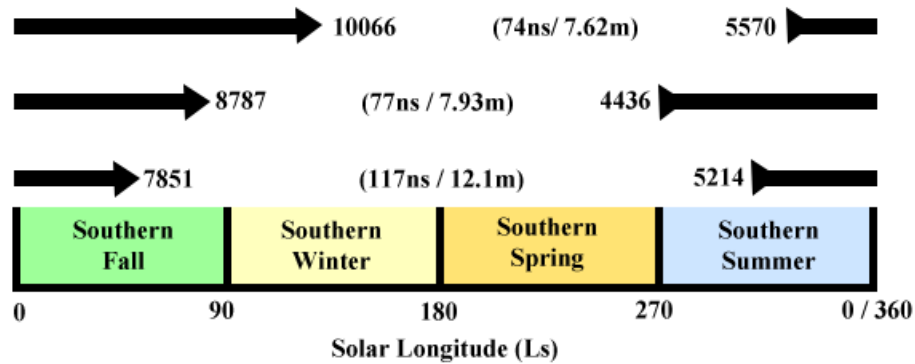


Figure 4.9 Three arrows represent three different in-line pairs that show the one-way travel time taken and change in thickness measured between one in-line (i.e. 10066) and another in-line (i.e. 5570) through different seasons along cross-line 4444

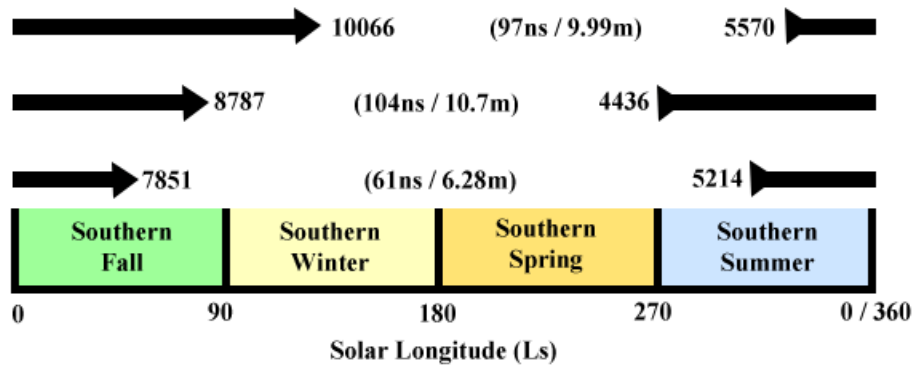


Figure 4.10 Three arrows represent three different in-line pairs that show the one-way travel time taken and change in thickness measured between one in-line (i.e. 10066) and another in-line (i.e. 5570) through different seasons along cross-line 5723

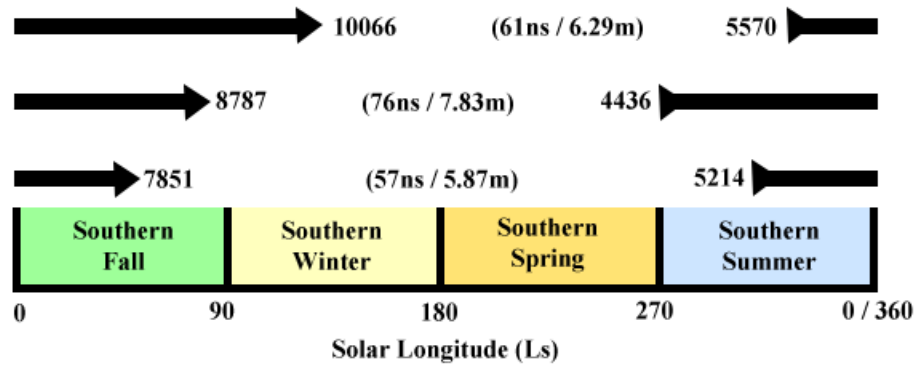


Figure 4.11 Three arrows represent three different in-line pairs that show the one-way travel time taken and change in thickness measured between one in-line (i.e. 10066) and another in-line (i.e. 5570) through different seasons along cross-line 5789

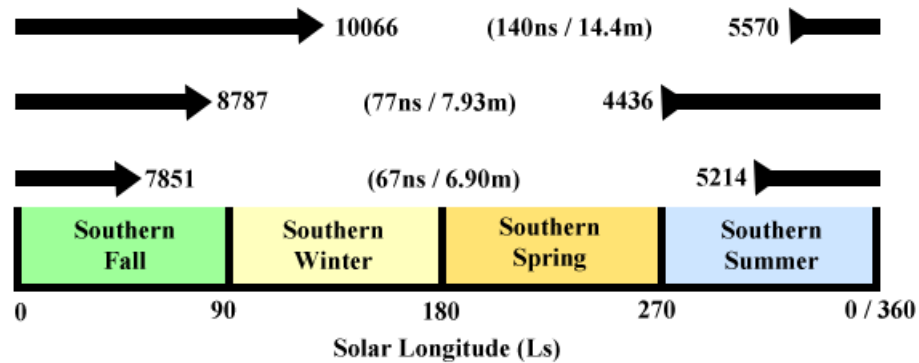


Figure 4.12 Three arrows represent three different in-line pairs that show the one-way travel time taken and change in thickness measured between one in-line (i.e. 10066) and another in-line (i.e. 5570) through different seasons along cross-line 11920

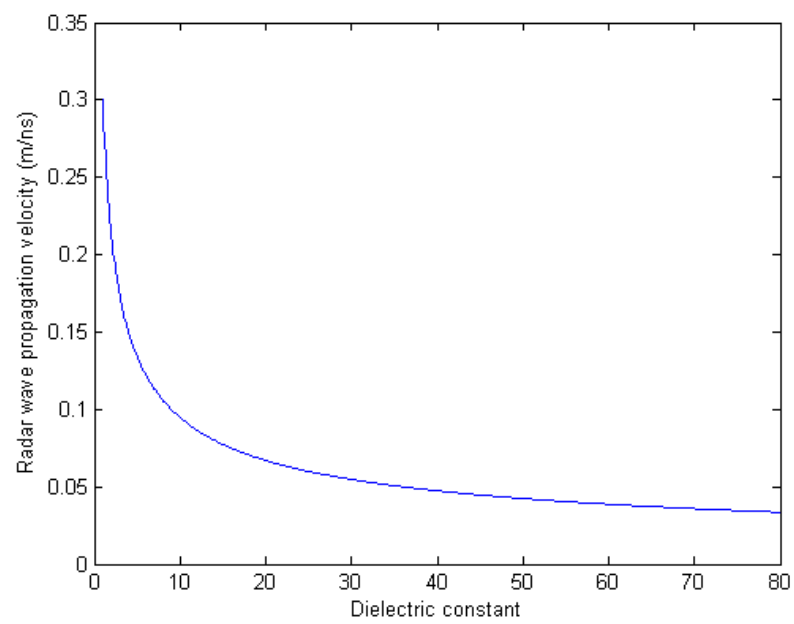


Figure 4.13 Radar wave propagation velocity with different dielectric constants

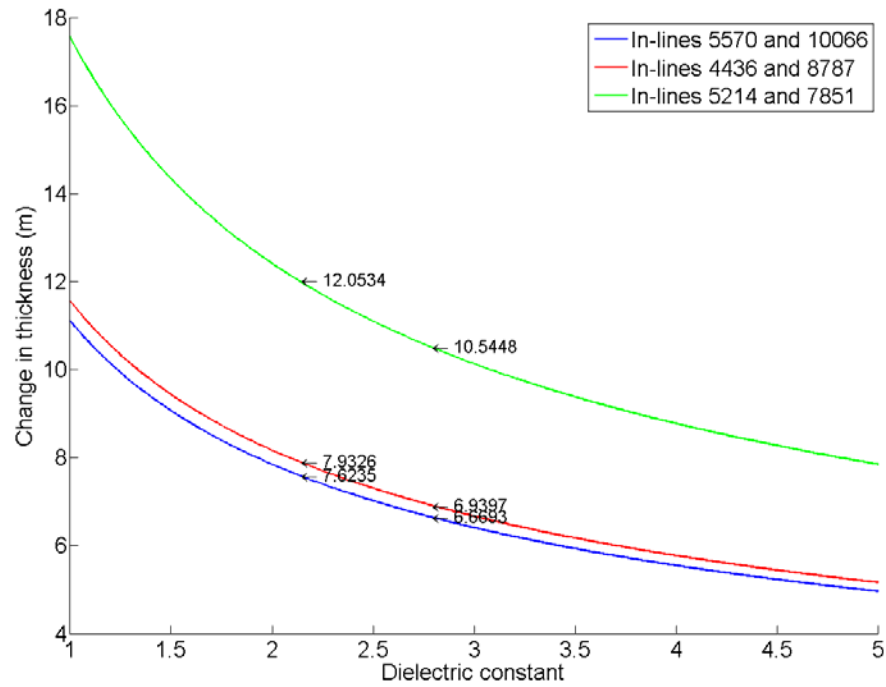


Figure 4.14 Thickness vs. dielectric constant along cross-line 4444. Each arrow shows the thickness for each in-line pair with $\epsilon_r = 2.12$ and 2.77 .

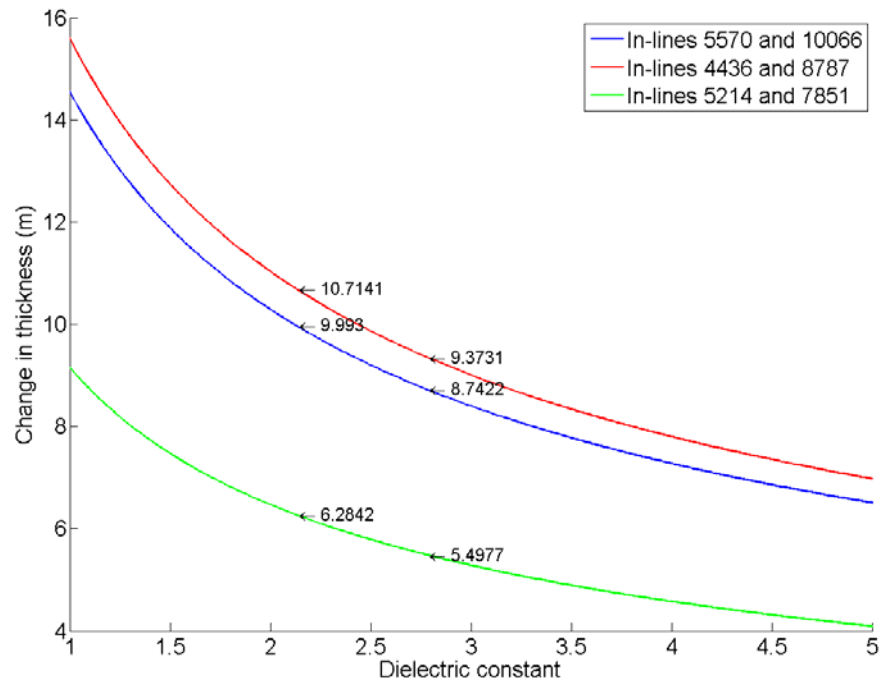


Figure 4.15 Thickness vs. dielectric constant along cross-line 5723. Each arrow shows the thickness for each in-line pair with $\epsilon_r = 2.12$ and 2.77 .

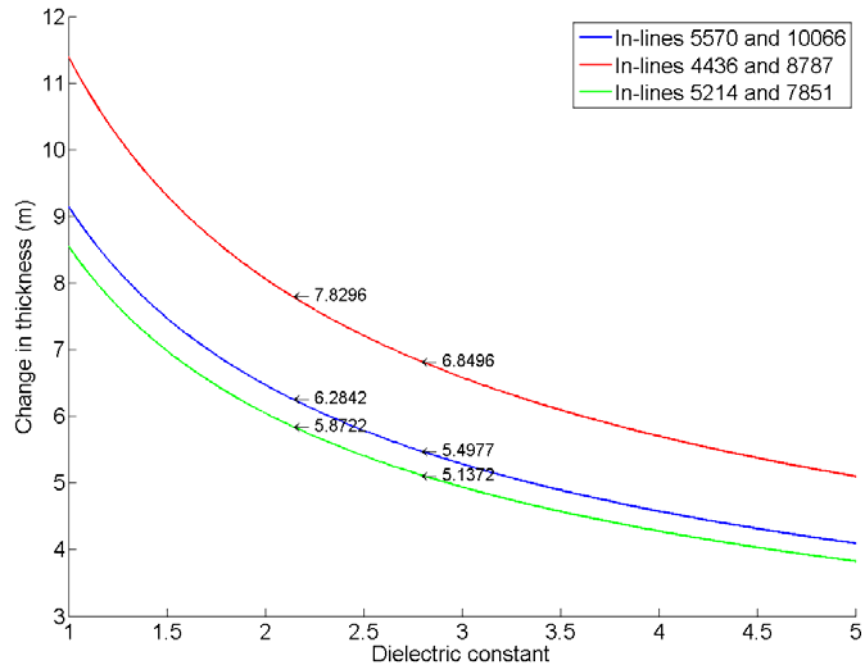


Figure 4.16 Thickness vs. dielectric constant along cross-line 5789. Each arrow shows the thickness for each in-line pair with $\epsilon_r = 2.12$ and 2.77 .

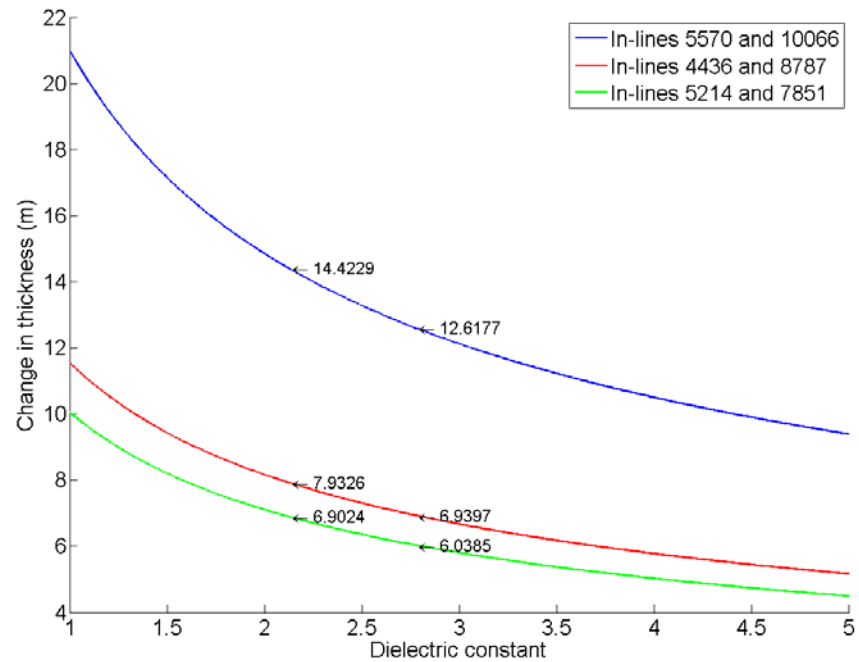


Figure 4.17 Thickness vs. dielectric constant along cross-line 11920. Each arrow shows the thickness for each in-line pair with $\epsilon_r = 2.12$ and 2.77 .

	Thickness (m) ($\epsilon_r = 2.12$)	Thickness (m) ($\epsilon_r = 2.77$)	Difference (m)
5570 and 10066	7.62	6.67	0.95
4436 and 8787	7.93	6.94	0.99
5214 and 7851	12.05	10.54	1.51

Table 4.1 Thicknesses with dielectric constants of 2.12 and 2.77 and their differences on cross-line 4444

	Thickness (m) ($\epsilon_r = 2.12$)	Thickness (m) ($\epsilon_r = 2.77$)	Difference (m)
5570 and 10066	9.99	8.74	1.25
4436 and 8787	10.71	9.37	1.34
5214 and 7851	6.28	5.49	0.79

Table 4.2 Thicknesses with dielectric constants of 2.12 and 2.77 and their differences on cross-line 5723

	Thickness (m) ($\epsilon_r = 2.12$)	Thickness (m) ($\epsilon_r = 2.77$)	Difference (m)
5570 and 10066	6.28	5.50	0.78
4436 and 8787	7.83	6.85	0.98
5214 and 7851	5.87	5.14	0.73

Table 4.3 Thicknesses with dielectric constants of 2.12 and 2.77 and their differences on cross-line 5789

	Thickness (m) ($\epsilon_r = 2.12$)	Thickness (m) ($\epsilon_r = 2.77$)	Difference (m)
5570 and 10066	14.42	12.62	1.8
4436 and 8787	7.93	6.94	0.99
5214 and 7851	6.90	6.04	0.86

Table 4.4 Thicknesses with dielectric constants of 2.12 and 2.77 and their differences on cross-line 11920

	Average Thickness (m) ($\epsilon_r = 2.12$)	Average Thickness (m) ($\epsilon_r = 2.77$)	Average Difference (m)
5570 and 10066	9.58	8.38	1.20
4436 and 8787	8.60	7.53	1.07
5214 and 7851	7.78	6.80	0.98

Table 4.5 Average thicknesses with dielectric constants of 2.12 and 2.77 and their average differences along all the cross-lines

4.2 Amplitude analysis

Unlike the results from the travel time analysis, the results from the amplitude analysis shows almost no trend in CO₂ thickness changes over the course of a season cycle. The difference in both amplitude ratios between a cross-line and an in-line at each intersection is scattered and does not follow any type of pattern (Figures 4.14, 4.15, 4.16, and 4.17).

An observation is made on the difference in amplitude ratios that is more spread out during summer in Figures 4.15 and 4.16 than those during the southern fall and winter. One possible explanation is that the water ice with an unknown amount of Martians dust collected over years is exposed on the surface during summer, which provides a different reflectivity to the SHARAD signals. The reflected amplitude readings could be varied based on the reflectivity at those locations. On the opposite, the Martian surface is more uniform with a layer of CO₂ frost condensed on the surface during winter and provides a more constant reflectivity over a large area for the SHARAD signals. Unfortunately, this could vary greatly depending on the location and time the radar measurements are made.

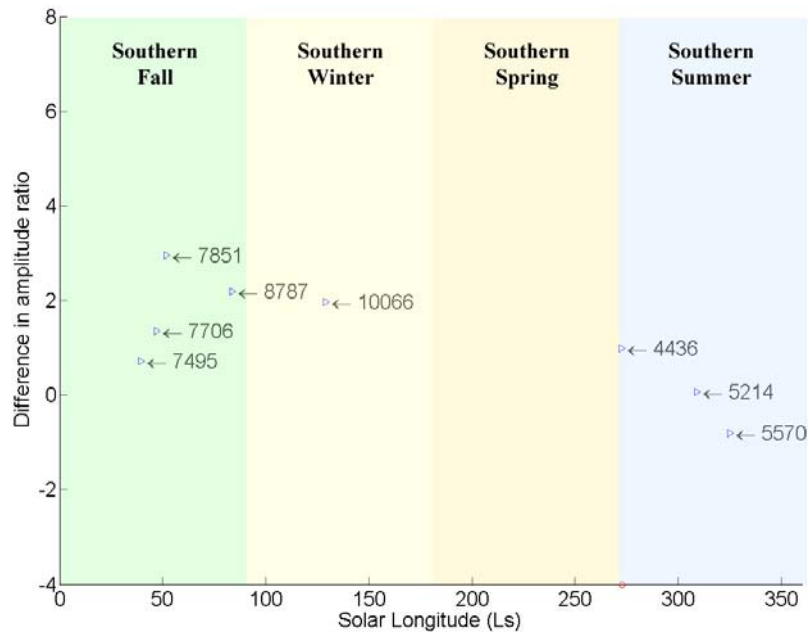


Figure 4.18 Difference in amplitude ratios at each intersection between each of eight in-lines and cross-line 4444. The red circle on the x-axis corresponds to the season when cross-line 4444 was acquired.

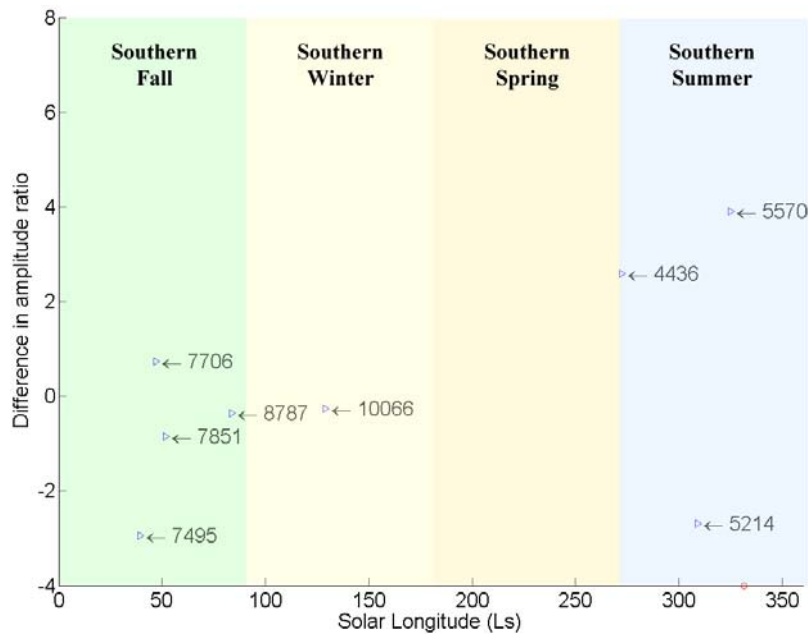


Figure 4.19 Difference in amplitude ratios at each intersection between each of eight in-lines and cross-line 5723. The red circle on the x-axis corresponds to the season when cross-line 5723 was acquired.

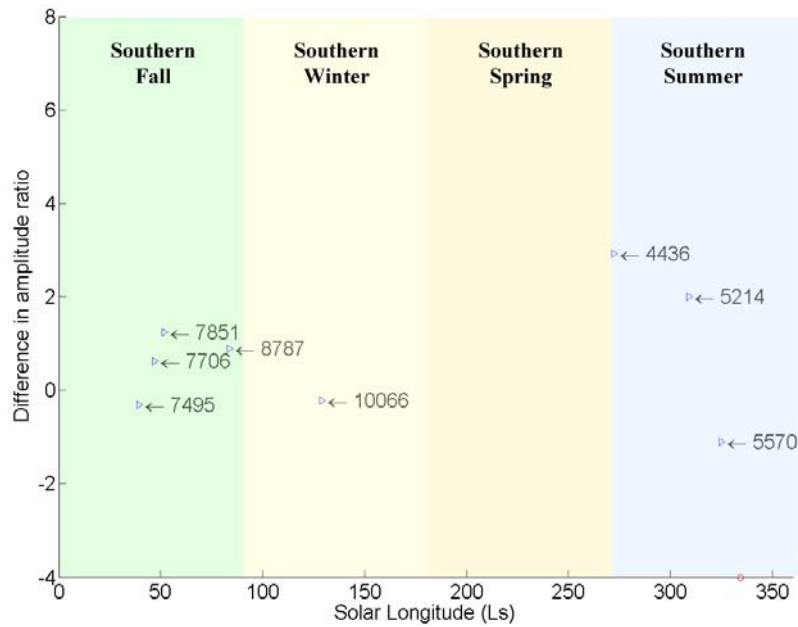


Figure 4.20 Difference in amplitude ratios at each intersection between each of eight in-lines and cross-line 5789. The red circle on the x-axis corresponds to the season when cross-line 5789 was acquired.

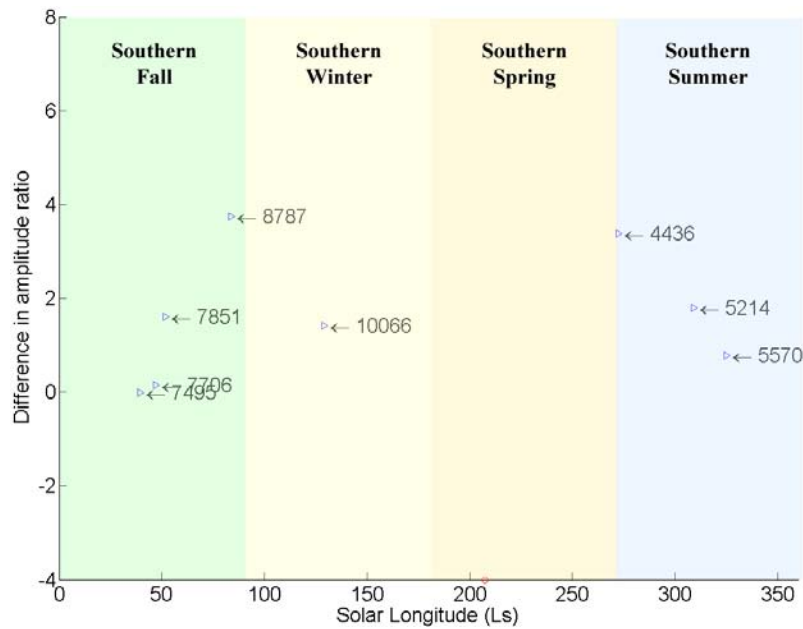


Figure 4.21 Difference in amplitude ratios at each intersection between each of eight in-lines and cross-line 11920. The red circle on the x-axis corresponds to the season when cross-line 11920 was acquired.

Chapter 5: Conclusions and Recommendations

Using SHARAD proves to be an effective method for imaging the Martian surface and subsurface at the field area in the south polar region. Data returned from SHARAD is used for the first time to analyze whether SHARAD signals are influenced by seasonal variability on the surface since each set of the SHARAD data was collected during a different season.

A method has been developed to visualize and interpret for the SHARAD data in Kingdom Suite by first running a script in Interactive Data Language to extract SHARAD data and then MATLAB to convert SHARAD data into the SEG-Y format. After the data is displayed in Kingdom Suite for interpretation, misalignment is observed between surface reflections of every two intersecting orbital tracks. Travel time analysis is conducted to estimate the difference of these misalignments in terms of their travel time. The difference in travel time at each intersection is converted from time to thickness and plotted against different seasons.

The results of the travel time analysis show that the average CO₂ frost thickness ranges from 6.80m to 8.38m with a dielectric constant of 2.77 and from 7.78m to 9.58m with a dielectric constant of 2.12. The CO₂ thickness reaches its maximum during winter and minimum during summer likely because of the CO₂

frost accumulation and retreat, respectively. This observation agrees with other studies. However, the magnitude of change in CO₂ frost thickness estimated in this study is somewhat greater than values reported in other studies (Aharonson et al., 2004; Bibring et al., 2004; Smith et al., 2001). It is because each study has a different location and the results of this study reflect the CO₂ frost thickness difference at the location of this study.

Amplitude analysis is not able to show any type of pattern caused by seasonal variations on the Martian surface consistently through all four cross-lines. The difference in amplitude ratios at each intersection between an in-line and a cross-line are scattered without any interpretable trend. Analyzing the travel time of the SHARAD signals proves to be a more effective approach for this investigation.

Tracking the change in surface elevation caused by seasonal variation may provide a way to estimate the amount of water ice and CO₂ frost accumulated on the surface in between different seasons. The approach of this study highlights the dynamic of the south polar ice cap through different seasons. The travel time analysis can be applied at the north polar ice cap and other locations at the south polar ice cap for result comparison. In addition, study at the polar regions has always been an important goal for Mars exploration to search for useable water reservoirs for future manned missions.

A rover-based GPR (Grant et al., 2003) will help for acquiring high spatial and vertical resolution near-surface data. More detailed images of sedimentary or ice layers in the near-surface can be revealed for geologic and hydrologic investigations. The results presented in this study show how important GPR imaging is for understanding the current condition on Mars by monitoring water ice and CO₂ accumulation at the south polar regions. GPR imaging also offers a way to understand the past by imaging subsurface layering.

Most importantly, this investigation will extend the knowledge and evaluate the utility of the radar sounding method and signal processing technique for future radar subsurface explorations.

References

- Aharonson, O., Zuber, M. T., Smith, D. E., Neumann, G. A., Feldman, W. C., and Prettyman, T. H. (2004), Depth, distribution, and density of CO₂ deposition on Mars, *Journal of Geophysical Research*, v. 109, E05004, doi: 10.1029/2003JE002223.
- Alberti, G., Dinardo, S., Mattei, E., Papa, C., and Santovito, M. R. (2007), SHARAD radar signal processing technique, abstract presented at 4th International Workshop on Advanced Ground Penetrating Radar, Naples, Italy, June 27-29.
- Bibring, J.-P., Langevin, Y., Poulet, F., Gendrin, A., Gondet, B., Berthe, M., Soufflot, A., Drossart, P., Combes, M., Bellucci, G., Moroz, V., Mangold, N., Schmitt, B., and team, t. O. (2004), Perennial water ice identified in the south polar cap of Mars, *Nature*, v. 428, 627-630, doi: 10.1038/NATURE02474.
- Boynton, W. V., Feldman, W. C., Squyres, S. W., Prettyman, T. H., Bruckner, J., Evans, L. G., Reedy, R. C., Starr, R., Arnold, J. R., Drake, D. M., Englert, P. A. J., Metzger, A. E., Mitrofanov, I., Trombka, J. I., d'Uston, C., Wanke, H., Gasnault, O., Hamara, D. K., Janes, D. M., Marcialis, R. L., Maurice, S., Mikheeva, I., Taylor, G. L., Tokar, R., and Shinohara, C. (2002), Distribution of hydrogen in the near surface of Mars: Evidence for subsurface ice deposits, *Science*, v. 297, 81-85, doi: 10.1126/SCIENCE.1073722.
- Christie, M., Tsoflis, G. P., Stockli, D. F., and Black, R. (2009), Assessing fault displacement and off-fault deformation in an extensional tectonic setting using 3-D ground-penetrating radar imaging, *Journal of Applied Geophysics*, v. 68, 9-16, doi: 10.1016/J.JAPPGEO.2008.10.013.
- Farrell, W. M., Clifford, S. M., Milkovich, S. M., Plaut, J. J., Leuschen, C. J., Picardi, G., Gurnett, D. A., Watters, T. R., Safaeinili, A., Ivanov, A. B., Phillips, R. J., Stofan, E. R., Heggy, E., Cummer, S. A., and Espley, J. R. (2008), MARSIS subsurface radar investigation of the south polar reentrant Chasma Australe, *Journal of Geophysical Research*, v. 113, E04002, doi: 10.1029/2007JE002974.

- Feldman, W. C., Prettyman, T. H., Boynton, W. V., Murphy, J. R., Squyres, S., Karunatillake, S., Maurice, S., Tokar, R. L., McKinney, G. W., Hamara, D. K., Kelly, N., and Kerry, K. (2003), CO₂ frost cap thickness on Mars during northern winter and spring, *Journal of Geophysical Research*, v. 108, E9, 5103, doi: 10.1029/2003JE002101.
- Flamini, E., Fois, F., Calabrese, D., Bombaci, O., Catallo, C., Croce, A., Croci, R., Guelfi, M., Zampolini, E., Picardi, G., Seu, R., Mecozzi, R., Biccari, D., Cartacci, M., Cicchetti, A., Masdea, A., Alberti, G., Maffei, S., and Papa, C. (2007), Sounding Mars with SHARAD and MARSIS, abstract presented at 4th International Workshop on Advanced Ground Penetrating Radar, Naples, Italy, June 27-29.
- Gogineni, S., Tammana, D., Braaten, D., Leuschen, C., Akins, T., Legarsky, J., Kanagaratnam, P., Stiles, J., Allen, C., and Jezek, K. (2001), Coherent radar ice thickness measurements over the Greenland ice sheet, *Journal of Geophysical Research*, v. 106, D24, 33,761-733,772.
- Grant, J. A., Schutz, A. E., and Campbell, B. A. (2003), Ground-penetrating radar as a tool for probing the shallow subsurface of Mars, *Journal of Geophysical Research*, v. 108, E4, 8024, doi: 10.1029/2002JE001856.
- Hansen, T. M. (2010), SegyMAT, [Software]. Available from <http://segymat.sourceforge.net>.
- Kelly, N. J., Boynton, W. V., Kerry, K., Hamara, D., Janes, D., Reedy, R. C., Kim, K. J., and Haberle, R. M. (2006), Seasonal polar carbon dioxide frost on Mars: CO₂ mass and columnar thickness distribution, *Journal of Geophysical Research*, v. 111, E03S07, doi: 10.1029/2006JE002678.
- Kieffer, H. H. (1979), Mars south pole spring and summer temperatures: A residual CO₂ frost, *Journal of Geophysical Research*, v. 84, B14, 8236-8288.
- National Aeronautics and Space Administration, Program and mission historical Log, <http://mars.jpl.nasa.gov/programmissions/missions/log/>, date accessed:12-06-2010, date cited: 12-06-2010.
- National Aeronautics and Space Administration, European Space Agency, Jet Propulsion Laboratory, University of Rome, and Washington University in St. Louis (2008), Two radar sounders examine South Polar Layered Deposits on Mars,

http://www.nasa.gov/mission_pages/mars/images/marsis-caption-20080417.html, date accessed:12-06-2010, date cited: 12-06-2010.

National Aeronautics and Space Administration, and Jet Propulsion Laboratory (2005), The Mars Reconnaissance Orbiter using radar (side view), http://www.nasa.gov/mission_pages/MRO/multimedia/sharad-side.html, date accessed:11-29-2010, date cited: 11-29-2010.

Nunes, D. C., and Phillips, R. J. (2006), Radar subsurface mapping of the polar layered deposits on Mars, *Journal of Geophysical Research*, v. 111, E06S21, doi: 10.1029/2005JE002609.

Nye, J. F., Durham, W. B., Schenk, P. M., and Moore, J. M. (2000), The instability of a south polar cap on Mars composed of carbon dioxide, *Icarus*, v. 144, 449-455, doi: 10.1006/ICAR.1999.6306.

Olhoeft, G. R. (1989), Electrical properties of rocks, in *Physical Property of Rocks and Minerals*, Taylor and Francis, Philadelphia, Pa.

Pettinelli, E., Vannaroni, G., Cereti, A., Paolucci, F., Della Monica, G., Storini, M., and Bella, F. (2003), Frequency and time domain permittivity measurements on solid CO₂ and solid CO₂-soil mixtures as Martian soil simulants, *Journal of Geophysical Research*, v. 108, E4, 8029, doi: 10.1029/2002JE001869.

Pettinelli, E., Vannaroni, G., Cereti, A., Pisani, A. R., Paolucci, F., Del Vento, D., Dolfi, D., Riccioli, S., and Bella, F. (2005), Laboratory investigations into the electromagnetic properties of magnetite/silica mixtures as Martian soil simulants, *Journal of Geophysical Research*, v. 110, E04013, doi: 10.1029/2004JE002375.

Phillips, R. J., Davis, B. J., Byrne, S., Campbell, B. A., Carter, L. M., Haberle, R. M., Holt, J. W., Kahre, M. A., Nunes, D. C., Plaut, J. J., Putzig, N. E., Smith, I. B., Smrekar, S. E., Tanaka, K. L., and Titus, T. N. (2010), SHARAD finds voluminous CO₂ ice sequestered in the Martian South Polar Layered Deposits, abstract P34A-01 presented at 2010 Fall Meeting, American Geophysical Union, San Francisco, California, USA, December 13-17.

Phillips, R. J., Zuber, M. T., Smrekar, S. E., Mellon, M. T., Head III, J. W., Tanaka, K. L., Putzig, N. E., Milkovich, S. M., Campbell, B. A., Plaut, J. J., Safaeinili, A., Seu, R., Biccari, D., Carter, L. M., Picardi, G., Orosei, R.,

- Mohit, P. S., Heggy, E., Zurek, R. W., Egan, A. F., Giacomoni, E., Russo, F., Cutigni, M., Pettinelli, E., Holt, J. W., Leuschen, C., and Marinangeli, L. (2008), Mars north polar deposits: stratigraphy, age, and geodynamical response, *Science*, v. 320, 1182-1185, doi: 10.1126/science.1157546.
- Picardi, G., Plaut, J. J., Biccari, D., Bombaci, O., Cartacci, M., Cicchetti, A., Clifford, S. M., Edenhofer, P., Farrell, W. M., Federico, C., Frigeri, A., Gurnett, D. A., Hagfors, T., Heggy, E., Herique, A., Huff, R. L., Ivanov, A. B., Johnson, W. T. K., Jordan, R. L., Kirchner, D. L., Kofman, W., Leuschen, C., Nielsen, E., Orosei, R., Pettinelli, E., Phillips, R. J., Plettemeier, D., Safaeinili, A., Seu, R., Stofan, E. R., Vannaroni, G., Watters, T. R., and Zampolini, E. (2005), Radar soundings of the subsurface of Mars, *Science*, v. 310, 1925-1928, doi: 10.1126/SCIENCE.1122165.
- Plaut, J. J., Picardi, G., Safaeinili, A., Ivanov, A. B., Milkovich, S. M., Cicchetti, A., Kofman, W., Mouginot, J., Farrell, W. M., Phillips, R. J., Clifford, S. M., Frigeri, A., Orosei, R., Federico, C., Williams, I. P., Gurnett, D. A., Nielsen, E., Hagfors, T., Heggy, E., Stofan, E. R., Plettemeier, D., Watters, T. R., Leuschen, C., and Edenhofer, P. (2007), Subsurface radar sounding of the south polar layered deposits of Mars, *Science*, v. 316, 92-95, doi: 10.1126/SCIENCE.1139672.
- Putzig, N. E., Phillips, R. J., Campbell, B. A., Holt, J. W., Plaut, J. J., Carter, L. M., Egan, A. F., Bernardini, F., Safaeinili, A., and Seu, R. (2009), Subsurface structure of Planum Boreum from Mars Reconnaissance Orbiter Shallow Radar soundings, *Icarus*, v. 204, 443-457, doi: 10.1016/J.ICARUS.2009.07.034.
- Safaeinili, A., Kofman, W., Nouvel, J.-F., Herique, A., and Jordan, R. L. (2003), Impact of Mars ionosphere on orbital radar sounder operation and data processing, *Planetary and Space Science*, v. 51, 505-515, doi: 10.1016/S0032-0633(03)00048-5.
- Seu, R., Phillips, R. J., Albertim G., Biccari, D., Bonaventura, F., Bortone, M., Calabrese, D., Campbell, B. A., Cartacci, M., Carter, L. M., Catallo, C., Croce, A., Croci, R., Cutigni, M., Di Placido, A., Dinardo, S., Federico, C., Flamini, E., Fois, F., Frigeri, A., Fuga, O., Giacomoni, E., Gim, Y., Guelfi, M., Holt, J. W., Kofman, W., Leuschen, C. J., Marinangeli, L., Marras, P., Masdea, A., Mattei, S., Mecozzi, R., Milkovich, S. M., Morlupi, A., Mouginot, J., Orosei, R., Papa, C., Paterno, T., Persi del Marmo, P., Pettinelli, E., Pica, G., Picardi, G., Plaut, J. J., Provenziani, M., Putzig, N.

- E., Russo, F., Safaeinili, A., Salzillo, G., Santovito, M. R., Smrekar, S. E., Tattarletti, B., and Vicari, D. (2007a), Accumulation and erosion of Mars' south polar layered deposits, *Science*, v. 317, 1715-1718, doi: 10.1126/SCIENCE.1144120.
- Seu, R., Phillips, R. J., Biccari, D., Orosei, R., Masdea, A., Picardi, G., Safaeinili, A., Campbell, B. A., Plaut, J. J., Marinangeli, L., Smrekar, S. E., and Nunes, D. C. (2007b), SHARAD sounding radar on the Mars Reconnaissance Orbiter, *Journal of Geophysical Research*, v. 112, E05S05, doi: 10.1029/2006JE002745.
- Slavney, S., and Orosei, R. (2007), Mars Reconnaissance Orbiter: SHARAD radar reduced data record software interface specification, http://pds-geosciences.wustl.edu/mro/mro-m-sharad-4-rdr-v1/mrosh_1xxx/document/rdrsis.pdf, date accessed:12-30-2010, date cited: 12-30-2010.
- Smith, D. E., Zuber, M. T., and Neumann, G. A. (2001), Seasonal variations of snow depth on Mars, *Science*, v. 294, 2141-2146, doi: 10.1126/SCIENCE.1066556.
- Society of Exploration Geophysicist (2002), SEG Y rev 1 Data Exchange format.
- Stimson, G. W. (1998), Introduction to airborne radar, SciTech Publishing Inc., Raleigh.
- Tanaka, K. L. (2005), Geology and insolation-driven climatic history of Amazonian north polar materials on Mars, *Nature*, v. 437, 991-994, doi: 10.1038/nature04065.
- Titus, T. N., Kieffer, H. H., and Christensen, P. R. (2003), Exposed water ice discovered near the south pole of Mars, *Science*, v. 299, 1048-1051, doi: 10.1126/SCIENCE.1080497.
- Tokar, R. L., Elphic, R. C., Feldman, W. C., Funsten, H. O., Moore, K. R., Prettyman, T. H., and Wiens, R. C. (2003), Mars odyssey neutron sensing of the south residual polar cap, *Geophysical Research Letters*, v. 30, 13, 1677, doi: 10.1029/2003GL017316.
- Tsoflias, G. P., and Hoch, A. (2004), Investigating multi-polarization GPR wave transmission through thin layers: Implication for vertical fracture

characterization, *Geophysical Research Letters*, v. 33, L20401, doi: 10.1029/2006GL027788.

Zurek, R. W., and Smrekar, S. E. (2007), An overview of the Mars Reconnaissance Orbiter (MRO) science mission, *Journal of Geophysical Research*, v. 112, E05S01, doi: 10.1029/2006JE002701.

Appendices

Appendix A: List of datasets selected

		Track	Trace Chosen	Acquisition Start Time	Is	Season
Winter	Early	FPA_9222C1000_1_Mode_001	17500-20999	2008-07-15-T01:20:52.1743	58.8	Early SH Winter
		FPA_9888C1000_1_Mode_001	34000-37499	2008-07-27-T23:45:54.6404	104.61	Early SH Winter
	Mid	FPA_9955C1000_1_Mode_001	34000-36999	2008-09-10-T04:08:22.1332	125.02	Mid SH Winter
		FPA_10066C1000_1_Mode_001	14500-18999	2008-09-18-T19:45:17.5241	125.14	Mid SH Winter
	Late	FPA_2413C1000_1_Mode_003	0-2999	2007-01-31-T10:54:49.7524	175.9	Late SH Winter
		FPA_10865C1000_1_Mode_001	21500-23999	2008-11-20-T02:04:16.3279	160.5	Late SH Winter
		FPA_11274C1000_1_Mode_001	21500-24499	2008-12-21-T22:58:33.5119	177.87	Late SH Winter
Spring	Early	FPA_2624C1000_1_Mode_003	0-3499	2007-02-16-T21:30:11.2911	185.18	Early SH Spring
		FPA_11920C1000_1_Mode_001	21500-22999	2009-02-10-T07:04:09.5634	207.23	Early SH Spring
	Mid	FPA_3257C1000_1_Mode_002	5500-7999	2007-04-07-T05:15:04.1027	214.48	Mid SH Spring
		FPA_3297C1000_1_Mode_001	27000-29499	2007-04-10-T07:54:48.9339	216.39	Mid SH Spring
		FPA_3315C1000_1_Mode_001	14500-16999	2007-04-11-T17:34:31.3842	217.25	Mid SH Spring
		FPA_3468C1000_1_Mode_001	21000-24499	2007-04-23-T15:43:55.2767	224.65	Mid SH Spring
		FPA_3679C1000_1_Mode_001	21000-23999	2007-05-10-T02:19:48.4640	234.96	Mid SH Spring
		FPA_12400C1000_1_Mode_001	17000-19999	2009-03-19-T16:38:50.7316	230.32	Mid SH Spring
		FPA_12553C1000_1_Mode_001	34500-37499	2009-03-31-T14:45:18.5722	237.83	Mid SH Spring
	Late	FPA_4107C1000_1_Mode_001	21000-23499	2007-06-11-T23:31:12.2392	255.79	Late SH Spring
		FPA_4172C1000_1_Mode_001	2000-4499	2007-06-17-T12:20:25.5843	259.3	Late SH Spring
		FPA_4212C1000_1_Mode_001	1000-4499	2007-06-20-T15:08:38.0307	261.28	Late SH Spring
		FPA_4220C1000_1_Mode_001	7500-4999	2007-06-21-T06:10:43.2805	261.67	Late SH Spring
		FPA_4286C1000_1_Mode_001	29000-31999	2007-06-26-T09:25:56.3762	264.92	Late SH Spring
		FPA_4312C1000_1_Mode_001	21500-23499	2007-06-28-T10:06:19.0252	266.2	Late SH Spring
		FPA_4357C1000_1_Mode_001	1500-4499	2007-07-01-T22:18:31.2231	268.41	Late SH Spring
Summer	Early	FPA_4423C1000_1_Mode_001	1000-3999	2007-07-07-T01:44:21.7676	271.64	Early SH Summer
		FPA_4437C1000_1_Mode_001	2000-4999	2007-07-07-T16:46:28.4678	272.04	Early SH Summer
		FPA_4436C1000_1_Mode_001	2000-2599	2007-07-08-T02:02:59.6173	272.28	Early SH Summer
		FPA_4444C1000_1_Mode_001	2500-4499	2007-07-08-T17:05:10.4175	272.67	Early SH Summer
		FPA_4457C1000_1_Mode_001	1500-4999	2007-07-09-T17:24:04.5162	273.31	Early SH Summer
		FPA_4587C1000_1_Mode_001	1500-4799	2007-07-19-T09:12:26.4592	275.34	Early SH Summer
		FPA_4594C1000_1_Mode_001	2000-4499	2007-07-20-T09:31:02.8090	275.97	Early SH Summer
		FPA_4713C1000_1_Mode_001	18500-18999	2007-07-29-T15:58:04.2982	285.7	Early SH Summer
		FPA_4727C1000_1_Mode_001	28500-31999	2007-07-30-T06:53:40.8974	286.08	Early SH Summer
		FPA_4734C1000_1_Mode_001	21500-23499	2007-07-31-T07:17:17.7988	286.71	Early SH Summer
		FPA_13547C1000_1_Mode_001	7000-10499	2009-06-17-T01:44:16.8157	286.6	Early SH Summer
	Mid	FPA_5214C1000_1_Mode_001	16500-18999	2007-09-06-T16:55:06.4186	305.16	Mid SH Summer
		FPA_5222C1000_1_Mode_001	28500-30499	2007-09-07-T07:52:41.5658	306.52	Mid SH Summer
		FPA_5570C1000_1_Mode_001	17000-19499	2007-10-04-T10:41:20.6953	325.02	Mid SH Summer
		FPA_13832C1000_1_Mode_001	34500-36499	2009-07-09-T06:38:04.7450	300.07	Mid SH Summer
		FPA_14043C1000_1_Mode_001	34500-37999	2009-07-25-T17:14:00.5834	305.78	Mid SH Summer
	Late	FPA_5723C1000_1_Mode_001	29000-31499	2007-10-16-T08:49:08.6895	331.61	Late SH Summer
		FPA_5789C1000_1_Mode_001	21500-24999	2007-10-21-T12:17:46.0659	334.42	Late SH Summer
Autumn	Early	FPA_7007C1000_1_Mode_001	9500-11999	2008-01-24-T10:17:43.6134	22.08	Early SH Autumn
		FPA_7055C1000_1_Mode_001	21000-23999	2008-01-28-T04:04:12.1097	23.83	Early SH Autumn
		FPA_7068C1000_1_Mode_001	28500-32499	2008-01-29-T04:19:56.2545	24.3	Early SH Autumn
		FPA_7073C1000_1_Mode_001	10000-12199	2008-01-29-T13:44:02.2073	24.48	Early SH Autumn
		FPA_7200C1000_1_Mode_001	21000-23999	2008-02-08-T11:15:55.9516	26.06	Early SH Autumn
		FPA_7218C1000_1_Mode_001	9500-11999	2008-02-09-T20:56:01.7990	25.71	Early SH Autumn
	Mid	FPA_7416C1000_1_Mode_001	17000-19499	2008-02-25-T07:14:38.7347	36.74	Mid SH Autumn
		FPA_7429C1000_1_Mode_001	8300-11999	2008-02-26-T07:36:36.5863	37.19	Mid SH Autumn
		FPA_7495C1000_1_Mode_001	8300-11999	2008-03-02-T11:03:46.1326	35.51	Mid SH Autumn
		FPA_7840C1000_1_Mode_001	8500-11999	2008-03-13-T18:16:57.7730	44.58	Mid SH Autumn
		FPA_7706C1000_1_Mode_001	9500-11999	2008-03-18-T21:44:04.2091	46.87	Mid SH Autumn
		FPA_7857C1000_1_Mode_001	9000-11499	2008-03-30-T04:57:09.5601	51.87	Mid SH Autumn
		FPA_7917C1000_1_Mode_001	9000-11499	2008-04-04-T08:24:13.3572	54.14	Mid SH Autumn
		FPA_8062C1000_1_Mode_001	9500-11999	2008-04-15-T15:37:11.1498	59.1	Mid SH Autumn
	Late	FPA_8787C1000_1_Mode_001	17000-19499	2008-06-11-T03:44:17.6506	83.81	Late SH Autumn
		FPA_8867C1000_1_Mode_001	29000-32499	2008-06-16-T22:09:48.0464	86.34	Late SH Autumn

Appendix B: Data loading and editing scripts in IDL

```
.*****
; This IDL script is to extract SHARAD data into a 2-D array and also extract coordinates. The 2-
; D array is then saved into the ASCII format and coordinates are saved into the CSV format.
.*****
FUNCTION read_mlk, fname

; Extracting info from the input file
finfo = FILE_INFO(fname)

; Calculate the # of frames/traces
frames = LONG(finfo.size/16384L)

; Setting up a 2-D array to load all the traces
mlking = FLTARR(4096L,frames)

; Open and read the input file into 10
OPENR, 10, fname

; Read unformatted binary data from a file or 10 into IDL variable "mlking"
READU, 10, mlking

CLOSE, 10

FREE_LUN, 10

RETURN, mlking

END
.*****
PRO mlking_raw

; Input file path
mlking = read_mlk('/cresis/data1/MARSIS/sharad_data/FPA_PROD/FPA_563101000_1/FPA_56
3101000_1_Mode_001.dat.mlk')

; Check the dimension of the mlking and print it on the screen
dimension = SIZE(mlking,/DIMENSIONS)
PRINT, "mlking = ", dimension[0], " ROWS and ", dimension[1], " COLUMNS"

; Truncate mlking if necessary to get rid of the unwanted portion of the data
truncated_mlking = mlking(*,29000:31499)

; Check the dimension of the truncated_mlking and print it on the screen
dimension = SIZE(truncated_mlking,/DIMENSIONS)
PRINT, "truncated_mlking = ", dimension[0], " ROWS and ", dimension[1], " COLUMNS"
```

```

; Create a file and write the 2-D array to the file
OPENW,lun, 'FPA_563101000_1_Mode_001_no_dervi.dat',/GET_LUN

FOR i = 0, dimension[0]-1 DO PRINTF, LUN, truncated_mlkimg(i,0:dimension[1]-1), FORMAT
= "(60000E13.5)"

FREE_LUN, LUN

; Check if the file has been created
IF FILE_TEST('/cresis/data1/MARSIS/sharad_data/SEGY/Default/FPA_563101000_1_Mode_00
1_no_dervi.dat') EQ 1 THEN PRINT, "MLKIMG.DAT EXISTS!!" ELSE PRINT,
"MLKIMG.DAT DOESN'T EXIST!!"

END
.*****
PRO import_coordinate

mlking_raw

; Look for the file that contains the coordinate information
file_name = '/cresis/data1/MARSIS/sharad_data/FPA_PROD/FPA_563101000_1/FPA_56310100
0_1_Mode_001.dat.etm'

; Read the file
coordinate = READ_ASCII(file_name, TEMPLATE=ASCII_TEMPLATE(file_name))

; Check how many coordinates the file contains and create a 2-D array. Column 1 is the latitude
; values and Column 2 is the longitude values. Each row represents one trace
column = (size(coordinate.FIELD05))[1]
coordinate_pair = FLTARR(column,2)

; Copy all the latitude and longitude values from the input file
coordinate_pair(*,0) = coordinate.FIELD05
coordinate_pair(*,1) = coordinate.FIELD06

; Create 2 arrays for the csv file
trace_number = MAKE_ARRAY(column,1, /STRING, VALUE = 0)
CSV = MAKE_ARRAY(column,1, /STRING, VALUE = 0)

; Copy coordinates into CSV
FOR i = 0L, column-1 DO BEGIN
    CSV(i,0) = STRING(coordinate_pair(i * 1,0), FORMAT = '(F0)') + ',' +
    STRING(coordinate_pair(i * 1,1), FORMAT = '(F0)')
ENDFOR

; The # of rows should be equal to the # of traces that were kept in the data file
CSV = CSV(29000:31499,0)

; Check the size of CSV
dimension = SIZE(CSV, /DIMENSION)

```

```

; Add the trace numbers in the 1st column
FOR i = 0L, dimension[0] - 1 DO BEGIN
    trace_number(i) = i + 1
    CSV(i,0) = trace_number(i) + ',' + CSV(i,0)
ENDFOR

; Create a csv file and write an output file
OPENW, LUN, 'FPA_563101000_1_Mode_001_no_dervi.csv', /GET_LUN

FOR i = 0L, dimension[0] - 1 DO PRINTF, LUN, CSV(i,0)

FREE_LUN, LUN

END
.*****
;
PRO main

import_coordinate

END

```

Appendix C: Loading and writing data to SEG-Y in MATLAB

```
clear all; clc;
```

```
filename{01} = 'FPA_922201000_1_Mode_001_no_dervi.dat';  
filename{02} = 'FPA_938801000_1_Mode_001_no_dervi.dat';  
filename{03} = 'FPA_995501000_1_Mode_001_no_dervi.dat';  
filename{04} = 'FPA_1006601000_1_Mode_001_no_dervi.dat';  
filename{05} = 'FPA_241301000_1_Mode_003_no_dervi.dat';  
filename{06} = 'FPA_1086501000_1_Mode_001_no_dervi.dat';  
filename{07} = 'FPA_1127401000_1_Mode_001_no_dervi.dat';  
filename{08} = 'FPA_262401000_1_Mode_003_no_dervi.dat';  
filename{09} = 'FPA_1192001000_1_Mode_001_no_dervi.dat';  
filename{10} = 'FPA_325701000_1_Mode_002_no_dervi.dat';  
filename{11} = 'FPA_329701000_1_Mode_001_no_dervi.dat';  
filename{12} = 'FPA_331501000_1_Mode_001_no_dervi.dat';  
filename{13} = 'FPA_346801000_1_Mode_001_no_dervi.dat';  
filename{14} = 'FPA_367901000_1_Mode_001_no_dervi.dat';  
filename{15} = 'FPA_1240001000_1_Mode_001_no_dervi.dat';  
filename{16} = 'FPA_1255301000_1_Mode_001_no_dervi.dat';  
filename{17} = 'FPA_410101000_1_Mode_001_no_dervi.dat';  
filename{18} = 'FPA_417201000_1_Mode_001_no_dervi.dat';  
filename{19} = 'FPA_421201000_1_Mode_001_no_dervi.dat';  
filename{20} = 'FPA_422001000_1_Mode_001_no_dervi.dat';  
filename{21} = 'FPA_428601000_1_Mode_001_no_dervi.dat';  
filename{22} = 'FPA_431201000_1_Mode_001_no_dervi.dat';  
filename{23} = 'FPA_435701000_1_Mode_001_no_dervi.dat';  
filename{24} = 'FPA_442301000_1_Mode_001_no_dervi.dat';  
filename{25} = 'FPA_443101000_1_Mode_001_no_dervi.dat';  
filename{26} = 'FPA_443601000_1_Mode_001_no_dervi.dat';  
filename{27} = 'FPA_444401000_1_Mode_001_no_dervi.dat';  
filename{28} = 'FPA_445701000_1_Mode_001_no_dervi.dat';  
filename{29} = 'FPA_458101000_1_Mode_001_no_dervi.dat';  
filename{30} = 'FPA_459401000_1_Mode_001_no_dervi.dat';  
filename{31} = 'FPA_471301000_1_Mode_001_no_dervi.dat';  
filename{32} = 'FPA_472101000_1_Mode_001_no_dervi.dat';  
filename{33} = 'FPA_473401000_1_Mode_001_no_dervi.dat';  
filename{34} = 'FPA_1354701000_1_Mode_001_no_dervi.dat';  
filename{35} = 'FPA_521401000_1_Mode_001_no_dervi.dat';  
filename{36} = 'FPA_522201000_1_Mode_001_no_dervi.dat';  
filename{37} = 'FPA_557001000_1_Mode_001_no_dervi.dat';  
filename{38} = 'FPA_1383201000_1_Mode_001_no_dervi.dat';  
filename{39} = 'FPA_1404301000_1_Mode_001_no_dervi.dat';  
filename{40} = 'FPA_572301000_1_Mode_001_no_dervi.dat';  
filename{41} = 'FPA_578901000_1_Mode_001_no_dervi.dat';  
filename{42} = 'FPA_700701000_1_Mode_001_no_dervi.dat';  
filename{43} = 'FPA_705501000_1_Mode_001_no_dervi.dat';  
filename{44} = 'FPA_706801000_1_Mode_001_no_dervi.dat';
```

```

filename{45} = 'FPA_707301000_1_Mode_001_no_dervi.dat';
filename{46} = 'FPA_720001000_1_Mode_001_no_dervi.dat';
filename{47} = 'FPA_721801000_1_Mode_001_no_dervi.dat';
filename{48} = 'FPA_741601000_1_Mode_001_no_dervi.dat';
filename{49} = 'FPA_742901000_1_Mode_001_no_dervi.dat';
filename{50} = 'FPA_749501000_1_Mode_001_no_dervi.dat';
filename{51} = 'FPA_764001000_1_Mode_001_no_dervi.dat';
filename{52} = 'FPA_770601000_1_Mode_001_no_dervi.dat';
filename{53} = 'FPA_785101000_1_Mode_001_no_dervi.dat';
filename{54} = 'FPA_791701000_1_Mode_001_no_dervi.dat';
filename{55} = 'FPA_806201000_1_Mode_001_no_dervi.dat';
filename{56} = 'FPA_878701000_1_Mode_001_no_dervi.dat';
filename{57} = 'FPA_886101000_1_Mode_001_no_dervi.dat';

addpath ('.\Default' , '\SegyMAT')

for i = 1 : length(filename)

    clear mlking

    if length(filename{i}) == 37
        mlking = importdata(filename{i});
        WriteSegy([filename{i}(1:24),'.sgy'],mlking,'dt',0.00375,'revision',1);
    else
        mlking = importdata(filename{i});
        WriteSegy([filename{i}(1:25),'.sgy'],mlking,'dt',0.00375,'revision',1);
    end

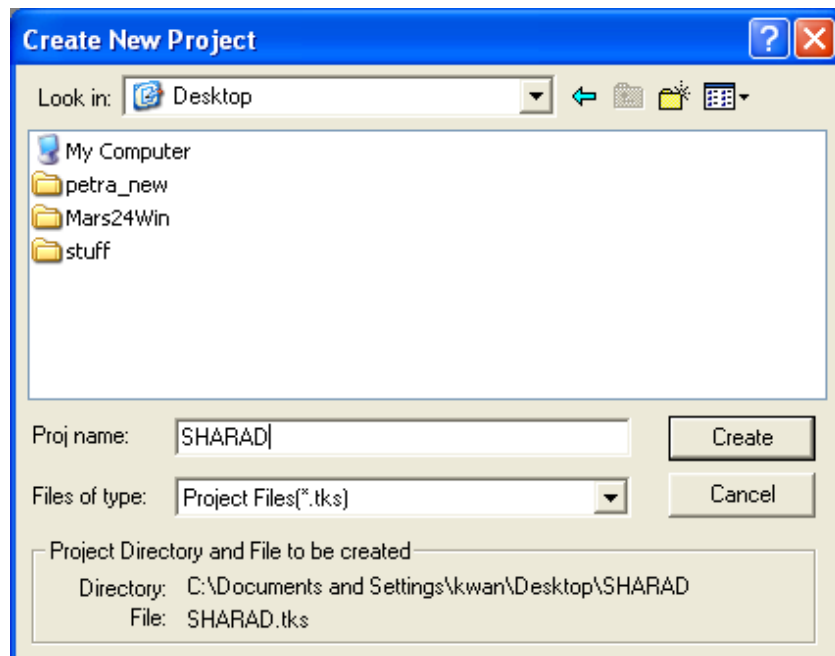
end

```

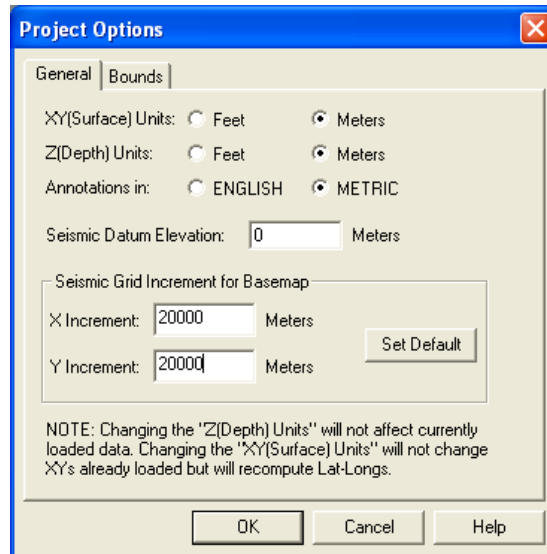
Appendix D: Loading data into Kingdom Suite



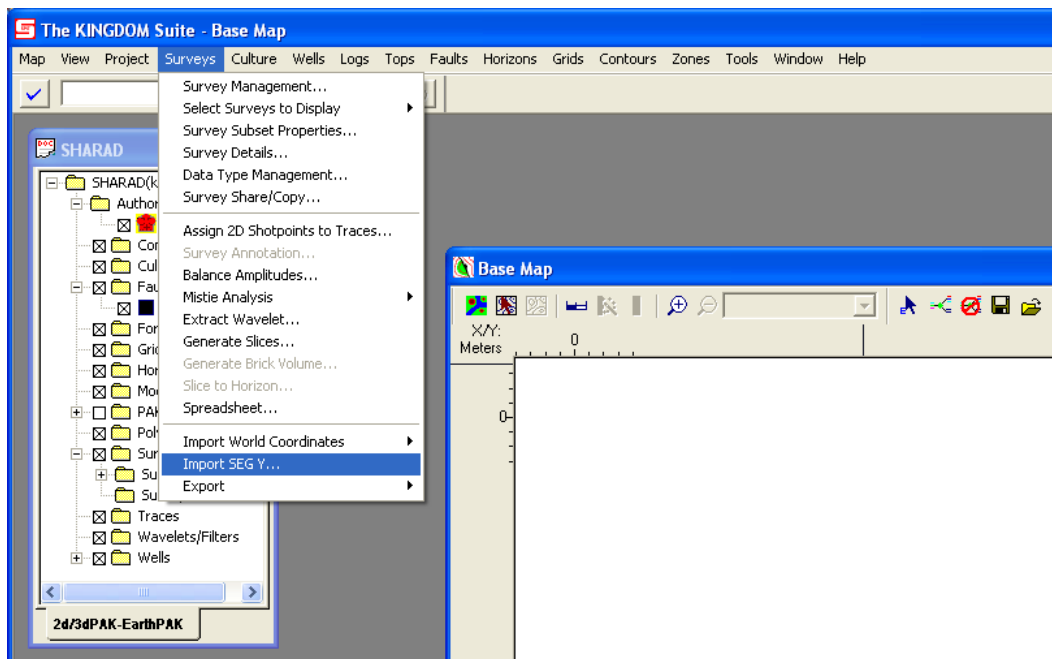
D-1 Launch Kingdom Suite → click Project → click Create New Project



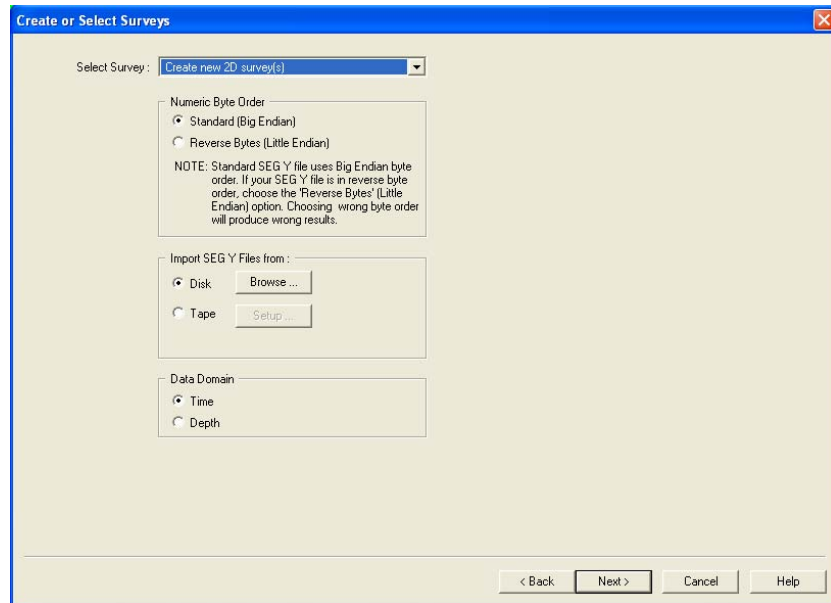
D-2 Define a project name and a location to save the project → click Create
Enter a name of the author → click OK
Highlight “MS Access XP” as the project database → click OK



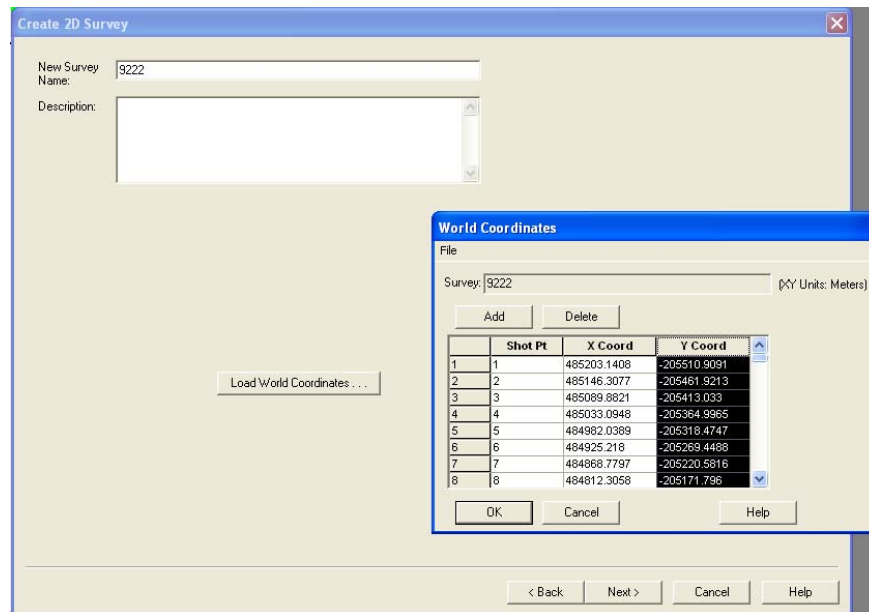
- D-3** Set “XY (Surface) Units” and “Z (Depth) Units” to Meters
 Set “Annotations in to” to Metric
 Set “X Increment” and “Y Increment” to 20000 Meters
 Click OK → click Yes → click No



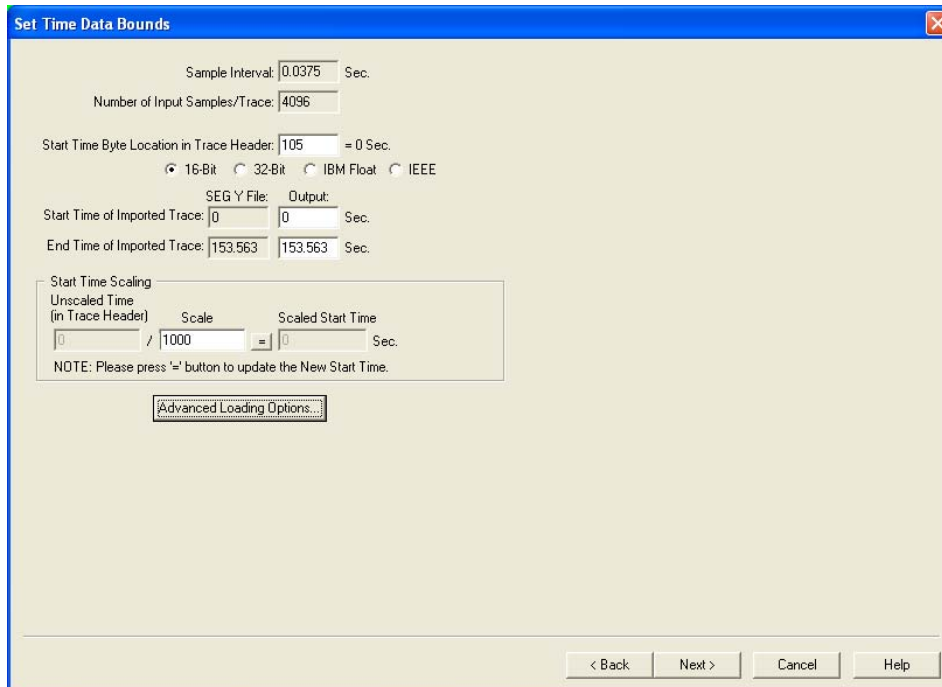
- D-4** An empty base map appears
 Click Survey → click Import SEG Y ... → click Next



D-5 Click Browse and select a SEG-Y file → click Open → click Next
Select “Amplitudes” → click Next



D-6 Create a new survey name for the SEG-Y file that is being imported
Click “Load World Coordinates ...” to import coordinates
Click OK → click Next
Choose “Trace Sequence Number by Counting” → click Next



Set Time Data Bounds

Sample Interval: 0.0375 Sec.

Number of Input Samples/Trace: 4096

Start Time Byte Location in Trace Header: 105 = 0 Sec.

☒ 16-Bit ☐ 32-Bit ☐ IBM Float ☐ IEEE

SEG Y File: Output:

Start Time of Imported Trace: 0 0 Sec.

End Time of Imported Trace: 153.563 153.563 Sec.

Start Time Scaling

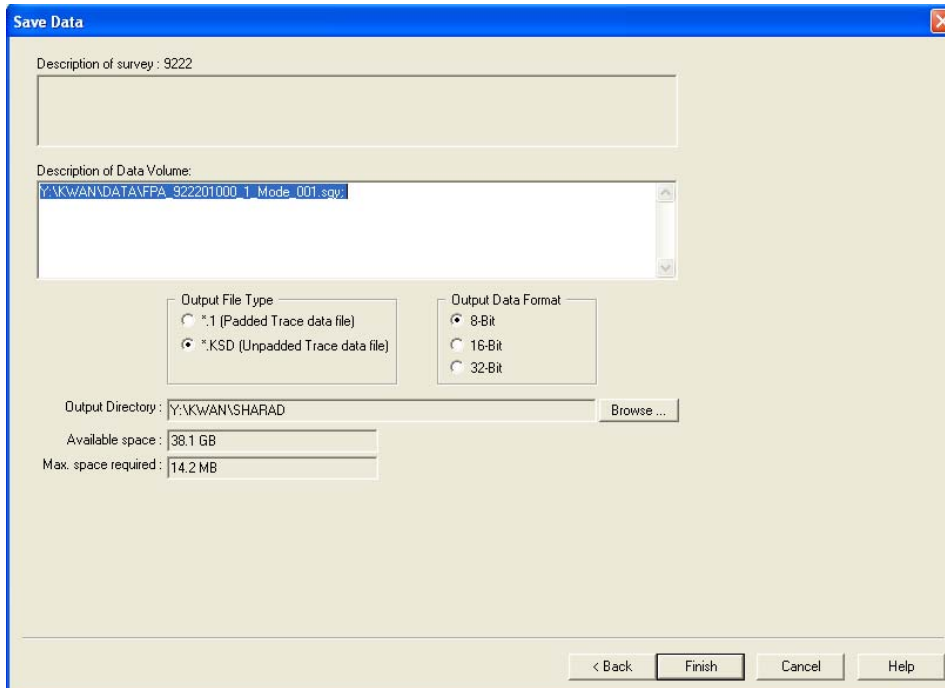
Unscaled Time (in Trace Header)	Scale	Scaled Start Time
0	/ 1000	0 Sec.

NOTE: Please press '=' button to update the New Start Time.

[Advanced Loading Options...](#)

< Back Next > Cancel Help

D-7 No changes in “Set Time Data Bounds” section → click Next



Save Data

Description of survey : 9222

Description of Data Volume:

Y:\KWAN\DATA\FPA_922201000_1_Mode_001.sgy

Output File Type

☐ *.1 (Padded Trace data file)

☒ *.KSD (Unpadded Trace data file)

Output Data Format

☒ 8-Bit

☐ 16-Bit

☐ 32-Bit

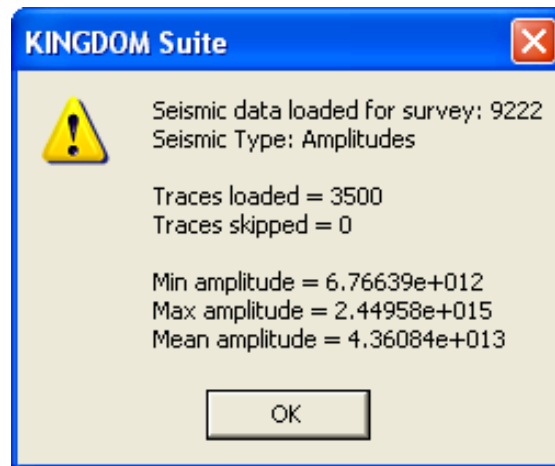
Output Directory : Y:\KWAN\SHARAD [Browse ...](#)

Available space : 38.1 GB

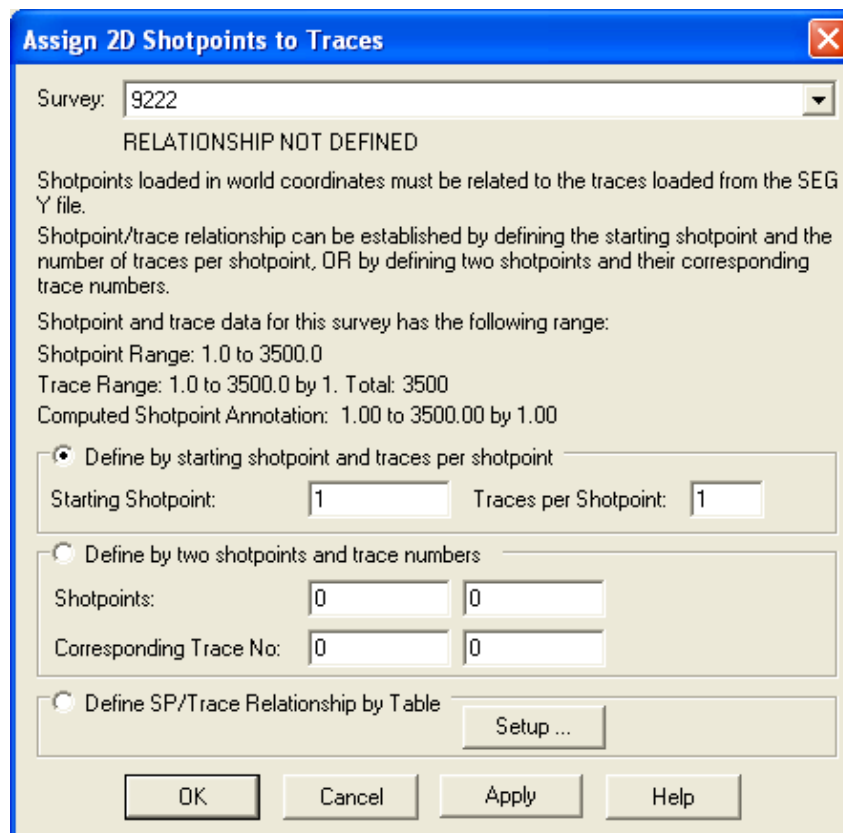
Max. space required : 14.2 MB

< Back Finish Cancel Help

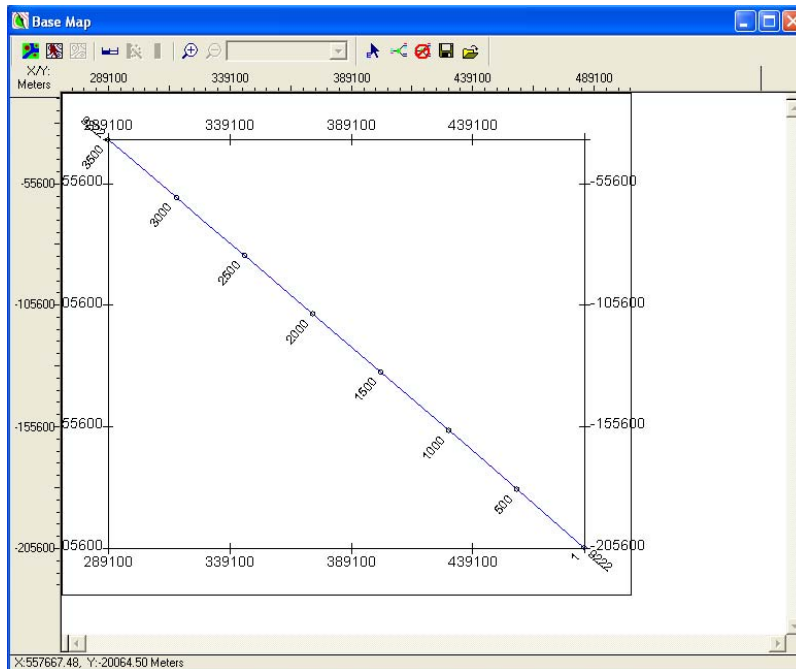
D-8 No changes in “Save Data” section → click Finish



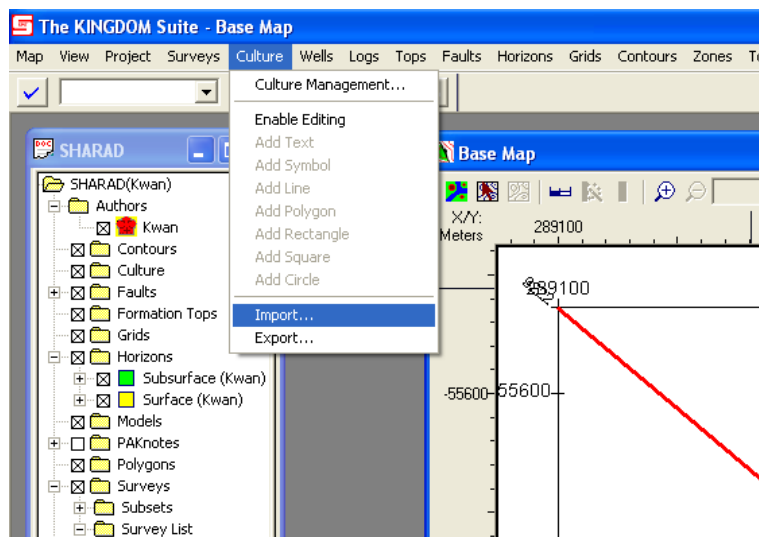
D-9 A summary appears about the SEG-Y file → click OK



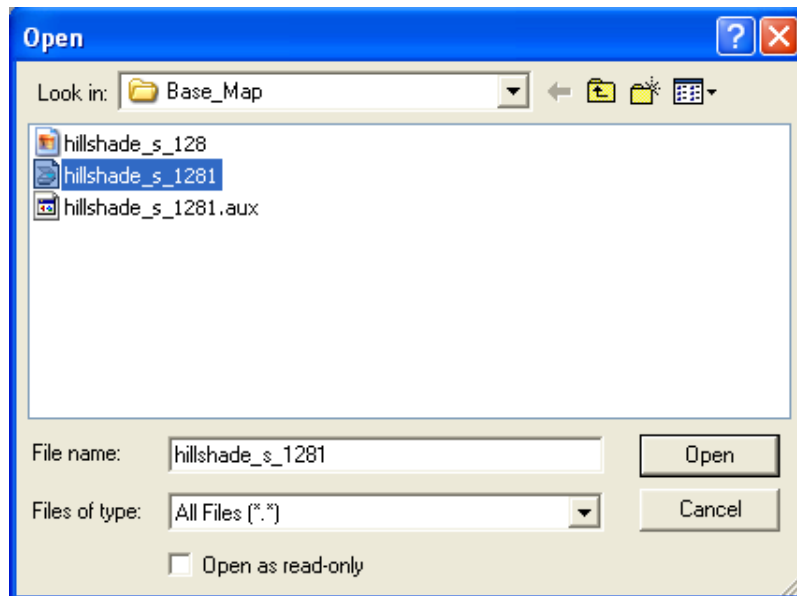
D-10 “Traces per Shotpoints” should be set to 1, so each shotpoint represents one trace → click OK



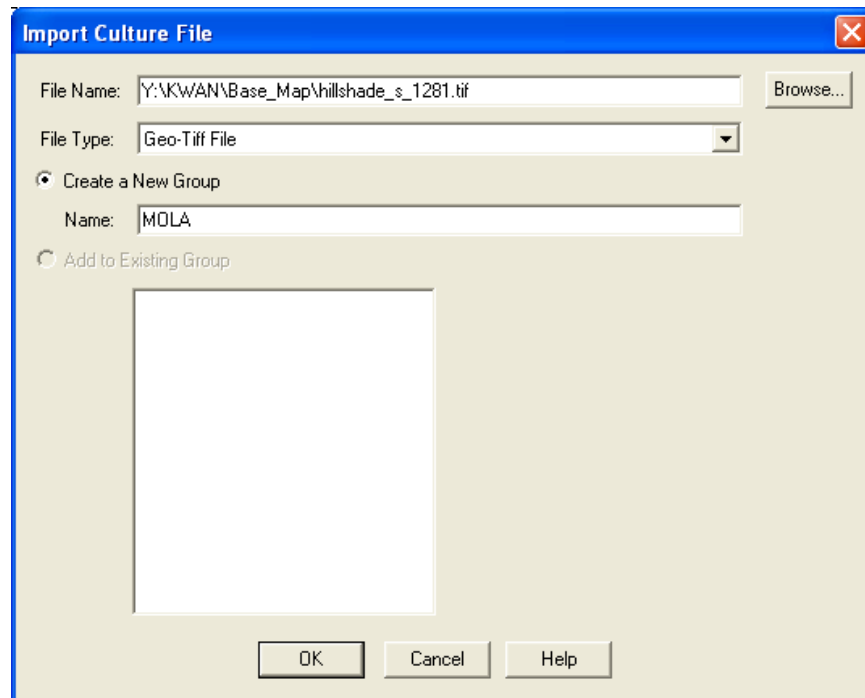
D-11 The SEG-Y file has been loaded successfully. All the traces along the orbital track (blue line) on the base map are placed based on their corresponding coordinates. The radar cross-section should appear by double-clicking the orbital track.



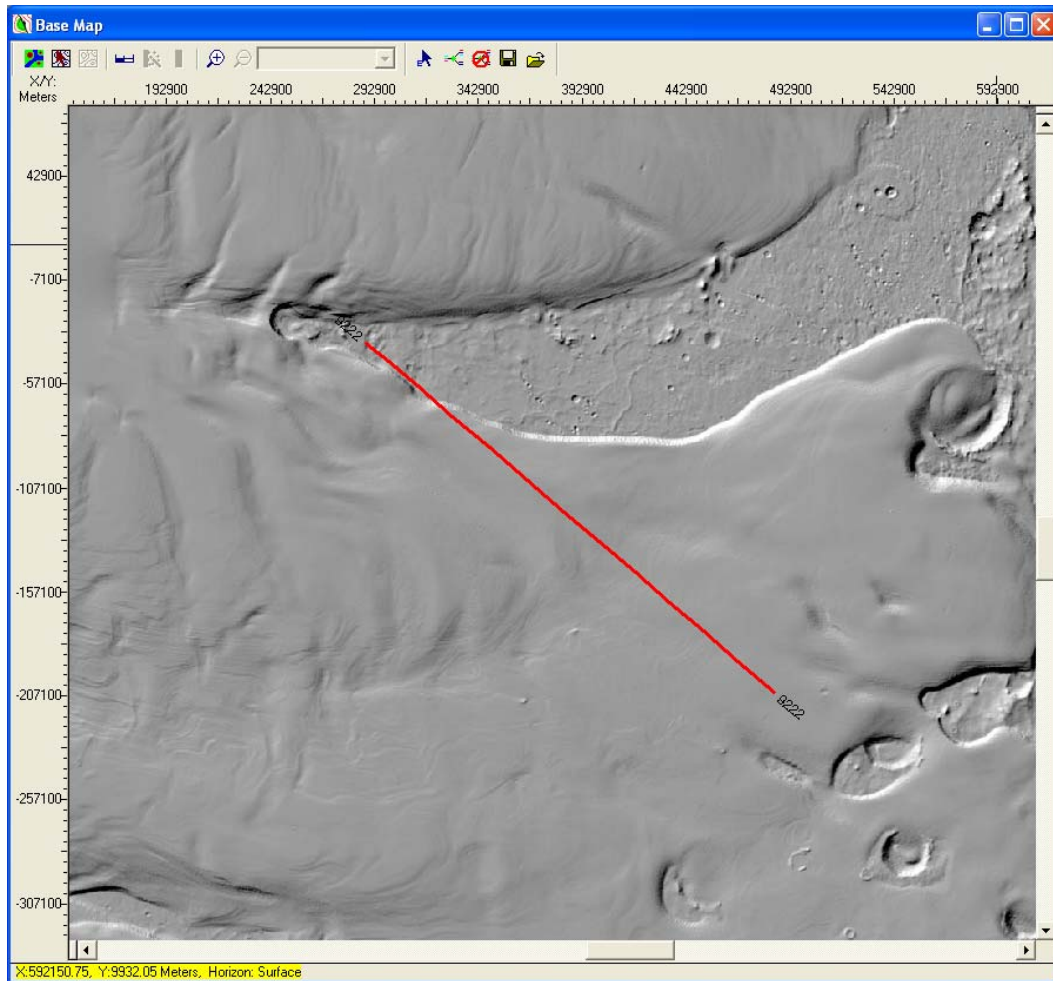
D-12 If a digital elevation model (DEM) in the Geo-Tiff format is available, it can be loaded onto the “Base Map” as a background. Click Culture → “Import...”



- D-13** Set “Files of Type” to “All Files”
Select the appropriate file → click Open

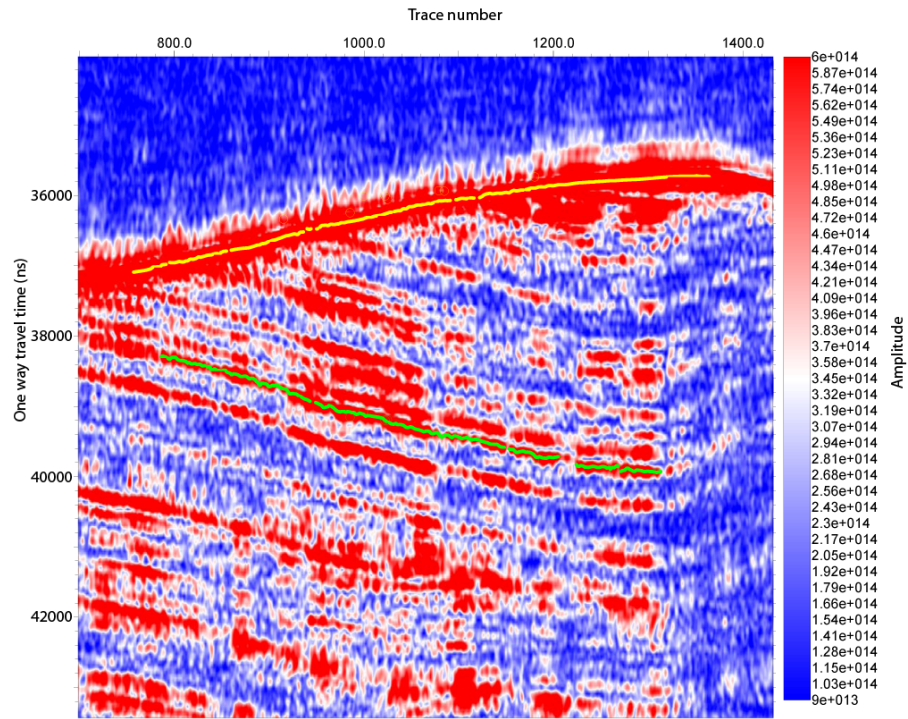


- D-14** Set “File Type” to “Geo-Tiff File”
Define a name for a new group that the Geo-Tiff file is located within

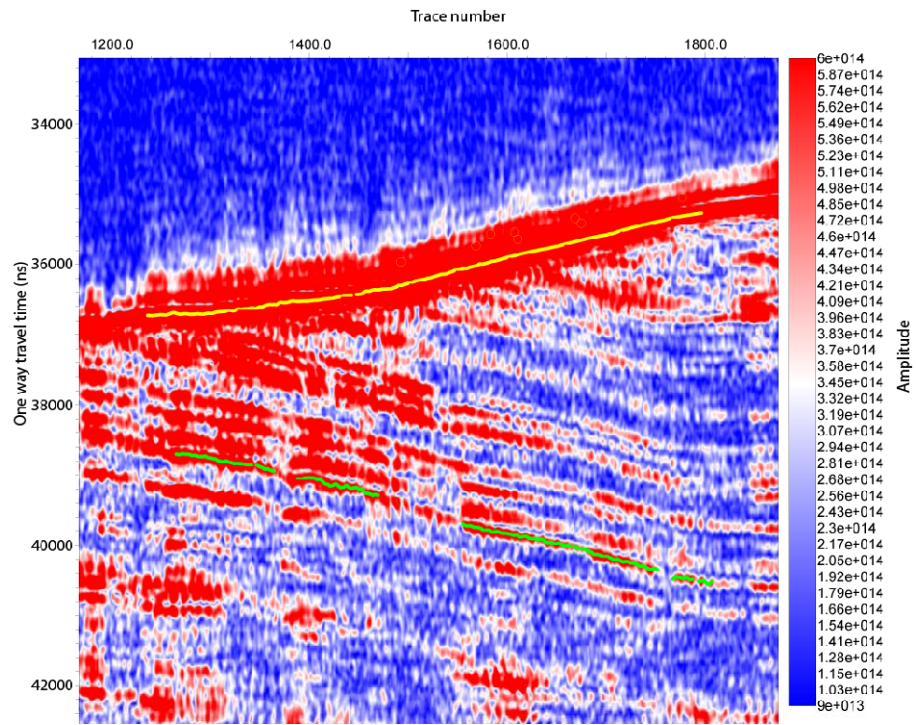


D-15 The DEM is now loaded as a background on the Base Map

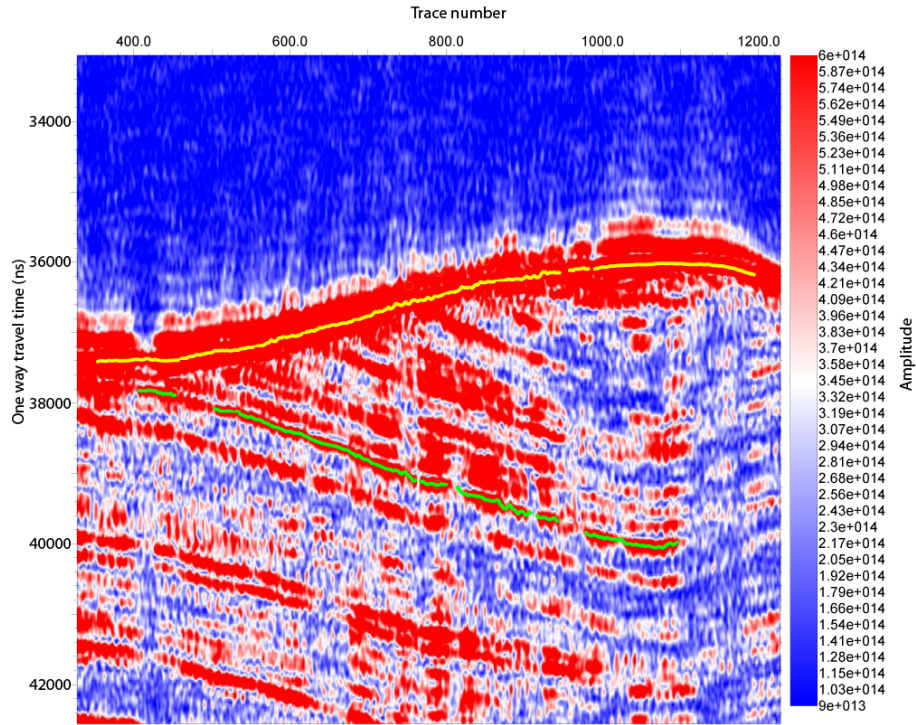
Appendix E: Twelve selected orbital tracks



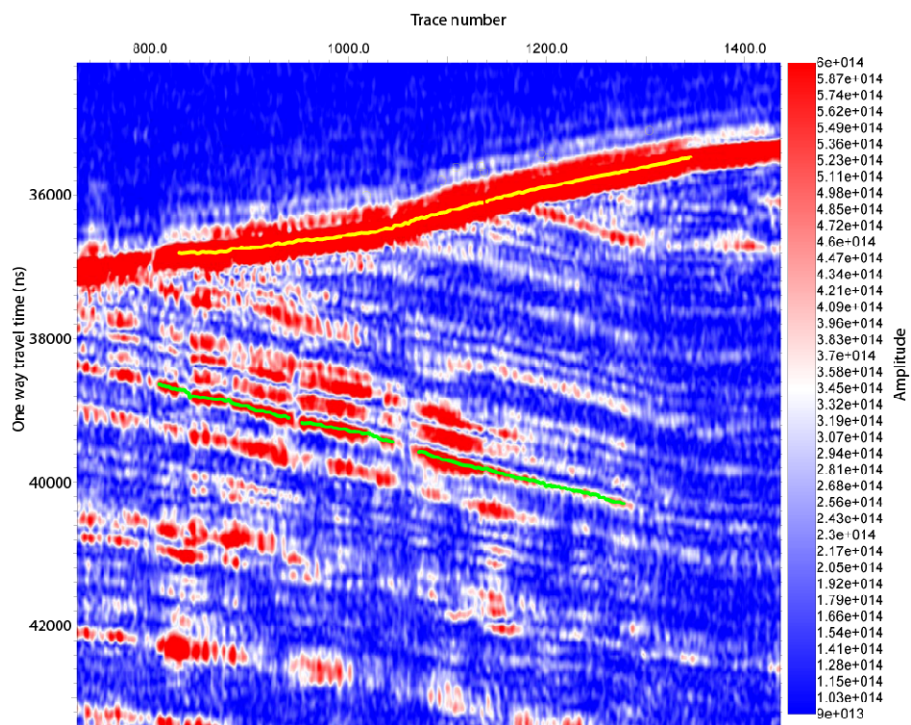
Track 4444 (Cross-line)



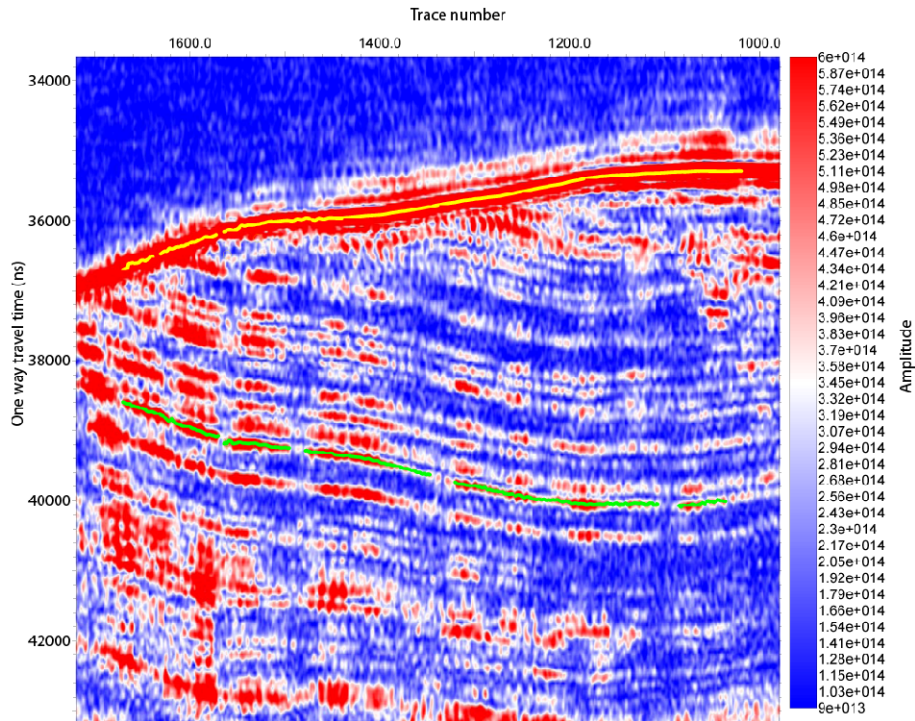
Track 5723 (Cross-line)



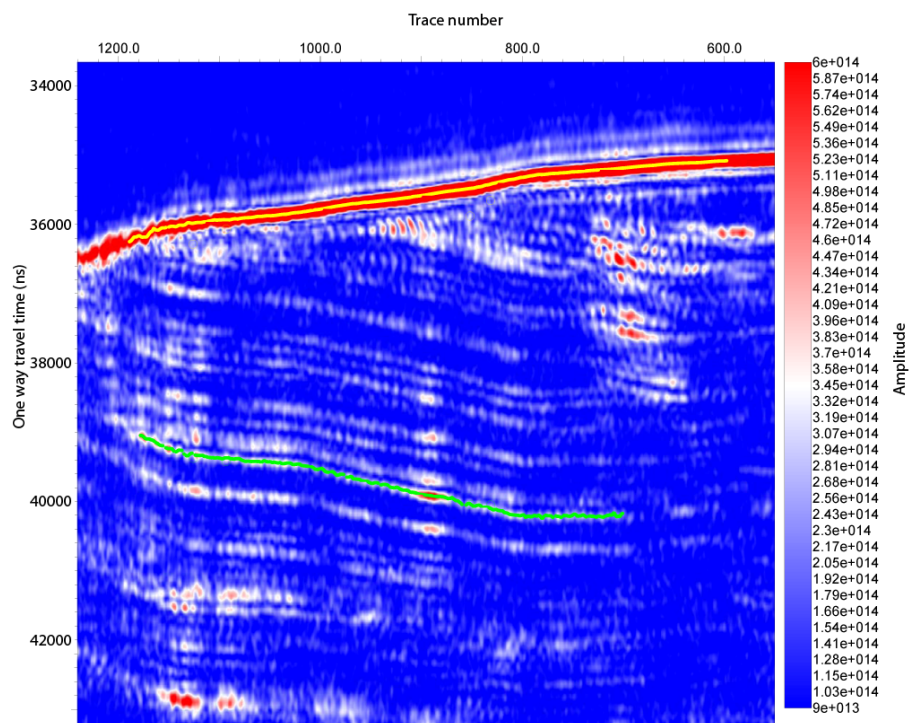
Track 5789 (Cross-line)



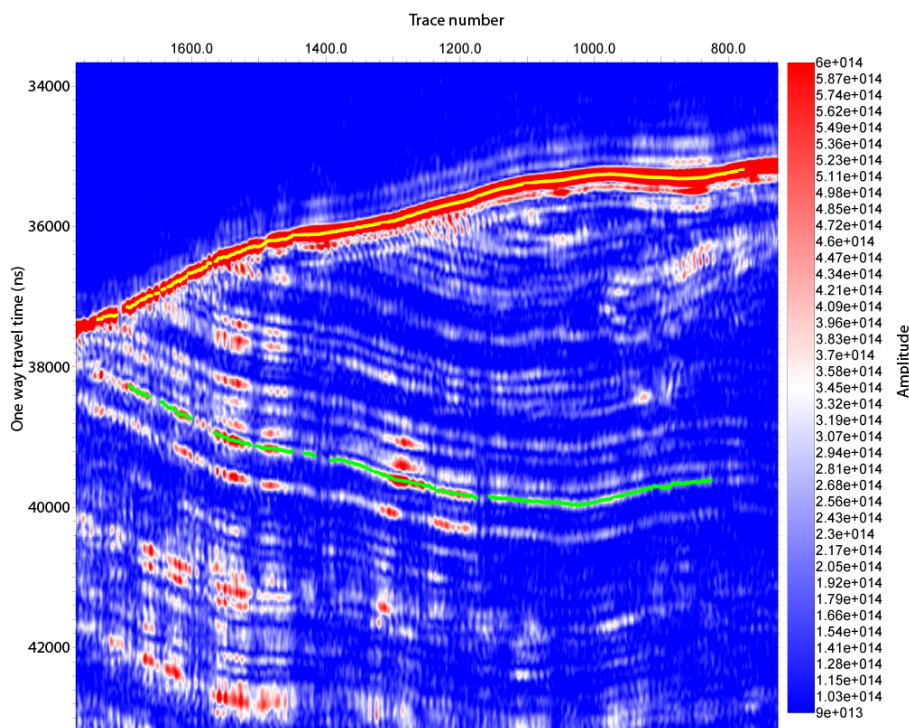
Track 11920 (Cross-line)



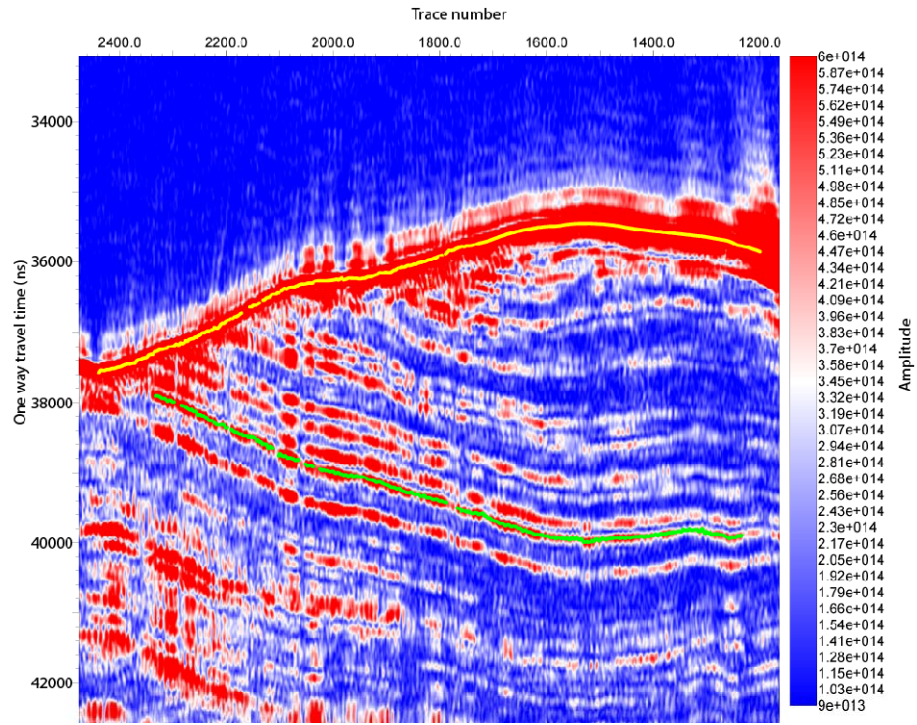
Track 4436 (In-line)



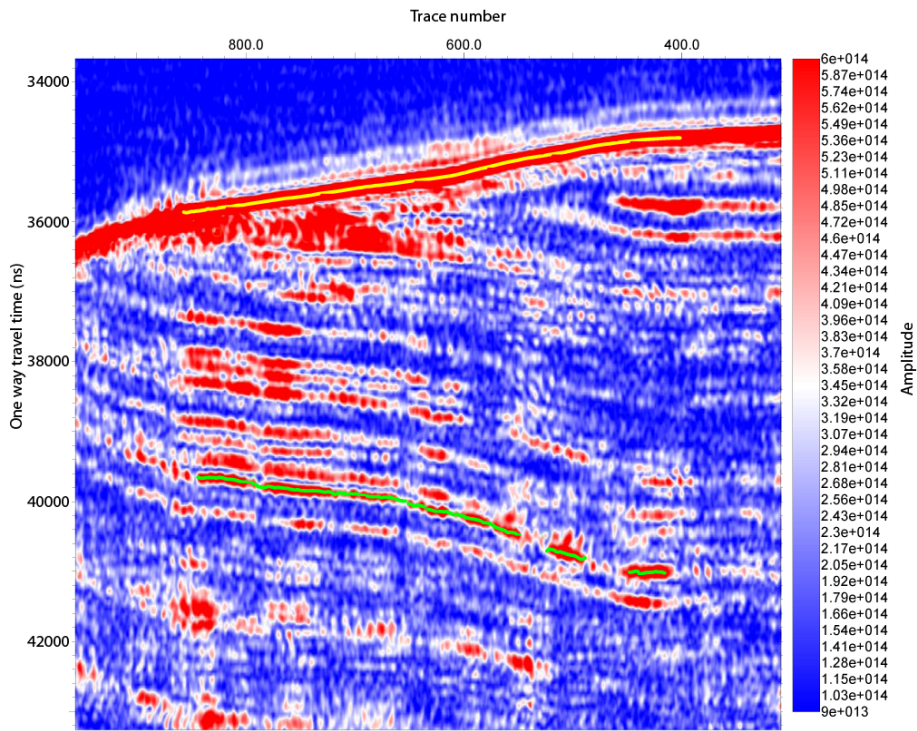
Track 5214 (In-line)



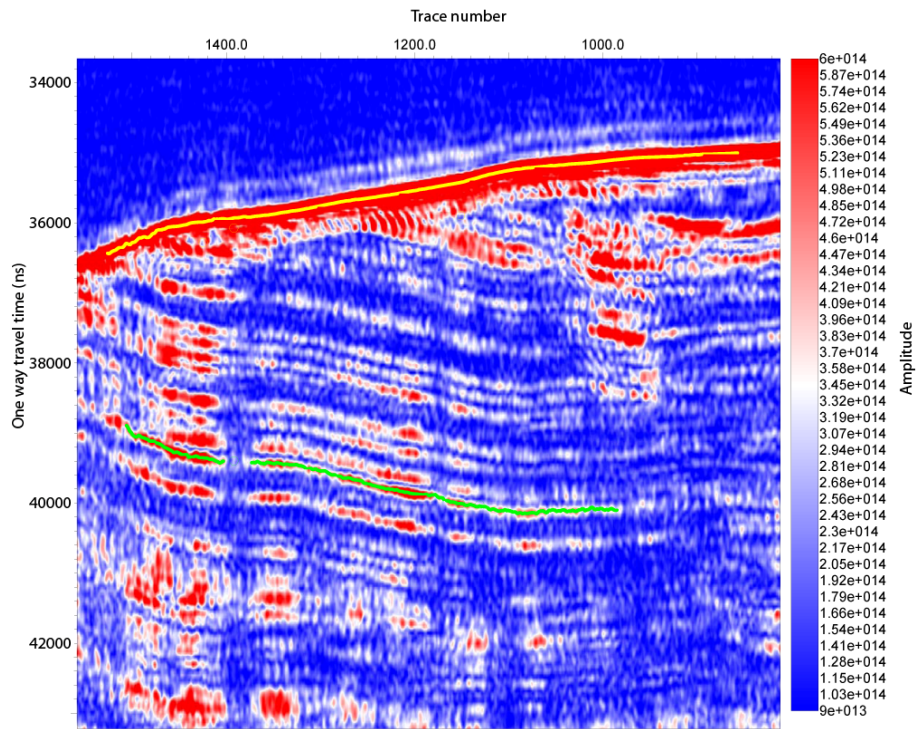
Track 5570 (In-line)



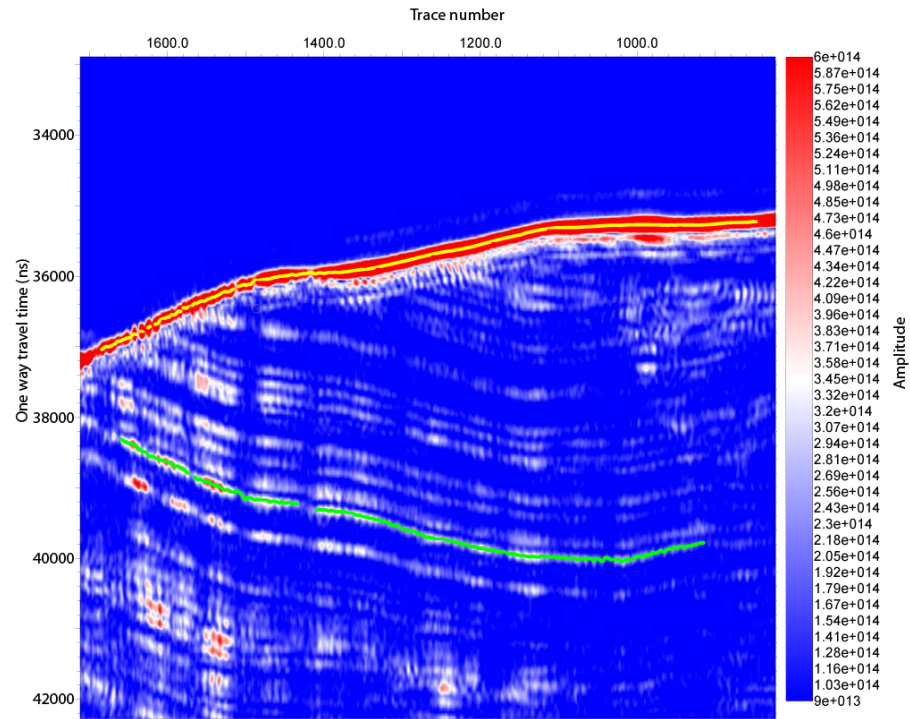
Track 7495 (In-line)



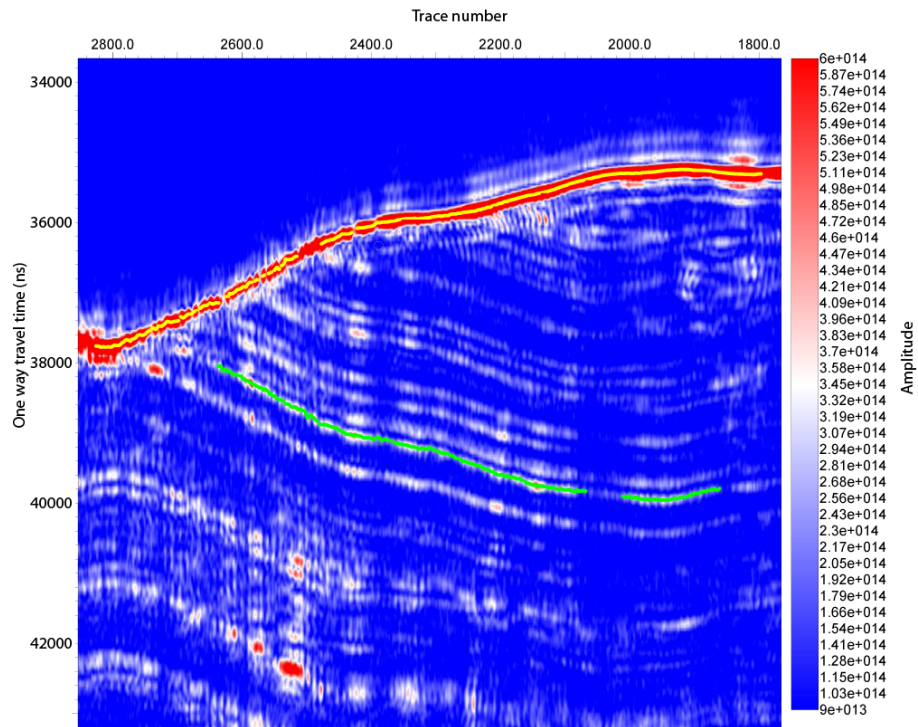
Track 7706 (In-line)



Track 7851 (In-line)



Track 8787 (In-line)



Track 10066 (In-line)

Appendix F: Matlab scripts for data analysis

1. *Combine_surface_subsurface_files.m*

```
clear all; clc; close all;

% Imported a #####_surface.dat and a #####_subsurface.dat files for one orbital track. These file
% were exported from horizon pickiing in Kingdom Suite. Each orbital track had one file for the
% surface horizon and one file for the subsurface horizon. Each .dat file contained columns of
% infomation, such as x and y coordinates in meter, orbital track #, trace #, and horizon pick in
% time and amplitude, for each trace along the horizon. This following script was to combine both
% files together based on their trace number. Each trace from one file looked for a trace from
% another file that had the same trace number and combined both trace into one trace. Therefore,
% each trace had both surface and subsurface information as an output.

% File names for all the orbital tracks
filename{1,01} = '4436_surface.dat'; filename{2,01} = '4436_subsurface.dat';
filename{1,02} = '4444_surface.dat'; filename{2,02} = '4444_subsurface.dat';
filename{1,03} = '5214_surface.dat'; filename{2,03} = '5214_subsurface.dat';
filename{1,04} = '5570_surface.dat'; filename{2,04} = '5570_subsurface.dat';
filename{1,05} = '5723_surface.dat'; filename{2,05} = '5723_subsurface.dat';
filename{1,06} = '5789_surface.dat'; filename{2,06} = '5789_subsurface.dat';
filename{1,07} = '7495_surface.dat'; filename{2,07} = '7495_subsurface.dat';
filename{1,08} = '7706_surface.dat'; filename{2,08} = '7706_subsurface.dat';
filename{1,09} = '7851_surface.dat'; filename{2,09} = '7851_subsurface.dat';
filename{1,10} = '8787_surface.dat'; filename{2,10} = '8787_subsurface.dat';
filename{1,11} = '10066_surface.dat'; filename{2,11} = '10066_subsurface.dat';
filename{1,12} = '11920_surface.dat'; filename{2,12} = '11920_subsurface.dat';

for idx = 1:length(filename(1,:))

    clear surface subsurface horizons remove k

    % imported a file for the surface horizon and a file for the subsurface horizon
    surface = importdata(filename{1,idx});
    subsurface = importdata(filename{2,idx});
    disp([filename{1,idx} ' and ' filename{2,idx} ' are being run right now!'])

    % Correct the time back to ns
    surface(:,5) = (surface(:,5)/0.00375).*37.5;
    subsurface(:,5) = (subsurface(:,5)/0.00375).*37.5;

    horizons = zeros(length(surface(:,1)),8);

    % This matrix had 8 columns as shown in the following for each orbital track:
    % Column 1 = x
    % Column 2 = y
    % Column 3 = track #
```

```

% Column 4 = trace #
% Column 5 = time(surface horizon)
% Column 6 = amp(surface horizon)
% Column 7 = time(subsurface horizon)
% Column 8 = amp(subsurface horizon)

% This contained all the information obtained from Kingdom Suite. This for loop was used to
% match all the traces between the surface and the subsurface horizons. Traces that did not have
% a matching trace were discarded.
for i = 1:length(surface(:,1))
    for k = 1:length(subsurface(:,1))
        if surface(i,4) == subsurface(k,4)
            horizons(i,1) = surface(i,1);
            horizons(i,2) = surface(i,2);
            horizons(i,3) = surface(i,3);
            horizons(i,4) = surface(i,4);
            horizons(i,5) = surface(i,5);
            horizons(i,6) = surface(i,6);
            horizons(i,7) = subsurface(k,5);
            horizons(i,8) = subsurface(k,6);
        end
    end
end

% k was a variable for counting how many row or trace that did NOT have a subsurface
% horizon pick. These rows or traces appeared to have 0 predefined if there was no input from
% Kingdom Suite.
k = 1;

% This for loop was to go through all the rows in horizons to look for any cells in the matrix
% that contained 0's, which mean there were no inputs from Kingdom Suite.
for i = 1:length(horizons(:,1))
    if horizons(i,8) == 0
        remove(k) = i;
        k = k + 1;
    end
end

% Variable_test was set to see whether the variable remove existed or not.
variable_test = exist('remove');

% If remove existed, this if statement deleted all those rows that had zeros.
if variable_test == 1
    for i = 1:length(remove)
        horizons(remove(i),:) = [];
        remove = remove - 1;
    end
end

% This wrote all the columns for an entire orbital track to a .csv file for later use.

```

```

if length(filename{1,idx}) == 16
    csvwrite([filename{1,idx}(1:4) '.csv'], horizons);
    movefile([filename{1,idx}(1:4) '.csv'],'\surface_subsurface_combined')
else
    csvwrite([filename{1,idx}(1:5) '.csv'], horizons);
    movefile([filename{1,idx}(1:5) '.csv'],'\surface_subsurface_combined')
end
end

```

2. *Analysis_along_each_cross_track_in_time.m*

```

clear all; clc; close all;

% Orbital tracks (cross-lines)
along_track = 11920; % 4444 5723 5789 11920
% Cross-lines' solar longitude for plotting purposes
ls_along_track = 207.23; % 272.67 331.61 334.42 207.23
% Orbital tracks (in-lines) that intersected all the cross-lines
track = [4436 5214 5570 7495 7706 7851 8787 10066];
% In-lines' solar longitude for plotting purposes
ls = [272.28 309.16 325.02 39.51 46.87 51.87 83.81 129.14];

% Set a datum that all the subsurface horizons were shifted to.
datum = 37500;

track_1 = num2str(along_track);
% Imported the cross-line
import_1 = importdata(['\surface_subsurface_combined\',track_1,'.csv']);

% For each in-line
for f = 1:length(track)

    clear distance_to_closest_trace input test test_limit

    track_2 = num2str(track(f));
    % Imported the in-line
    import_2 = importdata(['\surface_subsurface_combined\',track_2,'.csv']);

    % For each trace on the cross-line, it calculated the distance
    % between all the traces on the in-line and created a matrix to
    % store all the information shown below:

```

```

% Column 1 = minimum distance between one trace on the cross-line
% to the closest trace on the in-line.

% Information about the cross-line
% Column 2 = x coordinate from the cross-line
% Column 3 = y coordinate from the cross-line
% Column 4 = orbital track # from the cross-line
% Column 5 = trace # from the cross-line
% Column 6 = time(surface horizon) from the cross-line
% Column 7 = amp(surface horizon) from the cross-line
% Column 8 = time(subsurface horizon) from the cross-line
% Column 9 = amp(subsurface horizon) from the cross-line

% Information about the in-line
% Column 10 = x coordinate from the in-line
% Column 11 = y coordinate from the in-line
% Column 12 = orbital track # from the in-line
% Column 13 = trace # from the in-line
% Column 14 = time(surface horizon) from the in-line
% Column 15 = amp(surface horizon) from the in-line
% Column 16 = time(subsurface horizon) from the in-line
% Column 17 = amp(subsurface horizon) from the in-line

% Column 18 = Time difference of the surface horizons from both cross-line and in-line
% Column 19 = Calculate change of elevation using  $v = (c / (2 * \sqrt{e}))$ 

% Found the closest trace on the in-line in meter to each trace on the cross-line
for a = 1:length(import_1(:,1))
    for b = 1:length(import_2(:,1))
        % Calculated the distance using the x and y coordinates
        distance_to_closest_trace(b,1) = sqrt((import_1(a,1) - import_2(b,1))^2 + (import_1(a,2) -
import_2(b,2))^2);
        distance_to_closest_trace(b,2) = import_1(a,1);
        distance_to_closest_trace(b,3) = import_1(a,2);
        distance_to_closest_trace(b,4) = import_1(a,3);
        distance_to_closest_trace(b,5) = import_1(a,4);
        distance_to_closest_trace(b,6) = import_1(a,5);
        distance_to_closest_trace(b,7) = import_1(a,6);
        distance_to_closest_trace(b,8) = import_1(a,7);
        distance_to_closest_trace(b,9) = import_1(a,8);

        distance_to_closest_trace(b,10) = import_2(b,1);
        distance_to_closest_trace(b,11) = import_2(b,2);
        distance_to_closest_trace(b,12) = import_2(b,3);
        distance_to_closest_trace(b,13) = import_2(b,4);
        distance_to_closest_trace(b,14) = import_2(b,5);
        distance_to_closest_trace(b,15) = import_2(b,6);
        distance_to_closest_trace(b,16) = import_2(b,7);
        distance_to_closest_trace(b,17) = import_2(b,8);
    end
end

```



```

% This for loop went through all the traces on the
% cross-line, so that each trace on the cross-line was able to
% select a closest trace on the in-line. Both traces were stored on the same row.
for c = 1:length(distance_to_closest_trace(:,1))
    if distance_to_closest_trace(c,1) == min(distance_to_closest_trace(:,1))
        input(a,:) = distance_to_closest_trace(c,:);
    end
end
end
end

%-----%
%                travel time analysis                %
%-----%

% Traces were removed if the closest distance was too large between
% both traces from the cross-line and in-line.
test = input;
test_limit = 5.*median(abs(diff(input(:,1))));

for idx = 1:length(input(:,1))-1
    if abs(input(idx,1) - input(idx+1,1)) > test_limit
        test(idx,:) = nan;
    end
end

for idx = 1:length(input(:,1))-1
    if idx == 1
        if abs(input(length(input(:,1)),1) - input(length(input(:,1))-idx,1)) > test_limit
            test(idx,:) = nan;
        end
    else
        if abs(input(length(input(:,1))-idx+1,1) - input(length(input(:,1))-idx,1)) > test_limit
            test(idx,:) = nan;
        end
    end
end

test = test(isfinite(test));
test = reshape(test, length(test)/length(input(1,:)), length(input(1,:)));
input = test;

for g = 1:length(input(:,1))
    if min(input(:,1)) == input(g,1)
        plot_dh_ls(f,:) = input(g,:);
    end
end

% level both subsurface reflections to the datum
diff_time = plot_dh_ls(f,8) - datum;

```

```

diff_between_track_1_and_track_2 = plot_dh_ls(f,8) - plot_dh_ls(f,16);
plot_dh_ls(f,8) = plot_dh_ls(f,8) - diff_time;
plot_dh_ls(f,16) = plot_dh_ls(f,16) + diff_between_track_1_and_track_2 - diff_time;
% Shift both surface reflections as well by the amount the
% subsurface horizons were shifted
plot_dh_ls(f,6) = plot_dh_ls(f,6) - diff_time;
plot_dh_ls(f,14) = plot_dh_ls(f,14) + diff_between_track_1_and_track_2 - diff_time;

end

% Time difference between both surface reflections
plot_dh_ls(:,18) = (plot_dh_ls(:,6) - plot_dh_ls(:,14));
% Difference in meter
plot_dh_ls(:,19) = plot_dh_ls(:,18).*(0.3/(2*sqrt(2.12)));

% Plotting the change in thickness in meters against Ls
figure(1); clf;
hold on
plot(ls,plot_dh_ls(:,19),'*',ls_along_track,0,'ro'); set(gca,'FontSize',20)
hold off

for h = 1:length(plot_dh_ls(:,1))
    text(ls(h),plot_dh_ls(h,19),[' \leftarrow ' num2str(plot_dh_ls(h,12))], 'FontSize',20)
end

axis([0 360 0 70]);
xlabel('Solar Longitude (Ls)', 'fontsize',20); ylabel('Change of elevation between surface horizons
(m)', 'fontsize',20);
print('-f1', '-dpng', [track_1 ' _figure_1.png']);
movefile([track_1 ' _figure_1.png'], '\along_track_dh_variation')

% Plotting the change in elevation in time against Ls
figure(2);
hold on
plot(ls,plot_dh_ls(:,18),'*',ls_along_track,0,'ro'); set(gca,'FontSize',20)
hold off

for h = 1:length(plot_dh_ls(:,1))
    text(ls(h),plot_dh_ls(h,18),[' \leftarrow ' num2str(plot_dh_ls(h,12))], 'FontSize',20)
end

axis([0 360 0 700]);
xlabel('Solar Longitude (Ls)', 'fontsize',20); ylabel('Change of elevation between surface horizons
(ns)', 'fontsize',20);
print('-f2', '-dpng', [track_1 ' _figure_2.png']);
movefile([track_1 ' _figure_2.png'], '\along_track_dh_variation')

csvwrite(['plot_dh_ls_' track_1 '.csv'], plot_dh_ls);
movefile(['plot_dh_ls_' track_1 '.csv'], '\along_track_dh_variation')

```

3. *Amp_ratio.m*

```
clear all; clc; close all;

% Cross-lines
track = [4444 5723 5789 11920];
% Cross-lines' solar longitude for plotting purposes
ls_along_track = [272.67 331.61 334.42 207.23];
% Solar longitude of each in-line
ls = [272.28 309.16 325.02 39.51 46.87 51.87 83.81 129.14];

for id = 4%1:length(track)

    clf;

    num = num2str(track(id));
    import = importdata(['.\along_track_dh_variation\plot_dh_ls_', num, '.csv']);

    % Amp ratio = surface horizon's amplitude / subsurface horizon's amplitude
    % Calculated amp ratio of the cross-line at the intersection
    ratio(:,1) = import(:,7)./import(:,9);
    % Calculated amp ratio of the in-line at the intersection
    ratio(:,2) = import(:,15)./import(:,17);

    % Change in amplitude = In-line - Cross-line;
    ratio(:,3) = ratio(:,2) - ratio(:,1);

    % Plotting the amp ratios of the cross-line, the in-line, and the difference for each intersection
    figure(1)
    hold on;
    plot(ls,ratio(:,3),'>',ls_along_track(id),-4,'ro'); set(gca,'FontSize',20)
    hold off;

    for h = 1:length(import(:,1))
        text(ls(h),ratio(h,3),[' \leftarrow ' num2str(import(h,12))],'FontSize',20)
    end

    xlabel('Solar Longitude (Ls)'); ylabel('Difference in amplitude ratio');
    axis([0 360 -4 8])
    print('-f1', '-dpng', [num '_ratio.png']);
    movefile([num '_ratio.png'],'\amp_ratio');
end
```

4. *Dielectric_const_vs_velocity.m*

```
clear all; clc; close all;

% Dielectric constant
e = 1:0.1:80;
% Frequency
f = 20e6;
% Speed of light
c = 3e8;

velocity = (c./sqrt(e))./1e9;

figure(1)
plot(e,velocity)
xlabel('Dielectric constant'); ylabel('Radar wave propagation velocity (m/ns)');
```

5. *e_vs_change_in_thickness.m*

```
clear all; clc; fclose all;

% Dielectric constant
e = 1:0.01:5;
% Speed of light (m/ns)
c = 0.3e9;

% inline = [74, 77, 117]; % 4444
% inline = [97, 104, 61]; % 5723
% inline = [61, 76, 57]; % 5789
inline = [140, 77, 67]; % 11920

change_in_thickness = zeros(3, length(e));

figure(1)
hold on;

for k = 1:length(inline)
    for i = 1:length(e)
        change_in_thickness(k,i) = ((c*(inline(k)/1e9))/(2*sqrt(e(i))));
    end
end
```

```

end

plot(e,change_in_thickness(1,:), 'linewidth',2); set(gca,'FontSize',20)
plot(e,change_in_thickness(2,:), 'r', 'linewidth',2);
plot(e,change_in_thickness(3,:), 'g', 'linewidth',2);

text(2.12,change_in_thickness(1,113),[' \leftarrow '
num2str(change_in_thickness(1,113))], 'FontSize',16)
text(2.12,change_in_thickness(2,113),[' \leftarrow '
num2str(change_in_thickness(2,113))], 'FontSize',16)
text(2.12,change_in_thickness(3,113),[' \leftarrow '
num2str(change_in_thickness(3,113))], 'FontSize',16)

text(2.77,change_in_thickness(1,178),[' \leftarrow '
num2str(change_in_thickness(1,178))], 'FontSize',16)
text(2.77,change_in_thickness(2,178),[' \leftarrow '
num2str(change_in_thickness(2,178))], 'FontSize',16)
text(2.77,change_in_thickness(3,178),[' \leftarrow '
num2str(change_in_thickness(3,178))], 'FontSize',16)

xlabel('Dielectric constant','fontsize',20); ylabel('Change in thickness (m)','fontsize',20);
legend('In-lines 5570 and 10066', 'In-lines 4436 and 8787', 'In-lines 5214 and 7851',0,'fontsize',20)
hold off;

```